10-21-2016 12:00 AM

Low Frequency Bio-Electrical Impedance Mammography and Dielectric Measurement

Seyyed Hesabgar
The University of Western Ontario

Supervisor
Dr. Samani
The University of Western Ontario

Graduate Program in Medical Biophysics
A thesis submitted in partial fulfillment of the requirements for the degree in Doctor of Philosophy

Abstract

Assessment of electrical impedance of biological tissues at low frequencies offers a great potential for a safe, simple, and low-cost medical breast imaging techniques such as mammography. As such, in this dissertation a mammography method which uses tissue electrical impedance to detect breast malignancies was developed. The dissertation also introduces a new technique for measuring the dielectric properties of biological tissues at low frequencies. The impedance mammography technique introduced in this study is founded on the assumption that dielectric values of breast malignancies are significantly higher than the dielectric values of normal breast tissues. While previous studies have shown that this assumption is valid at high frequencies (50MHz-20GHz), less research efforts have been dedicated to ascertain the validity of such assumption at low frequencies (<1MHz). It is noteworthy that impedance imaging and characterization of biological tissues is highly advantageous at low rather than high frequencies. This is due to the higher contrast of capacitance and phase angle image data projections at low frequencies. Moreover, dispersion (energy loss) in biological tissues decreases significantly at low frequencies, rendering impedance imaging safer. The proposed tissue dielectric measurement technique in this study is based on tissue impedance measurement and using impedance data in an inverse finite element framework. This method was tested on several bovine tissue specimens and compared with convectional dielectric measurement techniques via simulation. Reliable electrical impedance data of malignant breast tumors are rare in the literature. To take a step toward providing such data, the proposed measurement technique was employed to measure the dielectric properties of normal and malignant breast tissue in xenograft mice model at 100Hz-1MHz. At the end, the possibility of using low frequency impedance mammography for detection of breast malignancies was investigated via *in silico* and tissue mimicking phantom studies. Results of this investigation suggest that imaging the electrical impedance properties of biological tissues through the proposed electrical impedance mammography can be potentially employed for breast cancer detection in a reliable and safe manner.

Keywords: Electrical Property, Electrical Impedance, Dielectric Properties, Biological Tissue, Breast Tissue, Breast Imaging, Mammography, Data Projection, Image Reconstruction, Breast Cancer, Tumor, Conductivity, Permittivity, Resistance, Capacitance, Phase Angle, Frequency, Resolution, Contrast, Sensor, Simulation, Phantom, Specimen, Voltage, Excitation Signal, Tumor Detection.

Co-Authorship Statement

This thesis is written by Seyyed M. Hesabgar under supervision of Dr. Abbas Samani. Part of the material presented in this thesis have been submitted for publication in peer-reviewed journal papers as listed below. The research presented in each submitted article has been conducted by the principal author and guided/supported by or in collaboration with the underlined authors who are the research supervisors or members of supervisory committee.

The material presented in Chapter 2: S. Hesabgar, R. Menon, A. Adler, A. Samani, "A Method for Tissue Characterization Based on Low Frequency Dielectric Measurement and Comparison with Conventional Techniques" has been submitted to Medical Engineering and Physics journal and is currently under review.

The material presented in Chapter 3: S. Hesabgar, A. Sadeghi-Naini, Gregory Czarnota, A. Samani, "Dielectric Properties of the Normal and Malignant Breast Tissues in Xenograft Mice at Low Frequencies (100Hz-1MHz)" has been submitted to Measurement journal and is currently under review.

The material presented in chapter 4: S. Hesabgar, A. Samani, "Toward Medical Electrical Impedance Mammography Using Low Frequency Excitation" is currently pending submission to the peer-reviewed journal papers due to the US Patent W-15-036 filed in August, 2015 by the authors.

Acknowledgements

I would like to seize this opportunity to thank the people without whom, this achievement would not be possible.

My first and foremost gratitude indeed belongs to God, as I believe God is the real source of knowledge in the universe and everything returns to him eventually. My Second gratitude belongs to my research supervisor, Dr. Abbas Samani, who guided me through PhD studies. I would like to thank my advisory committee, Dr. David Holdsworth and Dr. Ravi Menon for their valuable feedback and recommendations. I also would like to appreciate the University of Western Ontario for funding my research project. Finally, my deepest and sincerest gratitude belongs to my parents who helped and supported me throughout these years by their prayers and kindness.

Table of Contents

List of Tables

List of Figures

List of Appendices

List of Acronyms and Abbreviations

1D	One-dimensional or one dimension
2D	Two-dimensional or two dimensions
3D	Three-dimensional or three dimensions
A/D	Analog to Digital Converter
C	Capacitance
CT	Computed Tomography
EC	Electrical Conductivity
EP	Electrical Permittivity
FE	Finite Element
EM	Electromagnetic
ECT	Electrical Capacitance Tomography
EIT	Electrical Impedance Tomography
EIM	Electrical Impedance Mammography
EPT	Electrical Permittivity Tomography
FEM	Finite Element Method
MRI	Magnetic Image Resonance
R	Resistance
SCID	Severely Compromised Immune-deficient
STD	Standard Deviation
VNA	Vector Network Analyzer

Chapter 1

Introduction

1.1. Background and Motivation

Electrical impedance analysis of biological tissues offers the potential for a safe, simple, portable and low-cost technique for a broad range of bio-medical applications [1,2]. These applications include analysis of body composition (i.e. *in vivo* measurement of total body water (TBW) and total body fat (TBF) [1-3]), differentiation between different types of tissues (i.e. malignant from benign and healthy) [4-8], detection and quantification of lung water [9], bone health assessment [10], aortic blood pressure measurement [11], and medical imaging of different organs such as the lung [9] and breast [12]. While the bio-impedance assessment approach in some areas such as monitoring cardiac function or analysis of body composition is well-established [13], clinical applications of bio-impedance imaging requires further development. The motivation of this research is derived from the fact that bio-impedance imaging technology has a great potential to be used as non-ionizing, easy and low-cost tool for breast imaging. This is mainly because previous research in conjunction with one of our studies which is presented in the third chapter of this work, have shown that breast malignancies have significantly higher dielectric properties and substantially lower impedance values in comparison with normal breast tissues. In this work we have taken advantage of the dielectric behaviour of biological tissues in order to image the breast and detect its malignancies. In this respect, the second chapter of this work is concentrated on introducing a novel technique for measuring the dielectric properties of biological tissues and comparing it with conventional measurement techniques introduced in the past three decades [14]. In the third chapter, we introduce an improved version of the dielectric measurement technique described in Chapter 2. Chapter 3 also describes using this technique to measure electrical conductivity and permittivity of normal and cancerous breast tissues harvested from a xenograft mouse model. In the fourth and last chapter of this work, we introduce a novel

electrical impedance mammography technique in conjunction with three linear image reconstruction approaches. In this chapter we present *in silico* and tissue mimicking phantom studies to demonstrate that the technique in conjunction with the phase angle image reconstruction is capable of reliably imaging the breast and detecting its malignancies.

1.2. Dielectric Properties of Biological Tissues

1.2.1. Definition of Dielectric Properties

The bulk electrical properties of tissues and cell suspensions have been of interest for many reasons for over the past century. These properties are used to determine the pathways of current flow through the body [15]. In the context of bioelectrical impedance, dielectric property of a biological tissue usually refers to its electrical conductivity (σ) and electrical permittivity (ε). These two parameters are known as the main intrinsic electrical properties of the tissues. Electrical conductivity (σ, in S/m) of tissue is a measure of the tissue's ability to conduct, i.e. let charge pass through it. Electrical permittivity (ε, in F/m) of tissue provides a measure of polarizability of the tissue, i.e. its ability to store charge via electrical capacitance. Electrical permittivity is often expressed as the relative permittivity ε_r (or dielectric constant, dimensionless), which is defined as the permittivity relative to that of vacuum ($\varepsilon_0 = 8.854 \times 10$-12 F/m): $\varepsilon_r = \varepsilon_0\ \varepsilon_r$ [16].

1.2.2. Frequency Dependence of Tissue's Dielectric Properties

Electrical conductivity and permittivity of biological tissues are highly frequency dependent, meaning that the value of these parameters varies based on the excitation frequency. These variations are such that the electrical conductivity of biological tissues usually increases with frequency, whereas their electrical permittivity decreases sharply as frequency increases. In biological tissues, the variation range of electrical permittivity with frequency is an order of magnitude broader than that of electrical conductivity. Variations of the tissues dielectric properties with frequency can be used to infer valuable information about the body composition. These variations are also advantageous as they maybe utilized to find frequencies which are

optimal for imaging specific parts of the body. For instance, for assessing the body composition, low frequency impedance measurement provides information about the body's extracellular water percentage, while high frequency impedance measurement gives an estimate on the total body water and fat free body mass [1-3]. Figure 1.1 and 1.2 show, respectively, the behaviour of the electrical conductivity and relative permittivity of a typical soft tissue such as adipose and muscle at 10 Hz-20 GHz which are obtained experimentally by using VNA (Vector Network Analyzer) [1-3].

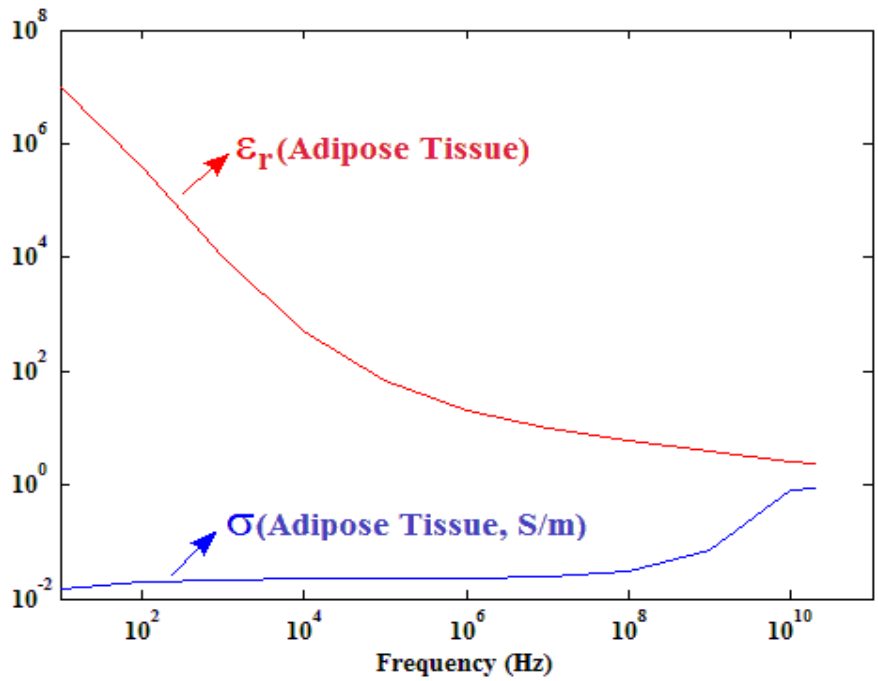

Figure 1.1. Variations of electrical conductivity (blue) and relative permittivity (red) of adipose tissue at 10Hz-20GHz [17, 18].

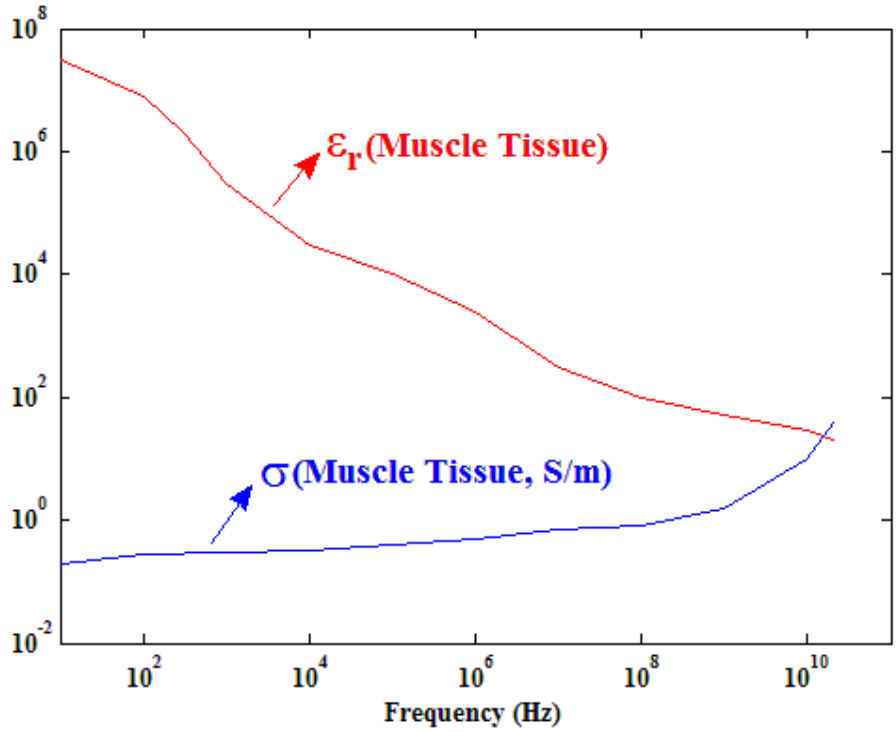

Figure 1. 2. Variations of electrical conductivity (blue) and relative permittivity (red) of muscle tissue at 10 Hz-20 GHz [16,17].

The relative permittivity of a biological tissue may reach up to 10^6 or 10^7 at frequencies below 100 Hz. It decreases at high frequencies in three main steps known as α, β, and γ dispersions [17]. For a biological tissue, α dispersion can be found around kilohertz region or lower, while β and γ dispersions are located in the hundred kilohertz and gigahertz frequency range, respectively [17, 19].

1.2.3. Dielectric Properties of Normal and Malignant Tissues

Dielectric properties of normal and malignant tissues have been of interest for many years. Only in the past three decades, hundreds of dielectric measurements have been conducted on various *ex* and *in vivo* biological tissues such as the breast, liver, bladder, skin and prostate [20-24]. Most of these measurements have shown that malignant tissues have significantly different dielectric values from their normal counterparts. For instance, researchers have found that dielectric properties of breast malignancies are substantially higher than those properties in benign and normal breast tissues [21,25-26]. Some of these findings have shown up to 20-40-fold higher

conductivity and permittivity values in malignant tissue compared to normal breast tissues [21]. Furthermore, researchers have shown that increase in the dielectric properties of cancer tissues is mainly caused by the higher concentration of intra and extracellular fluids, changes in the membrane and orientation of the malignant cells [27-29], and higher density of cells in malignant compared to normal tissues [16].

1.2.4. Dielectric Measurement Techniques and Tissue Characterization

1.2.4.1. VNA-based Approach

Dielectric properties of biological tissues have been measured by many researchers in the past one century [30-32]. While valuable in terms of laying the theoretical and empirical foundations of the field, many of these studies including most of the early works, involve theoretical over-simplification and measurement setups capable of providing only limited accuracy [17]. In the past three decades most of the measurements in this field, which have been conducted at high frequencies (20 MHz-20 GHz), are based on using network vector analyzer (VNA) and open-end coaxial cable. The VNA based approach has remained the method of choice for the dielectric characterization of biological materials at high frequencies [14]. This technique involves pressing the coaxial probe against the tissue while reflection coefficient or admittance of the probe–sample interface is measured and used to approximate the specimen's dielectric properties. Figure 1.3 shows the VNA-based biomedical device known as Margin Probe (Dune Medical, PA, USA). This device is used for tissue characterization during breast lumpectomy. MarginProbe measures the reflected electromagnetic waves at radio frequency in order to distinguish between malignant and healthy breast tissues during breast lumpectomy. The device has received FDA approval in 2012.

Figure 1.3. MarginProbe is used by a surgeon for breast tissue characterization during breast lumpectomy [52].

The accuracy that can be achieved in the VNA-based measurement approach is dependent on the reflected signal and reflection coefficient at the probe–sample interface [33]. While VNA based approach has been shown to be quite accurate and effective at high frequency, theoretical and empirical results from previous studies [14, 34-35] in conjunction with one of our studies which is presented in the second chapter of this work, have shown that VNA based technique is not capable of producing reliable dielectric measurements at low frequencies (<1MHz).

1.2.4.2. Inverse Finite Element Approach

In order to accurately measure the dielectric properties of biological tissues at low frequencies, an inverse finite element (FE) approach, which consists of an experimental and computational steps, is proposed in the Chapter 2 of this thesis. In the experimental step of this approach, the biological tissue is placed between two conductive plates or two conductive electrodes and its electrical impedance is measured. In the computational phase, the tissue and conductive plates/electrodes are modeled in a FE simulation software. Then the dielectric values of the

tissue's FE model are systematically altered using an optimization algorithm, until the impedance components of the FE computational model match with their experimental counterparts. The dielectric values that correspond to the best match of experimental and computational impedance are considered the tissue's dielectric values.

1.3. Relationship between Dielectric Properties, Resistance, and Capacitance

1.3.1. Relationship between Electrical Resistance and Conductance

Electrical conductivity (σ) is usually measured through measuring electrical resistance (R) as direct measurement of σ may not be feasible. R is a physical property that shows how well a material can resist the flow of electric current. It depends on the conductance and geometry of the materials which are placed inside the electric field while σ is an intrinsic property of the material and does not depend on the geometry or potential difference of the material placed inside the electric field. The following is a fundamental relationship used to express R [36]:

$$R = \frac{\mathrm{V}}{\mathrm{I}} = \frac{\int E.\ dl}{\oint \sigma E.\ ds} \qquad (1.1)$$

where V is the potential difference between the two electrodes, I is the electric current and E is the electric field. Equation 1.1 shows that the relationship between R and σ is complex; it depends highly on the conductor electrodes and geometry and conductivity of the material between them. Under the assumption of non-uniform E, the exact value of σ can be obtained from R by using numerical solutions such as finite element which is explained in section 1.7.2.

1.3.2. Relationship between Electrical Capacitance and Permittivity

Electrical permittivity (ε) is usually measured through measuring electrical capacitance (C), as direct measurement of electrical permittivity may not be feasible. C is a physical property of capacitors consisting of conductors and materials placed between them. It shows how well electric charge can be stored. Electrical capacitance depends on the geometry of the conductors and ε of the material placed between them while ε is an intrinsic property of the material and does not depend on the charge or potential difference between the conductors. The following is a fundamental relationship used to express C [36]:

$$C = \frac{\mathrm{Q}}{\mathrm{V}} = \frac{\oint \varepsilon E.\ ds}{\int E.\ dl} \qquad (1.2)$$

where Q is the electric charge, V the voltage between electrodes and E is the electric field. Equation 2 shows that the relationship between C and ε is highly complex as it depends on the geometry of the conductor electrodes and geometry and permittivity of the material between them. Under the assumption of non-uniform E, the exact value of ε can be obtained from C by using numerical solutions such as finite element which is explained in section 1.7.2.

1.4. Lumped Electrical Model of Biological Tissues

Figure 3 illustrates a lumped electrical model of a typical biological tissue. R_E and R_I in this model are influenced by the tissue's intra and extracellular fluids, respectively whereas C_M is dependent on the cell membranes of the tissue [1]. At low frequencies, where the electric current does not penetrate into the cell membranes, the cell walls act as barriers (insulators) against current flow. Consequently, at such frequencies R_I becomes very small, hence negligible [1]. At high frequencies, the cell membranes do not act as barriers against current flow and C_M becomes very small, hence negligible. As a result, the lumped electrical model of a biological tissue at high frequencies can be approximated by R_E paralleled with R_I [1].

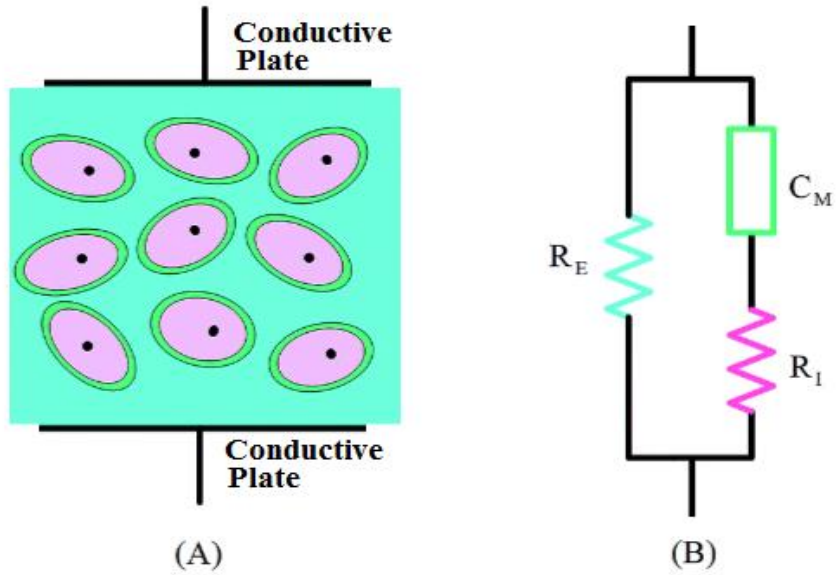

Figure 1.4. (A) A schematic of a typical biological Tissue. (B) Equivalent lumped circuit model.

1.5. Electrical Impedance of Biological Tissues

1.5.1. Definition of Bio-Electrical Impedance

Tissue's electrical or bio-electrical impedance is a physical parameter used to describe the combination of electrical resistance and electrical capacitance of a biological tissue [1]. Electrical impedance of a biological tissues is a function of frequency where it decreases as the frequency increases. At higher frequencies (>20kHz), the electrical impedance of a tissue can be approximated by only the tissue's resistance as its electrical reactance ($\frac{1}{C\omega}$) becomes significantly smaller than the tissue's resistance such that its impact on the overall tissue impedance becomes negligible.

1.5.2. Relationship between Electrical Impedance, Resistance, Capacitance and Phase Angle of Biological Tissues at Low Frequencies

The relationship between the electrical impedance, resistance, capacitance and phase angle of a biological tissue at low frequencies, which is derived from its equivalent circuit (Figure 4 (B)) in phasor format, is as follows:

$$Z_t \angle\theta_t = [(R_E/\omega C_M) / (R_E^2 + (1/\omega C_M)^2)^{1/2}] \angle -90^o + \text{Arctg}\,(1/R_E C_M \omega) \qquad (1.3)$$

where Z_t and θ_t are the amplitude and phase angle of the tissue's electrical impedance, ω is the natural frequency of the excitation signal, R_E and C_M are the tissue's electrical resistance and capacitance, respectively. It is noteworthy that R_I is considered to be very small and therefore negligible at low frequencies.

1.5.3. Phase Angle and its Bio-medical Implication and Application

The impedance phase angle of a biological tissue, which is usually obtained from the time delay between excitation and measured signals, is a function of the ratio of the tissue's permittivity to conductivity. As such, any changes in the ratio of the dielectric properties of a tissue at low frequencies manifests itself in the phase angle of the tissue. As described before, the permittivity of a tissue is influenced by its cell membranes [1]. In general, healthier and younger tissues exhibit higher permittivity and therefore higher phase angle values than older and unhealthy (non-cancerous) tissues of the same type [37]. Also, tissues with higher cell densities (e.g. cancerous tissues) have been shown to have higher electrical permittivity than tissues with lower cell densities [16]. As biological tissues start to die and their cell membranes begin to disintegrate, their permittivity and phase angle starts to decrease [13]. As a result, the impedance phase angle of biological tissues can be used as a measure of the overall tissue's health [39]. Furthermore, the phase angle has been found to be a prognostic indicator in several chronic conditions-such as HIV, liver cirrhosis, chronic obstructive pulmonary disease, and lung cancer-and in patients receiving dialysis [38]. In this study, we will show that phase angle-based image reconstruction can be used effectively to detect breast malignancies in electrical impedance mammography.

1.6. Literature Review Summary

1.6.1. Electrical Impedance Mammography (EIM)

Electrical impedance mammography (EIM) is a breast imaging modality that derives its contrast from electrical properties of the breast tissue. In EIM, the breast is compressed between two parallel plates or between one plate and the chest wall [41], and the electrical impedance projection of the breast tissue is measured before it is converted into 2D mammograms. Many of the studies conducted in the field of EIM in the past sixteen years are based on using the Siemens TransScan system (Siemens Medical, Germany, and TransScan, Ramsey, NJ, USA) and analyzing its performance. TransScan is an impedance mammography system which has received FDA approval for adjunctive use with X-ray Mammography [42]. This system consists of a hand-held electrode and measuring probe. Excitation signal with amplitudes of 1–2.5 volts and frequencies of 100 Hz-100 kHz is applied to the hand-held electrode. The measuring probe (Figure 1.6), which consists of a 2D array with multitude electrodes arranged on rectangular grid, is placed on the breast during the scan. The diagnosis in the TransScan mammography system is based on the spectral behaviour of the currents that pass through the breast tissue, namely the amplitude and phase components of the measured currents at various frequencies. These components are used to measure the resistance and capacitance of the breast tissue in order to generate impedance mammograms (Figure 1.7). Figure 1.5 shows a schematic of a typical breast examination performed by the TransScan 2000 system [41]. Based on analytical and simulation results, Assenheimer et al. [40] showed that the TransScan system is only capable of detecting highly conductive inclusions located close to the breast's surface. Among studies that assessed the performance of the TransScan 2000 for detecting breast carcinomas, Melloul et al. [44] used the system on 121 patients, all of whom had their breast lesions previously detected by other imaging modalities such as MRI and biopsied. Based on their results, Melloul et al. [44] obtained 72.2% sensitivity and 67% specificity for the TransScan 2000. Malich et al. [45] also used TransScan 2000 to examine 100 suspicious breast lesions and compared their results with MRI and US scans. They found that the TransScan 2000 system had 81% sensitivity and 63% specificity in detection and differentiation of the breast malignant and benign lesions. It is noteworthy that these values were higher than the sensitivity and specificity values of typical x-ray mammography systems as the sensitivity and specificity of such systems are around 40% and

24–58%, respectively [46]. Researchers also indicated that the greatest advantage of the TransScan TS2000 system was its ability to detect breast lesions as small as 3mm in diameter [44]. Despite these capabilities, previous studies [40] have shown that the TransScan mammography system still suffers from limited detectability depth.

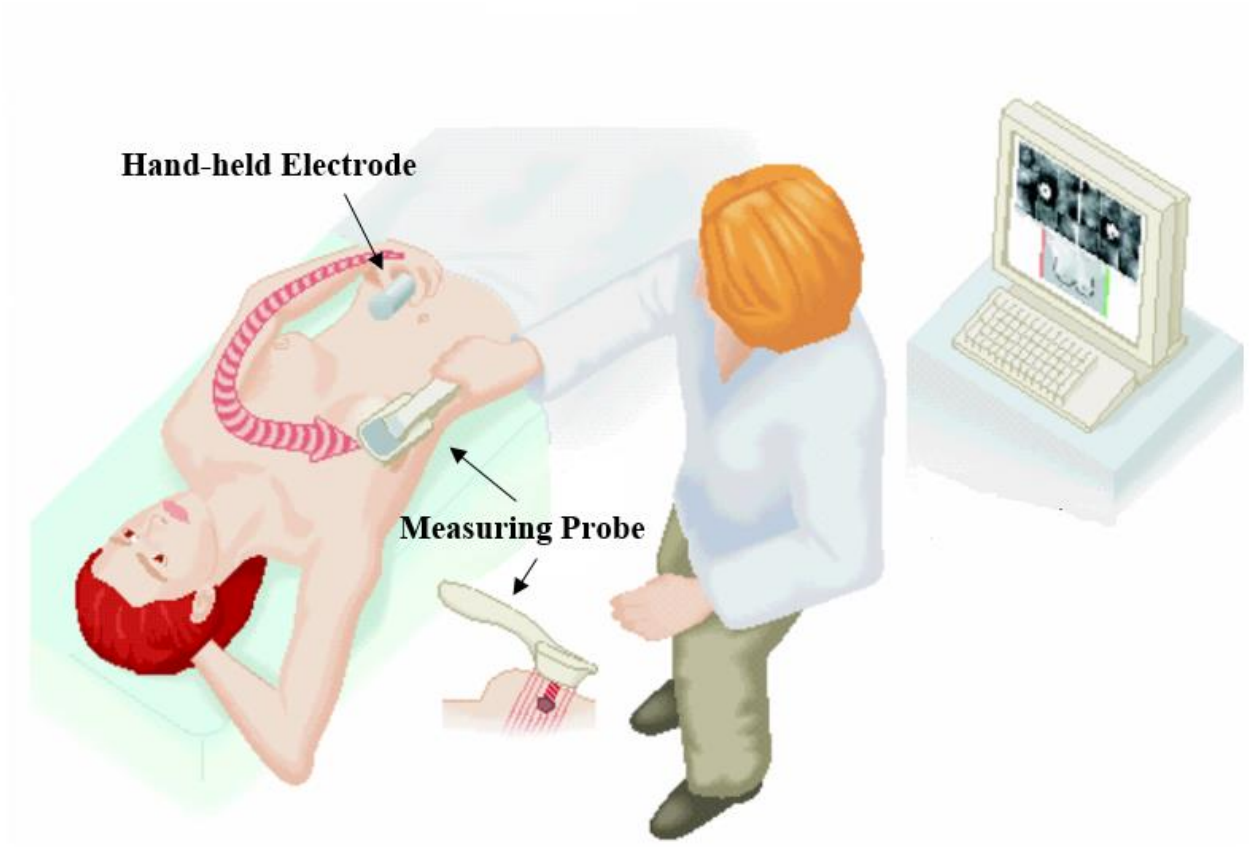

Figure 1.5. Schematic of the TransScan 2000 System [41]

Figure 1.6. Probe of the TransScan 2000 System [41]

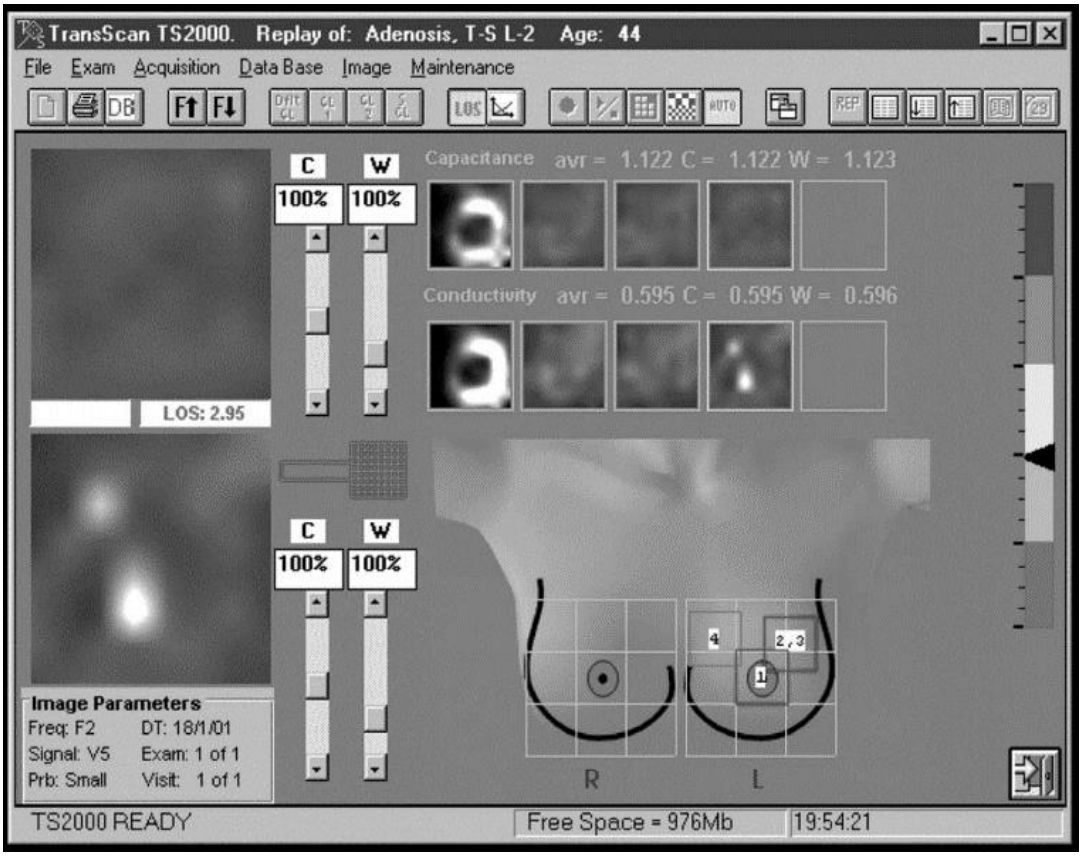

Figure 1.7. TransScan 2000 system examination window (LOS-Software) [47]. The bright spots in the above projection image represent the breast anomalies with higher dielectric values.

1.6.2. Electrical Impedance Tomography (EIT) of Breast

Many studies in the field of EIT are focused on breast imaging and detection of breast malignancies. This is mainly because previous studies have shown that breast malignancies have significantly higher conductivity and permittivity, and lower impedance values in comparison with normal breast tissues [21,25,26]. In breast EIT, usually a large number of electrodes are required to be attached to the breast surface to acquire the impedance data of the breast tissue between these electrodes before they are processed by a computer to generate tomographic 3D images of the impedance distribution within the breast. For impedance measurement, most practical EIT systems operate on a so called 'current-driving mode'. This mode involves applying a known, constant AC current to two or more electrodes, and measuring the voltages developed between other electrodes [48]. Conversely, the 'voltage driving mode' involves applying a known AC voltage to two or more electrodes and measuring the currents through other electrodes. Various data acquisition techniques have been used by different research groups in EIT. They mainly differ in the number and arrangement of electrodes, the excitation mode (i.e. current or voltage driving mode), the pattern of the excitation signal, and the working frequency range. Though being conceptually simple, the data acquisition process in EIT imaging is difficult to implement in practice. The image reconstruction in EIT is a challenging inverse problem, which is both nonlinear and ill posed. It usually involves solving the corresponding forward problem iteratively where a current estimation of impedance distribution is used to calculate the measured surface voltages from the applied currents. This iterative process continues until the calculated surface voltages match their measured counterparts [48]. The ill-posed and complex image reconstruction algorithms in conjunction with the large number of required electrodes are the two main limiting factors that have prevented EIT from becoming a viable clinical option in the area of breast imaging.

1.7. Theory

1.7.1. Maxwell's Equations

Data acquisition in EIT and EIM are based on measuring electrical quantities such as electric current and voltage on the body surface. These electrical quantities are governed by the constitutive physical laws. Maxwell's equations are the set of partial differential equations that

the constitutive physical laws use to define how these electrical quantities are generated and altered by each other and by electric and magnetic fields. For a nonmagnetic material such as biological tissues, the general form of Maxwell's equations in the time domain with the inclusion of displacement current and continuity equation is as follows [49]:

$$\nabla \cdot \mathbf{D}(r, t) = \rho(r, t) \qquad (1.4)$$

$$\nabla \times \mathbf{H}(r, t) = \mathbf{J}(r, t) + \frac{\partial \mathbf{D}(r,t)}{\partial t} = \sigma \mathbf{E}(r, t) + \mathbf{J_e}(r, t) + \frac{\partial \mathbf{D}(r,t)}{\partial t} \qquad (1.5)$$

$$\nabla \cdot \mathbf{B}(r, t) = 0 \qquad (1.6)$$

$$\nabla \times \mathbf{E}(r, t) = -\frac{\partial \mathbf{B}(r,t)}{\partial t} \qquad (1.7)$$

Where r is the location of each parameter in space, $\rho(r, t)$ is the electric charge density, $J(r, t) = \sigma E(r, t) + \mathbf{J_e}(r, t)$ is the electric current density, J_e is the externally induced current density (from the current source), $\sigma E(r, t)$ is known as conduction current density, E is the electric field, $D = \varepsilon E(r, t)$ is the electric displacement current, ε is the electric permittivity, $B(r, t)=\mu H(r, t)$ is the magnetic flux density, H(r, t) is the magnetic intensity and μ is the magnetic permeability which is considered to be the same as the permeability of vacuum for biological tissues. In this study we assume that the external magnetic flux density is negligible (i.e. $B(r, t) = 0$). We also assume that impedance measurement in EIT and EIM is performed at low frequencies (1MHz or lower) where voltage and current source frequencies are low enough for the electromagnetic field propagation delay to be neglected [50]. By using the phasor format of equations 1.4-1.7 and dropping the time harmonic, the format of Maxwell's equations in frequency domain are as follows:

$$\nabla \cdot \mathbf{D}(r, \omega) = \rho(r, \omega) \qquad (1.8)$$

$$\nabla \times \mathbf{H}(r, \omega) = \mathbf{J}(r, \omega) + j\omega\, \mathbf{D}(r, \omega) = \sigma \mathbf{E}(r, \omega) + \mathbf{J_e}(r, \omega) + j\omega\, \mathbf{D}(r, \omega) \qquad (1.9)$$

$$\nabla \cdot \mathbf{B}(r, \omega) = 0 \qquad (1.10)$$

$$\nabla \times \mathbf{E}(r, \omega) = -j\omega\, \mathbf{B}(r, \omega) \qquad (1.11)$$

Where ω is the natural frequency and Je is externally induced current density. In EIT and EIM, Maxwell's equations are usually solved based on an inverse problem framework where the finite element method (FEM) is used as the corresponding forward model.

1.7.2. Finite Element Method

The description of constitutive laws of physics for Maxwell's equations are expressed in terms of the partial differential equations (PDEs) described earlier. For the vast majority of problems and geometries, these PDEs cannot be solved with analytical methods. Instead, an approximation of the equations can be constructed, typically based upon different types of discretizations. These discretization methods approximate the PDEs with numerical model equations, which can be solved using numerical methods. The finite element method (FEM) is used to compute such approximations [51]. In other words, FEM discretizes complex geometries (i.e. breast in this study) into smaller elements with finite shape and simple geometries such as tetra- or hexahedral elements for a 3D object. The process of discretization in FEM is known as mesh generation. In this process, the original object is approximated with an assembly of elements which are connected at a finite number of joints, known as nodes. The properties of these elements (i.e. conductivity, permittivity, etc.) in conjunction with their geometry are entered to form the so called stiffness equation for each element. The element stiffness equation is a small set of algebraic equations derived based on the approximate version of the PDE which is strictly valid within the respective element. There are several methods (e.g. Galerkin method) to turn the PDEs into approximate algebraic equations valid for each element. The element equations are obtained in matrix form. The next step is to assemble the element equations into a large system of equations that governs the whole body. Next, the boundary conditions are applied and the system of equation is solved, leading to the required variables such as voltage, current, and phase angle for each element. In FEM, the convergence of the algorithm to an accurate solution is highly dependant upon the quality of the generated mesh, including the size, type and shape of elements.

1.8. Thesis Objective

The main objective of this work is to investigate the possibility of using the electrical impedance of biological tissues for the detection of breast malignancies and generating mammograms at low frequencies. As described earlier, for the bio-impedance based detection of breast malignancies at any frequency, the dielectric properties of the breast cancer tissues need to be significantly higher than the dielectric properties of their surrounding breast tissue. While previous studies have somewhat shown that dielectric values of the breast malignancies at high frequencies (20 MHz-20 GHz) are significantly different from the dielectric values of normal breast tissue, sufficient and reliable data pertaining to the dielectric values of normal and malignant breast tissues at low frequencies are not available in the literature. The majority of researchers in the past three decades utilized conventional VNA-based measurement techniques for measuring tissue dielectric properties. Theoretical and empirical studies have shown that VNA-based techniques are not capable of accurately measuring the dielectric properties of biological tissue at low frequencies. For this reason, another objective of this investigation is to introduce a reliable approach for measuring the dielectric properties of biological tissues at low frequencies. The other objective of this study is to ensure that the dielectric properties of breast malignancies at low frequencies are significantly different from the dielectric properties of normal breast tissues. To achieve these objectives, a finite element (FE) based computational approach in conjunction with using an impedance sensor for measuring tissues dielectric properties at low frequencies is proposed in this study. Based on theoretical evidence and simulation studies, we have shown that the proposed FE-based technique, which takes into account the real geometry and inhomogeneity of the biological tissues, is superior to the conventional VNA-based approach. For this purpose, we used an improved version of the proposed FE-based approach and measured the dielectric properties of the normal and malignant breast tissues in xenograft mice model at low frequencies (100 Hz-1 MHz). The results of this investigation, which is presented in third chapter of this work, indicated that the dielectric properties of breast cancer tissue at low frequencies are significantly higher than their corresponding properties of normal breast tissues. Furthermore, comparison between the measured conductivity and permittivity in this investigation showed that the permittivity of breast tissues at low frequencies can be used as a more powerful bio-marker than the conductivity for differentiation of healthy and malignant breast tissues. To achieve the main objective of this investigation, we conducted an *in silico* and tissue mimicking phantom

studies which involved using a parallel plate impedance sensor and a breast model with an inclusion with higher electrical conductivity and permittivity values. In this investigation, we compared different types of data projection images which were obtained from the mentioned *in silico* and tissue mimicking phantom studies and showed that the proposed impedance sensor with phase angle projection image can reliably detect breast malignancies with higher dielectric values than their surrounding normal breast tissues.

1.9. Thesis Outline

The thesis objectives which are defined above have been presented in three separate chapters followed by a closing chapter where the thesis conclusion and future directions are discussed. The material presented in each chapter is outlined below.

1.9.1. Chapter 2 (Paper 1)

In chapter 2 of this dissertation, a novel technique for measuring the dielectric properties of biological tissues such as tissue electrical permittivity at low frequencies is presented. The proposed technique utilizes a high precision hardware for impedance measurement of a sensor formed by two conductive parallel plates with the tissue specimen as its dielectric. The capacitance part of measured impedance is processed using an inverse finite element framework to determine the tissue's electrical permittivity. This framework considers the specimen's accurate geometry and boundary conditions. After successful validation, to demonstrate its performance, the technique was employed to measure the electrical permittivity of several specimens of bovine heart, liver and bone tissues. Furthermore, the sensitivity and accuracy of the proposed technique and the conventional VNA-based approach for measuring the permittivity of tissue specimen with inhomogeneity was analyzed and compared via *in silico* studies in this chapter.

1.9.2. Chapter 3 (Paper 2)

The possibility of using dielectric properties for tissue characterization in breast cancer has been studied in this chapter. For this purpose, several normal and malignant breast tissue specimens harvested from a xenograft mice model were measured at 100 Hz-1 MHz before they were compared. The measurements are conducted by using an improved version of the permittivity measurement technique presented in chapter 2 of this thesis.

1.9.3. Chapter 4 (Paper 3)

In this chapter, the feasibility of using the electrical impedance properties of breast tissues for detection of breast malignancies and generation of impedance mammograms are investigated. For this purpose, a breast electrical impedance mammography system consisting of a parallel plate impedance sensor was developed in conjunction with different types of image reconstructions. The effectiveness of the proposed system along with the image reconstruction methods was assessed through *in silico* and tissue mimicking phantom studies.

1.9.4. Chapter 5 (Conclusions and Future Work)

This chapter summarizes the materials presented in Chapters 2 through 4. It also suggests possible future directions for the research described in this thesis and finally concludes this dissertation.

References

[1] Ursula G. Kyle, Ingvar Bosaeus, Antonio D. De Lorenzo, Paul Deurenberg, Marinos Elia, Jose Manuel Gomez, Berit Lilienthal Heitmann, Luisa Kent-Smith, Jean-Claude Melchior, Matthias Pirlich, Hermann Scharfetter, Annemie M.W.J. Schols, Claude Pichard, Bioelectrical impedance analysis part I: review of principles and methods, Clinical Nutrition (2004) 23, 1226–1243

[2] Ursula G. Kyle, Ingvar Bosaeus, Antonio D. De Lorenzo, Paul Deurenberg, Marinos Elia, Jose Manuel Gomez, Berit Lilienthal Heitmann, Luisa Kent-Smith, Jean-Claude Melchior,

Matthias Pirlich, Hermann Scharfetter, Annemie M.W.J. Schols, Claude Pichard, Bioelectrical impedance analysis—part II: utilization in clinical practice, Clinical Nutrition (2004) 23, 1430–1453

[3] B. J. Thomas, L. C. Ward, B. H. Cornish; Bioimpedance Spectrometry in the Determination of Body Water Compartments: Accuracy and Clinical Significance, Appl. Radiat. lsot. Vol. 49, No. 5/6, pp. 447455, 1998

[4] Ryan J. Halter, Alan Schned, John Heaney, Alex Hartov, Keith D. Paulsen; Electrical Impedance Spectroscopy of Benign and Malignant Prostatic Tissues, DOI 10.1016/j.juro.2007.11.043

[5] Ryan J. Halter, Alex Hartov, Keith D. Paulsen, A Broadband High-Frequency Electrical Impedance Tomography System for Breast Imaging, IEEE Transactions on Biomedical Engineering, Vol. 55, No. 2, Feb 2008.

[6] Ryan J. Halter, Alan R. Schned, John A. Heaney, Alex Hartov; Passive Bioelectrical Properties for Assessing High- and Low-Grade Prostate Adenocarcinoma, The Prostate 71:1759-1767 (2011)

[7] William T. Joines, Yang Zhang, Chenxing Li, Randy L. Jirtle; The measured electrical properties of normal and malignant human tissues from 50 to 900 MHz, Med. Phys. 21, 547 (1994)

[8] William T. Joines, Randy L. Jirtle, Marc D. Rafal, Daniel J. Schaefer; Microwave power absorption differences between normal and malignant tissue, International Journal of Radiation Oncology Biology Physics, Volume 6, Issue 6, June 1980, Pages 681–687

[9] Neale R. Lange, Daniel P. Schuster; The measurement of lung water, *Crit Care* 1999, **3**:R19–R24

[10] Paul M. Meaney, Tian Zhou, Douglas Goodwin, Amir Golnabi, Elia A. Attardo, Keith D. Paulsen, Bone Dielectric Property Variation as a Function of Mineralization at Microwave Frequencies, International Journal of Biomedical Imaging, Volume 2012, Article ID 649612, 9 pages, doi:10.1155/2012/649612

[11] Fabian Braun, Martin Proença, Michael Rapin, Mathieu Lemay, Andy Adler, Bartłomiej Grychto, Josep Solà, Jean-Philippe Thiran; Aortic blood pressure measured via EIT: investigation of different measurement settings, Physiol. Meas. 36 (2015) 1147–1159

[12] Ryan J. Halter, Member, IEEE, Alex Hartov and Keith D. Paulsen, A Broadband High-Frequency Electrical Impedance Tomography System for Breast Imaging, 650 IEEE Transactions on Biomedical Engineering, Vol. 55, No. 2, Feb 2008

[13] Frederick D. Coffman and Stanley Cohen, Modern Trends in Imaging XI: Impedance measurements in the biomedical sciences, Analytical Cellular Pathology 35 (2012) 363–374 DOI 10.3233/ACP-2012-0070 IOS Press

[14] C. Gabriel, A. Peyman, Dielectric measurement: error analysis and assessment of uncertainty, Phys. Med. Biol. 51 (2006) 6033–6046

[15] Foster, K. R. "Dielectric Properties of Tissues."The Biomedical Engineering Handbook: Second Edition, Ed. Joseph D. Bronzin , Boca Raton: CRC Press LLC, 2000

[16] Gerard H. Markxa, Christopher L. Daveyb, The dielectric properties of biological cells at radiofrequencies: Applications in biotechnology, Enzyme and Microbial Technology 25 (1999) 161–171

[17] The dielectric properties of biological tissues: I. Literature survey, C Gabriel, S Gabriely and E Corthout, Phys. Med. Biol. 41 (1996) 2231–2249. Printed in the UK

[18] S Gabriel, R W Lau and C Gabriel, The dielectric properties of biological tissues: II. Measurements in the frequency range 10 Hz to 20 GHz, Phys. Med. Biol. 41 (1996) 2251–2269. Printed in the UK

[19] Sverre Grimnes, Ørjan G Martinsen, Alpha-dispersion in human tissue; Journal of Physics: Conference Series 224 (2010) 012073 doi:10.1088/1742-6596/224/1/012073

[20] William T. Joines, Yang Zhang, Chenxing Li, Randy L. Jirtle; The measured electrical properties of normal and malignant human tissues from 50 to 900 MHz, Med. Phys. 21, 547 (1994)

[21] Andrzej J. Surowiec, Stanislaw S. Stuchly, J. Robin Barr, Arvind Swarup, Dielectric Properties of Breast Carcinoma and the Surrounding Tissues, IEEE Transactions on Biomedical Engineering, Vol. 35, No. 4, April 1988

[22] Ryan J. Halter, Alan Schned, John Heaney, Alex Hartov, Keith D. Paulsen; Electrical Impedance Spectroscopy of Benign and Malignant Prostatic Tissues, DOI 10.1016/j.juro.2007.11.043

[23] Ann P O'Rourke, Mariya Lazebnik, John M Bertram, Mark C Converse, Susan C Hagness, John G Webster and David M Mahvi, Dielectric properties of human normal, malignant and

cirrhotic liver tissue: in vivo and ex vivo measurements from 0.5 to 20 GHz using a precision open-ended coaxial probe, Phys. Med. Biol. 52 (2007) 4707–4719

[24] Reza Aminzadeh, Mehrdad Saviz, Amir Ahmad Shishegar, Dielectric Properties Estimation of Normal and Malignant Skin Tissues at Millimeter-Wave Frequencies Using Effective Medium Theory, The 22nd Iranian Conference on Electrical Engineering (ICEE 2014), May 20-22, 2014, Shahid Beheshti University

[25] H. Fricke and S. Morse, "The electric capacity of tumors of the breast," J. Cancer Res., vol. 16, pp. 310-376, 1926

[26] Hardik J. Pandya1, Hyun Tae Kim, Rajarshi Roy, Wenjin Chen, Lei Cong, Hua Zhong, David J. Foran, and Jaydev P. Desai, Towards an Automated MEMS-based Characterization of Benign and Cancerous Breast Tissue using Bioimpedance Measurements, Sens Actuators B Chem. 2014 August 1; 199: 259–268. doi:10.1016/j.snb.2014.03.065

[27] William T. Joines, Randy L. Jirtle, Marc D. Rafal, Daniel J. Schaefer; Microwave power absorption differences between normal and malignant tissue, International Journal of Radiation Oncology Biology Physics, Volume 6, Issue 6, June 1980, Pages 681–687

[28] B. Rigaud, J.P. Morucci, N. Chauveau, Bioelectrical impedance techniques in medicine. Part I: Bioimpedance measurement. Second section: impedance spectrometry, Clin. Rev. Biomed. Eng. 24 (1996) 257

[29] J. Cuzick, R. Holland, V. Barth, R. Davies, M. Faupel, I. Fentiman, H.J. Frischbier, J.L. LaMarque, M. Merson, V. Sacchini, D. Vanel, U. Veronesi, Electropotential measurements as a new diagnostic modality for breast cancer, Lancet 352(9125) (1998) 359-363

[30] T. S. England and N. A. Sharples, "Dielectric properties of the human body in the microwave region of the spectrum," Nature, vol. 163, pp. 487-488, 1949

[31] T. S. England, "Dielectric properties of the human body for wave lengths in the 1-10 cm range," Nature, vol. 166, pp. 480-481, 1950

[32] Ann P O'Rourke, Mariya Lazebnik, John M Bertram, Mark C Converse, Susan C Hagness, John G Webster, David M Mahvi; Dielectric properties of human normal, malignant and cirrhotic liver tissue: in vivo and ex vivo measurements from 0.5 to 20 GHz using a precision open-ended coaxial probe; Phys. Med. Biol. 52 (2007) 4707–4719 doi:10.1088/0031-9155/52/15/022

[33] David M. Pozar; Microwave Engineering, Fourth edition, Wiley Global Education, 2011, P28-29

[34] James Baker Jarvis, Michael D. Janezic, Paul D. Domich, Richard G. Geyer; Analysis of an Open-Ended Coaxial Probe with Lift-off for Nondestructive Testing, IEEE Transactions on Instrumentation and Measurement, Vol. 43, No. 5, October 1994

[35] James Baker Jarvis, Michael D. Janezic, Bill F. Riddle, Robert T. Johnk, Pavel Kabos, Christopher L. Holloway, Richard G. Geyer, Chriss A. Grosvenor; Measuring the Permittivity and Permeability of Lossy Materials: Solids, Liquids, Metals, Building Materials, and Negative-Index Materials; Electromagnetics Division, National Institute of standards and Technology, U.S. Department of Commerce, 2004

[36] David K. Cheng, Field and Wave Electromagnetics, 1989

[37] Maria Cristina G Barbosa-Silva, Aluísio JD Barros, Jack Wang, Steven B Heymsfield, and Richard N Pierson J; Bioelectrical impedance analysis: population reference values for phase angle by age and sex; Am J Clin Nutr 2005;82:49 –52

[38] Gupta D, Lammersfeld CA, Burrows JL, Dahlk SL, Vashi PG, Grutsch JF, Hoffman S, Lis CG, Bioelectrical impedance phase angle in clinical practice: implications for prognosis in advanced colorectal cancer. Am J Clin Nutr. 2004 Dec;80(6):1634-8

[39] Barbosa-Silva, Maria Cristina G, Barros, Aluísio JD, Bioelectrical impedance analysis in clinical practice: a new perspective on its use beyond body composition equations, Current Opinion in Clinical Nutrition & Metabolic Care: Pharmaceutical aspects, devices and techniques; May 2005 - Volume 8 - Issue 3 - p 311–317

[40] Michel Assenheimer, Orah Laver-Moskovitz, Dov Malonek, David Manor, Udi Nahaliel, Ron Nitzan1 and Abraham Saad, The T-SCANTM technology: electrical impedance as a diagnostic tool for breast cancer detection, Physiol. Meas. 22 (2001) 1–8

[41] Mirabel Medical Systems, Inc., T-Scan 2000 ED, PMA P050003 Panel Pack, Table of Contents

[42] B. Scholz, R. Anderson, On Electrical Impedance Scanning Principles and Simulations, Siemens AG, Medical Engineering Group, Erlangen, Germany, Siemens-Elema AB, Solna, Sweden

[43] Tyna Hope and Siân E, The use of electrical impedance scanning in the detection of breast cancer, Breast Cancer Res. 2004; 6(2): 69–74

[44] Melloul M, Paz A, Ohana G, Laver O, Michalevich D, Koren R, Wolloch Y, Gal R: Double phase Tc-sectamibi scintimammography and Trans-Scan in diagnosing breast cancer. J Nucl Med 1999, 40:376-380

[45] Malich A, Boehm T, Facius M, FreesMeyer MG, Fleck M, Anderson R, Kaiser WA: Differentiation of mammographically suspicious lesions: evaluation of breast ultrasound, MRI mammography and electrical impedance scanning as adjunctive technologies in breast cancer detection. Clin Radiol 2001, 56:278-283

[46] MO Leach, CRM Boggis, AK Dixon, DF Easton, RA Eeles, DGR Evans, FJ Gilbert, I Griebsch, RJC Hoff, P Kessar, SR Lakhani, SM Moss, A Nerurkar, AR Padhani, LJ Pointon, D Thompson, RML Warren; Screening with magnetic resonance imaging and mammography of a UK population at high familial risk of breast cancer: a prospective multicentre cohort study; Lancet 2005; 365: 1769–78

[47] Thomas Diebold, Volkmar Jacobi, Bernhard Scholz, Conny Hensel, Christine Solbach, Manfred Kaufmann, Fernando Viana, Joern Balzer, Jutta Peters, Thomas Vogl, Value of Electrical Impedance Scanning (EIS) in the Evaluation of BI-RADS™ III/IV/V-Lesions, Technology in Cancer Research & Treatment ISSN 1533-0346 Volume 4, Number 1, February (2005)

[48] Y. Zou, Z. Guo, A review of electrical impedance techniques for breast cancer detection, Medical Engineering & Physics 25 (2003) 79–90

[49] Roberto Cardu, Philip H W Leong, Craig T Jin, Alistair McEwan, Electrode contact impedance sensitivity to variations in geometry, Physiol. Meas. 33 (2012) 817–830 doi:10.1088/0967-3334/33/5/817

[50] Wang W and Eisenberg S R 1994 A three-dimensional finite element method for computing magnetically induced currents in tissues *IEEE Trans. Magn.* 30 5015–23

[51] www.comsol.com/multiphysics/finite-element-method, Nov. 3, 2016

[52] http://marginprobe.com, Nov. 3, 2016

Chapter 2

A Method for Tissue Characterization Based on Low Frequency Dielectric Measurement and Comparison with Conventional Techniques

The material presented in this chapter has been submitted to Medical Engineering and Physics journal.

Authors' Contributions Statement: *The main idea of this chapter is conceived by the principal author, Seyyed M. Hesabgar and the research supervisor, Dr. Abbas Samani. The research, experiments, and tissue specimen preparation presented in this chapter have been conducted by the principal author Seyyed M. Hesabgar and guided by the research supervisor Dr. Abbas Samani. The general guidelines regarding the application of simulation software in this chapter are provided by Dr. Ravi Menon (member of supervisory committee). The Feedbacks, comments and revisions regarding the martial which is presented in this chapter (especially the material of the introduction section) are provided by the collaborator of this study, Dr. Andy Adler.*

2.1. Introduction

Accurate measurement of dielectric properties of biological tissues is important for a broad range of applications including development of medical imaging techniques that map tissue electrical properties (e.g. Electrical Capacitance Tomography (ECT) and Electrical Permittivity Tomography (EPT)) [1-4], tissue characterization and classification (e.g. differentiation between normal and malignant tissues) [2-4,17], studying biological tissue interaction with electromagnetic fields [20-27], and bone health assessment [5]. For such applications, having a reliable database from electrical permittivity (EP) of biological tissues is essential. As an example of tissue characterization application based on measuring the tissue dielectric properties, an intra-operative device named MarginProbe (MarginProbe, PA, USA), was developed and received FDA approval in 2012. MarginProbe is used during breast lumpectomy to distinguish malignant from healthy tissues based on the difference in their measured dielectric values [6].

Among other applications, EP imaging has a good potential as a diagnostic tool. EP properties of biological tissues cover a broad range which implies that EP imaging can produce high contrast images with enhanced diagnostic data [7,8]. EP can potentially be used as a biomarker to differentiate between various pathologies and to detect and classify tissue abnormalities such as tumors [2-4,17]. Table 2.1 presents relative electrical permittivity and electrical conductivity values of six types of human tissues at 100Hz, 100 kHz, 100 MHz and 10 GHz [7,8]. This table shows that relative permittivity (ε_r) of biological tissues decreases significantly while their conductivity (σ, S/m) increases with higher frequencies. This implies that EP imaging at low frequencies is highly advantageous as it can provide images with broad dynamic range and high contrast. For example, the table shows a ratio of 1774 as highest to lowest for ε_r at 100 Hz while this ratio is only 7.5 at 10 GHz. Furthermore, energy loss in biological tissues at low frequencies is significantly lower than at high frequencies due to the lower conductance, rendering tissue electrical property imaging safer. While significant efforts have been dedicated to study tissue EP at high frequencies, less efforts have been made to study EP at frequencies below 1MHz, where the literature values are scarce and have substantial uncertainties [10].

Table 2.1. Relative electrical permittivity and conductivity of various human tissues measured at four different frequency range [7, 8].

Tissue name	Muscle	Bone (Cortical)	Blood	Brain (White matter)	Brain (Grey matter)	Fat
ε_r, σ(S/m) @100 Hz	9329000 ,0.3	5852.8, 0.02	5259.8,0.7	1667700,0.05	3906100,0.06	457060,0.03
ε_r, σ(S/m) @100 kHz	8089, 0.5	227.6,0.02	5120,07	2108,0.8	3221,0.1	92.89,0.04
ε_r, σ(S/m) @100 MHz	65.9, 0.9	15.3,0.1	76.8,1.2	56.8,0.35	80.14,0.6	6.07,0.08
ε_r, σ(S/m) @10 GHz	30, 28	7, 2	45, 12	30, 10	35, 10	4, 0.6

Among researchers who measured electrical permittivity of biological tissues, Peyman et al. [9,12] measured EP of porcine and rat tissues at different ages from 40MHz to 20 GHz. Their results showed a general trend of EP reduction with age. For bone health assessment, Meaney et al. [5] conducted *ex vivo* microwave dielectric measurements on porcine trabecular bone specimens with various densities. Their results showed a strong correlation between both EP value and bone volume density. Among researchers who measured the EP of pathological tissues, Joines et al. [16,17] measured EP of various normal and malignant tissues acquired from rats and humans at 30 MHz-2 GHz, where they showed that at all frequencies the EP of

malignant tissues are up to 233% greater than their normal tissue counterparts. For breast and prostate benign and malignant tumor assessment, Halter et al. [2-4] developed measurement setups and imaging systems where they showed that tissue EP can be used not only to differentiate between malignant and benign tumors but also for cancer grade assessment.

To our knowledge, methods developed over the past three decades for measuring biological tissues EP, have used conventional measurement techniques by utilizing open-end coaxial cable in conjunction with analytical model based on a lumped parameter approach. More recently, such measurement systems utilized vector network analyzer (VNA) in conjunction with the open-end coaxial cable. These techniques involve pressing the coaxial probe against the specimen while the reflection coefficient or admittance of the probe–sample interface is measured and used to approximate the specimen's EP. Accuracy achieved in this measurement approach is dependent on the reflected signal and reflection coefficient at the probe–sample interface [36]. At low frequencies (<100kHz), where impedance of biological tissues is significantly higher than that of coaxial probe, measurement errors lead to very high amplification of the tissue EP estimation errors. Another issue associated with these techniques pertains to the lumped parameter approach used for its data processing.

As shown in this article through an in-silico phantom study, this may lead to large errors when the tissue sample has even small amount of inhomogeneity, confirming the importance of accounting for tissue actual geometry and boundary conditions. The latter can be effectively achieved through a distributed parameter modeling approach formulated using a finite element (FE) framework. Among researchers who pointed out limitations of current conventional EP measurement techniques, Gabriel and Peyman [11] and Baker et al. [18,19] demonstrated that the error percentage of using the conventional approach at low frequencies can exceed 50%. As such, a robust technique for EP measurement of biological tissues, which takes into account specimen's geometry and boundary conditions reliably while having low sensitivity to its inhomogeneity and raw data measurement errors, is desirable.

In this study, we introduce a novel technique with improved EP measurement accuracy for biological tissue specimens acquired from surgical procedures. In contrast to the conventional method which relies on signal reflection, the proposed method does not suffer from EP estimation error at low frequencies. It uses the distributed parameter FE approach which models

the specimen's geometry and boundary conditions accurately, leading to low sensitivity to tissue inhomogeneity.

2.2. Methods

2.2.1. Overview of the Conventional Technique for EP Measurement

Conventional techniques of measuring tissue EP use open-end coaxial probes in conjunction with VNAs as shown on Figure 2.1. As illustrated in this figure, the VNA transmits an electromagnetic wave (incident signal) into the coaxial probe which is pressed against the tissue sample at one end and attached to the VNA at the other end. The incident signal ($Vi\angle\beta$) propagates into the probe and hits the sample at the probe-sample interface region where part of it reflects back to the VNA through the probe due to the impedance mismatch. This reflected wave ($Vr\angle\alpha$) affects the amplitude and phase of the incident wave ($Vi\angle\beta$) in the coaxial probe. By measuring and analyzing the phase and amplitude of the incident and reflected waves, the VNA estimates the sample's impedance. Equations (2.1) and (2.2) show a fundamental relationship between incident and reflected waves and electrical impedance of the two sides of the probe-sample interface [38].

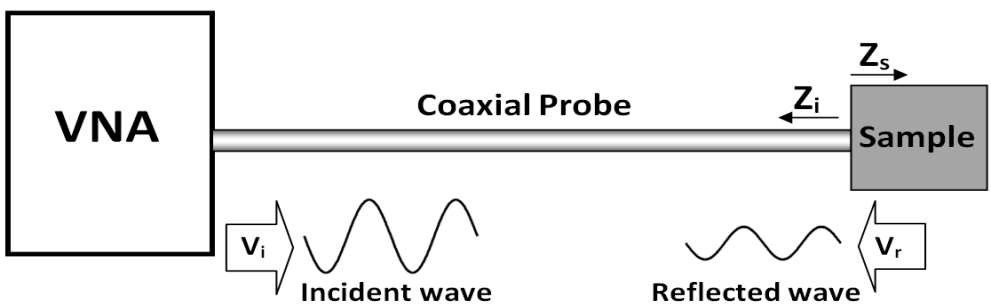

Figure 2.1. Schematic of the experimental setup used in conventional methods of tissue EP measurement.

The following equation, which is based on a lumped parameter approach, shows a fundamental relationship between incident and reflected waves and electrical impedance of the two sides of the probe-sample interface [37].

$$\Gamma = \frac{\mathrm{Vr}\,\angle\alpha}{\mathrm{Vi}\,\angle\beta} = \frac{Z_s - Z_i}{Z_s + Z_i} \qquad (2.1)$$

This leads to:

$$Z_s = \frac{(1+\Gamma)}{(1-\Gamma)}\, Z_i = \gamma Z_i \qquad (2.2)$$

where Γ is the reflection coefficient at the probe-sample interface, Vr and α are the amplitude and phase angle of the reflected wave, Vi and β are the amplitude and phase angle of the incident wave, Z_i is the impedance of the coaxial probe and Z_s is the impedance of the sample. Based on Equation 1, at low frequencies where the impedance of biological tissues is significantly higher than the impedance of coaxial probe (for instance 50kΩ or higher vs. 0.10kΩ at 10kHz [7-8, 34-35]) the reflection coefficient at the probe-sample interface becomes very close to 1, leading to a very large γ value. This implies that, at low frequencies, inevitable raw data measurement errors involved in the conventional EP measurement technique leads to highly magnified error in the tissue's EP estimation.

2.2.2. Overview of the Proposed Technique

The proposed EP measurement technique consists of tissue impedance data acquisition followed by data processing to estimate the tissue's EP. For tissue data acquisition, a freshly excised tissue specimen is placed between two plates of a custom-made impedance measurement sensor and the resultant resistance (R_m) and capacitance (C_m) values are measured at low frequencies as described in detail in Section 2.2.5. It is noteworthy that C_m depends on the geometry of the conductors and ε of the tissue while the latter is an intrinsic property of the tissue and does not depend on the charge or potential difference between the conductors. The following is a fundamental relationship that governs C of an arbitrarily shaped capacitor [15]:

$$C = \frac{\mathrm{Q}}{\mathrm{V}} = \frac{\oint \varepsilon E.\ ds}{\int E.\ dl} \qquad (2.3)$$

where Q is the electric charge, V is the voltage between electrodes, E is electric field, and $\varepsilon = \varepsilon_r\varepsilon_0$ where ε_r and ε_0 are medium's relative permittivity and vacuum's permittivity, respectively. Equation 3 shows that the relationship between C and ε is complex as E is spatially variable. E can be calculated by solving Maxwell's equation which can be achieved numerically using FEM. Equation 3 also shows that C depends on the geometry of the conductor plates and geometry and permittivity of the materials between them. Given that measured capacitance (C_m) is a complex function of ε_r which can be formulated numerically using FEM, inverse problem formulation can be used to calculate ε_r corresponding to measured C_m. As such, we use an algorithm based on the flowchart shown in Figure 2 to calculate ε_r using measured C_m data. In the proposed inverse FE framework, the forward model is an FE model of the sensor with the specimen as the sensor's capacitor dielectric. Given the known geometry of the sensor's plates and specimen and the electrical properties of the plates including their electrical conductance and permittivity, for any given input ε_r value of the tissue specimen, this FE model outputs a corresponding capacitance (C_c). As such, the inverse problem was formulated as a 1D optimization problem where ε_r is the unknown parameter to be determined. In this optimization problem, the calculation starts with an initial guess value of $\varepsilon_r = \varepsilon_{r0}$. This value is modified iteratively using the optimization algorithm until the difference between the sensor's capacitance value (C_c) calculated using the FE model and its measured counterpart (C_m) is minimum. The last ε_r value, which corresponds to this minimum difference, will be taken as the specimen's relative permittivity value.

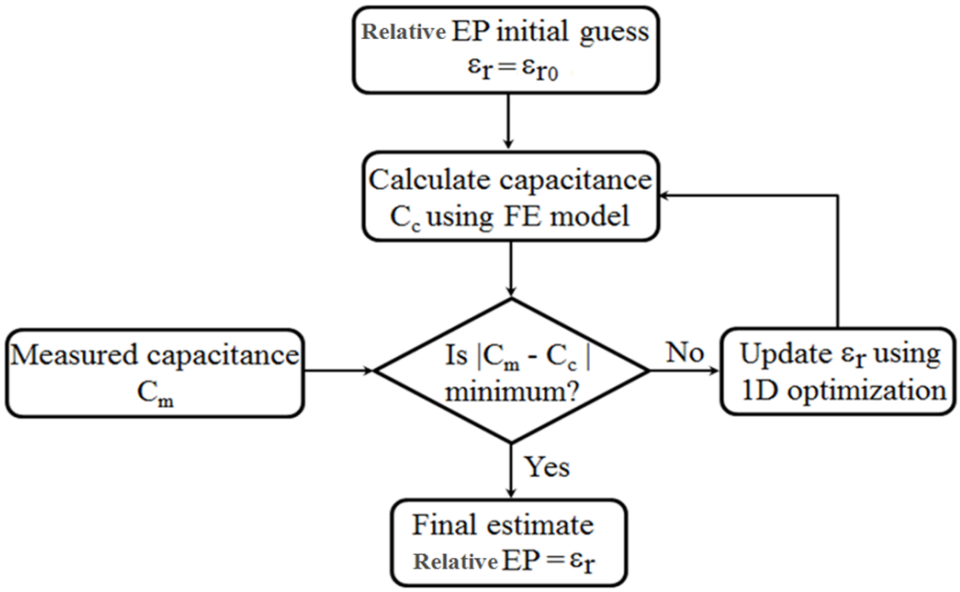

Figure 2.2. Flowchart of the inverse finite element algorithm used to estimate tissue specimen relative electrical permittivity

2.2.3. Ex-vivo sample preparation

Twenty nine bovine specimens were excised up to 4 hours post-mortem. They included 5 trabecular bone, 15 heart (5 from the right ventricle and the rest from the left ventricles) in addition to 9 liver specimens. The samples were mainly cut into block shaped specimens and their dimensions were recorded for their FE mesh generation which is required for EP calculation. We also cut some of the tissue into curved specimens with uniform thickness as shown in Figure 2.3. This was done to demonstrate the effectiveness of the proposed method in measuring EP of tissue specimens with arbitrary shape.

Figure 2.3. Samples of ex-vivo bovine specimens with arbitrary shapes used in the study.

2.2.4. Experimental setup for capacitance measurement

A schematic of the experimental setup used in this investigation is illustrated in Figure 2.4. As depicted in this figure, the capacitive sensor of the measurement system consists of two parallel conductive plates. The distance between the plates is adjustable to fit the specimen being measured so as to establish contact with its two sides. The plates have dimensions of 84mm × 46mm × 1mm. Connection between the sensor's plates and data acquisition (DA) circuit board was made via two pairs of shielded wires. The impedance measurement was carried out through a custom-designed DA system which benefits from a high resolution sigma-delta analog-to-digital converter (ADC). The DA board first measures the amplitude and phase of the current that passes through the sensor and send this information to the analog-to-digital converter. The ADC then converts the information to two 24-bit packets and feed them to the Digital Signal Processing (DSP) chip. The DSP chip then analyzes the phase and amplitude information and extracts the sample's capacitance. The capacitance data is then fed to an 8-bit micro-controller via I^2C interface. The micro-controller coordinates between different parts of the DA board and sends the capacitance data to a computer via USB ports. The architecture of this DA system features resolution of 24-bit no missing codes with up to 21-bit effective resolution, high linearity of ±0.01% and high accuracy of ±24 fF (calibrated) for measuring capacitance. The DA system's input capacitance range is 0-50 nF. The system uses $5V_{p\text{-}p}$ excitation pulse at frequency of 32 kHz to measure the impedance of the sensor ensemble.

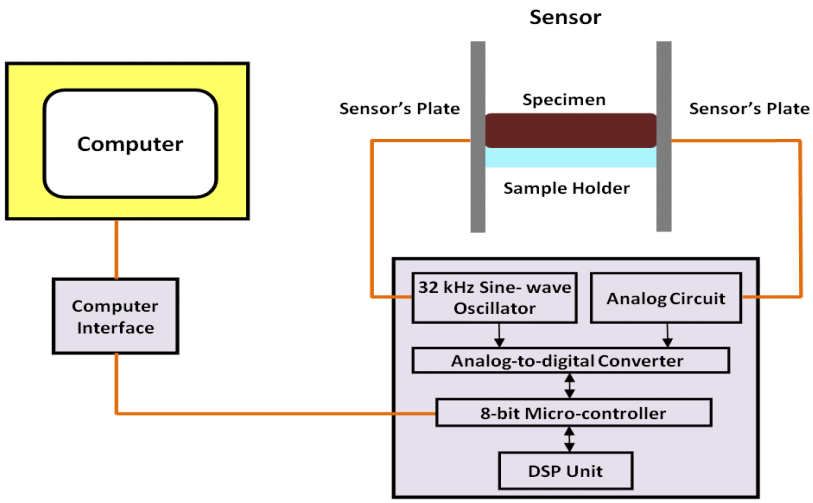

Figure 2.4. Schematic of the experimental setup for impedance measurement.

2.2.5. Optimization based inverse finite-element approach for EP calculation

As indicated earlier, the proposed EP measurement technique follows an inverse FE framework. The forward model in this framework is tissue specimen FE model while the inversion part utilizes a constrained optimization algorithm which seeks a relative EP value (ε_r) that leads to the closest match between the capacitance value obtained from the FE model (C_c) and its experimentally measured counterpart (C_m). For this purpose, an objective cost function representing the absolute difference between experimental and simulated capacitance values was defined. As such, ε_r value that minimizes the objective function is the sought relative electrical permittivity. Given that the range of relative permittivity values for biological tissues is known based on the literature, constrained (bounded) optimization was used to determine tissue ε_r such that the risk of convergence to local minima is minimized. Therefore, the constrained minimization problem is formulated as follows:

$$f(\varepsilon_r) = |\, C_m - C_c\,(\varepsilon_r)|$$

$$\begin{cases} \text{Min.}\, f(\varepsilon_r) \\ \text{sub. to}\ \varepsilon_{rL} \le \varepsilon_r \le \varepsilon_{rU} \end{cases}$$

Here C_m and $C_c(\varepsilon_r)$ are, respectively, the experimentally acquired capacitance value and its counterpart obtained from the FE model. We used lower bound ε_{rL} values of 100 and 1000 and upper bound ε_{rU} values of 5000 and 50000 for the trabecular bone and soft tissues (heart and liver specimens), respectively. The algorithm is launched with an input relative EP initial guess value. To systematically change this value, the bisection search algorithm [28] was used which finds a uni-modal function's minimum by successively narrowing the range of values where the minimum occurs. The optimization process is terminated when the current range becomes sufficiently small.

2.2.5.1. Sensor FE model

As stated earlier, the forward model of the problem involved in the proposed technique inputs data of the sensor including the specimen's geometry and ε_r and outputs corresponding capacitance. This model is formulated numerically using FEM which was implemented in CST Studio software package (Computer Simulation Technology AG, Darmstadt, Germany). This software calculates the electric field in the specimen by solving the governing Maxwell's equations before determining the capacitance value of the sensor ensemble using Equation 2.3. Figures 2.5(a) and (b) illustrate a side view and 3-D view of a coarse FE mesh of the sensor including a tissue sample cut into a curved specimen shape. This coarse mesh is illustrated for the purpose of clear visualization only as specimens' FE mesh generated by CST to achieve desired accuracy through iterative refinement typically consists of ~1.4-2.8 million 8-noded hexahedral elements in this application. The FE model requires the electrical conductance and permittivity values for each material within the sensor as input. As stated earlier, the tissue ε_r value is one of the key parameters that affects the overall capacitance of the sensor. In brief, for a known excitation voltage and known geometry, EC and ε_r parameters, the FE model outputs the C value of the capacitor.

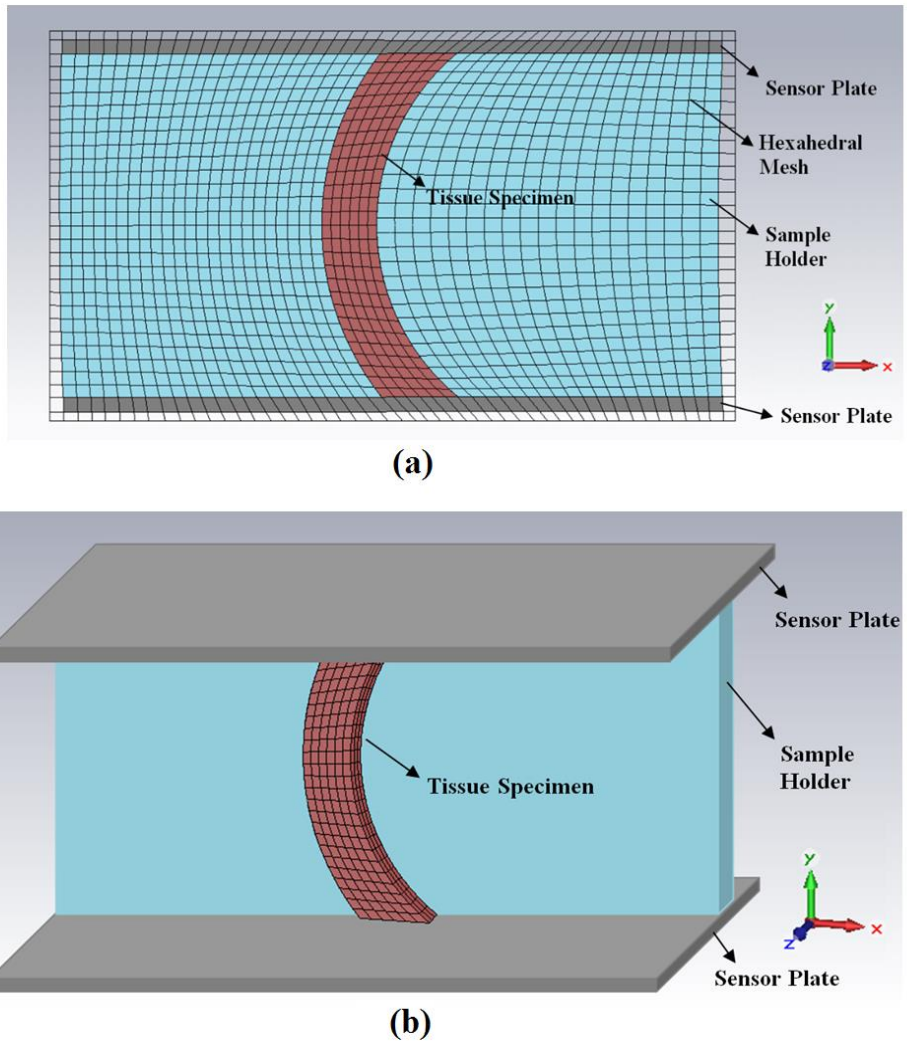

Figure 2.5. Side view of the finite-element model of the proposed sensor with a curved-shape specimen and (a), and 3-D view of the proposed sensor with the same curved-shape specimen (b).

2.2.6. Measurement sensitivity to specimen geometry

In order to assess the impact of sample's geometry errors, both gross and systematic, on accuracy of estimated ε_r of the sample was assessed. Such inaccuracy is expected because of errors encountered in specimen's dimensions measurement or segmentation of its image in case geometry is acquired through imaging. For this assessment, a block-shaped liver sample was selected and its dimensions of 41mm × 5mm × 5mm were accurately measured. These

dimensions which are considered to be the true dimensions, were altered to mimic gross and segmentation errors to determine the impact of such level of inaccuracy on the tissue reconstructed EP value. To mimic gross geometry errors, the dimensions were randomly altered by ±10% to generate 8 different altered geometries. For segmentation error simulation, two levels of isotropic errors of ±0.2mm and ±0.1mm were randomly added to the specimen's dimensions, each leading to 8 different altered geometries. The two segmentation error levels were considered for high and low image resolution scenarios. Each geometry was fed to the inverse FE-based algorithm to calculate the tissue's corresponding EP values using the original geometry and the variants geometries.

2.2.7. *In silico* assessment of measurement sensitivity to tissue specimen inhomogeneity

In some tissues such as the breast, acquiring a homogeneous specimen is challenging as the breast adipose and fibroglandular tissues are often intertwined where layers/pockets of adipose tissues are distributed within the fibroglandular tissue regions or vice versa. Such inhomogeneity is often not detectable visually. In order to assess the impact of inevitable biological tissue inhomogeneity on measured EP using the proposed technique versus the conventional approach, we conducted a computer simulation study where FE models of two breast tissue specimens with dimensions of 12mm × 12mm × 10.5mm were used. To mimic inhomogeneity, one of the specimens is assumed to consist of fibroglandular block of tissue with 10 mm thickness and ε_r = 2500 at 10 kHz with a very thin layer of adipose tissue of 0.5 mm thickness and ε_r = 500 at 10 kHz. The other specimen is assumed to consist of adipose tissue block with the same dimensions of 12mm × 12mm and 10 mm thickness and ε_r = 500 at 10 kHz with a very thin layer of fibroglandular tissue of 0.5 mm thickness and ε_r = 2500 at 10 kHz [7,31-33]. FE models of these specimens were constructed using the CST Studio Software followed by FE analysis of these models using the same software to obtain the specimen's capacitance in the two cases. These cases assumed using the two measurement methods of 1) open-end coaxial cable (core conductor diameter = 1.30 mm, shield conductor diameter = 5.72 mm) pressing against the tissue samples (Figure 2.6(a) and (b)), and 2.2) the proposed method of parallel plate sensor with the tissue specimen placed between them as described in Section 2.2.5 (Figure 2.6(c) and (d)), respectively.

The obtained capacitance values were used as input to calculate the specimens' ε_r using the conventional and proposed techniques.

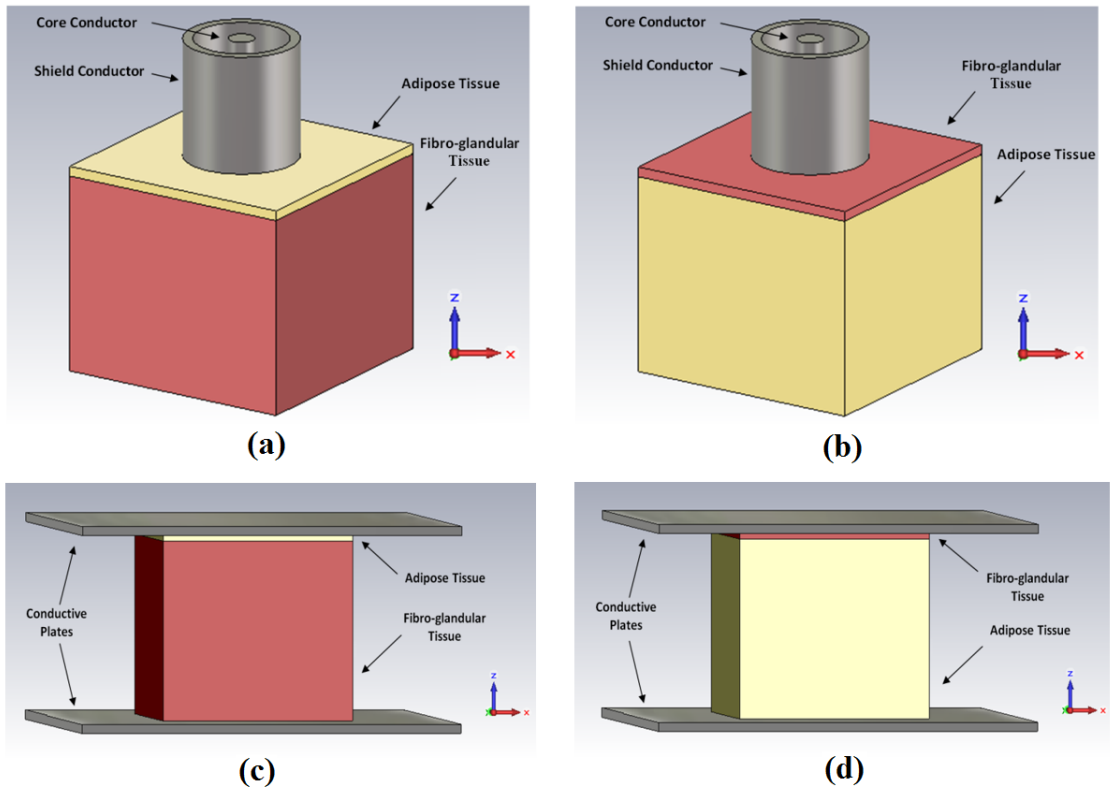

Figure 2.6. Schematics of inhomogeneous breast tissue specimen models consisting of fibroglandular and adipose tissues. They are shown with an open-end coaxial cable and parallel plate sensor used with the conventional measurement ((a) and (b)) and the proposed measurement techniques ((c) and (d)), respectively.

2.2.8. Methods validation

The proposed method in this study was validated by measuring the permittivity of a Plexiglas sheet at 32 kHz using the proposed measurement technique. The permittivity of the Plexiglas is known at 60 Hz-100 kHz range. According to the specifications provided by the manufacturer, from 60 Hz-100 kHz the relative permittivity of the Plexiglas ranges from 3.5 to 2.7 [29]. This measurement was conducted 10 times to account for experimental errors. The plexiglas specimen was plate shaped with dimensions of 50mm×48mm×1mm which led to a fine FE mesh of 75000 elements. This model was incorporated into the mathematical cost function of the optimization

algorithm used to calculate its relative EP. It noteworthy that plexiglass was chosen for validation in this study because its dielectric values were provided by the manufacturer at the low frequency range (60Hz-100kHz). Unfortunately for other materials and solutions such as saltwater with higher conductivity and permittivity, the reliable data pertaining to their dielectric values at low frequencies does not exist in the literature.

2.3. Results

2.3.1. Specimen's geometry sensitivity analysis

Using the "true" geometry of 41mm × 5mm × 5mm, the ε_r value of the blocked-shape liver tissue specimen was calculated at 28300. The first set of altered geometries corresponding to the geometry gross errors of ±10% led to ε_r estimation error of 3.4±17.1%. The two other sets of altered geometries led to ε_r estimation errors of 0.6±8.7% and 0.1±4.3% corresponding to the isotropic segmentation errors of ±0.2mm and ±0.1mm, respectively. These errors indicate that while relative EP estimation errors can be significant with gross geometry errors, they are insignificant with errors expected from image segmentation in case of imaging based geometry acquisition.

2.3.2. *In silico* assessment of measurement sensitivity to tissue specimen inhomogeneity

Capacitance values of the fibroglandular tissue specimen with a thin layer of adipose was calculated at 15.62 pF and 255.09 pF using the conventional method and FE model pertaining to the proposed setup, respectively. These differences can be explained by Figure 2.7 which illustrates the electrical potential and corresponding electric field pertaining to the conventional and proposed setups with this breast specimen model. Figures 2.7(a) and (b) illustrate the electric potential while Figures 2.7(c) and (d) illustrate the corresponding electric fields. For example, Figure 2.7(c), which corresponds to the conventional technique, shows that the electric field is close to zero within the entire tissue sample except for a small region underneath the coaxial cable. The field's depth penetration is very limited and barely reaches the fibroglandular tissue layer, leading to capacitance value which is predominantly determined by the permittivity of the thin adipose layer according to Equation 2.3. In contrast, Figure 2.7(d), which corresponds to the

proposed technique, shows significant non-zero electric field values throughout the entire sample including in the thick fibroglandular tissue layer. For the adipose tissue specimen with a thin layer of fibroglandular tissue, capacitance values of 46.45 pF and 63.19 pF were obtained using the FE models pertaining to the conventional and proposed experimental setups, respectively. Using these values, the ε_r values for the fibroglandular tissue were calculated at 650 and 2100 using the conventional and the proposed techniques, indicating errors of 74% and 16% corresponding to these techniques, respectively. The ε_r values obtained for the adipose tissue were calculated at 1850 and 520 using the conventional and proposed approaches, indicating errors of 270% and only 4% corresponding to these techniques, respectively.

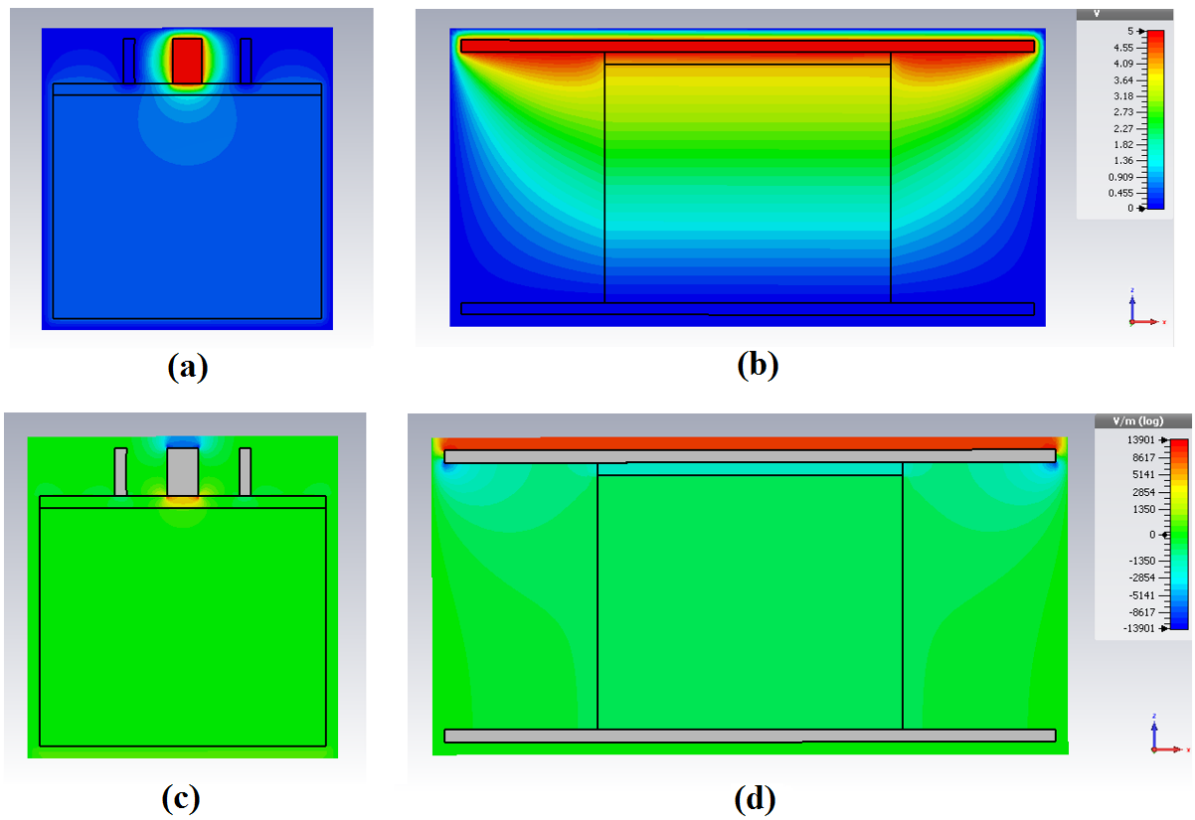

Figure 2.7. Simulated distributions of electric potential ((a),(b)) and electric field ((c),(d)) inside the inhomogeneous breast tissue specimen model consisting of fibroglandular tissue and a thin layer of adipose tissues. Simulated distributions were obtained with conventional ((a),(c)) and the proposed ((b),(d)) techniques.

2.3.3. Method validation results

For the methods validation, ε_r of the Plexiglas was measured at 2.9±0.15 with the excitation frequency of 32 kHz. Considering linear variation approximation of EP over the frequency range of 60 Hz-100 kHz, the given ε_r range of 3.5-2.7 leads to 3.24. This value is sufficiently close to the ε_r values measured in our validation experiment.

2.3.4. Tissue relative EP measurement results

ε_r values of the 35 bovine specimens, which were obtained using the proposed technique, are presented in Figure 8. These values are 12162±1800, 11630±1403, 31550±2391 and 283±20 for the left ventricle, right ventricle, liver and trabecular bone samples, respectively.

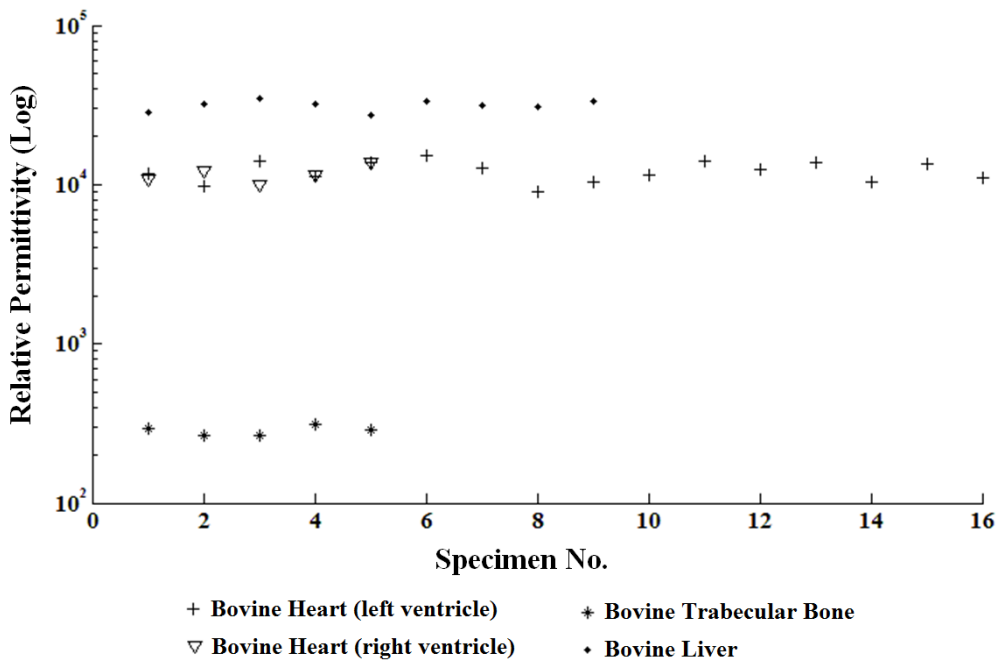

Figure 2. 8. ε_r values of bovine heart, liver and trabecular bone specimens at 32 kHz.

The standard deviations values pertaining to the measurements are only 14%, 12%, 7% and 7% of the corresponding average values of the left ventricle, right ventricle, liver and trabecular bone, respectively. This demonstrates relatively high repeatability of the proposed measurement

method, especially that the observed permittivity variations include inter and intra specimen variability in addition to experimental errors. It is noteworthy that in Figure 2.8, the left ventricle tissue specimens 11 to 16 correspond to the curved shape specimens while the rest correspond to the block shaped specimens. T-test was conducted to assess statistical differences between measured ε_r values of these two groups of specimens. The test led to $p = 0.5794$, indicating that the differences are not statistically significant. This consolidates that the proposed method is capable of estimating tissue ε_r accurately irrespective of the specimen's geometric complexity.

2.4. Discussion and Conclusions

The technique presented in this article was developed for measurement of relative EP of small ex-vivo tissue specimens. It uses an impedance sensor consisting of two parallel plates where the tissue sample is placed between the plates and acts as its dielectric. Compared to experimental setup used in conventional methods, this sensor is capable of measuring the sample's impedance with high accuracy especially at low frequencies, providing capacitance data which carries the ε_r information of the tissue specimen. To extract this information, we developed an inverse FE algorithm which inputs the measured capacitance, sensor's configuration data including the specimen's geometry, known electrical properties of sensor's plates and excitation voltage to output the tissue specimen's relative EP. Conventional EP measurement techniques were developed based on lumped parameter admittance data analysis model [7,10,17,18]. As described in Section 2.2.1, while these techniques may provide good ε_r measurement accuracy at higher frequencies, they are highly sensitive to raw data measurement errors at low frequencies. Electrode polarization is another issue which is encountered with very low frequencies. Schwan 1992 showed that electrode polarization at frequencies below 1kHz range may lead to inaccuracy in EP measurements. Electrode polarization usually increases with increasing sample conductivity, leading to inaccuracy of measured capacitance of ionic solutions and, to some extent, biological tissue [30]. With biological tissue specimens, however, the poorly conducting tissue structure shields the electrode from the ionic current, thus reducing the polarization effects [7]. Therefore, in the proposed method, electrode polarization is expected to have insignificant impact on measured ε_r. Another issue with ε_r measurement using the conventional techniques under low frequencies pertains to very limited penetration of electric field generated in the tissue specimen tested using conventional methods setup. As demonstrated in this study, limited

electric field penetration of conventional techniques may lead to high ε_r estimation errors for tissue specimens with even small amount of inhomogeneity. In contrast, through FE simulation, the proposed technique models the specimen's geometry, boundary conditions, and data pertaining to the measurement sensor highly accurately. Therefore, in principle, this technique offers a more rigorous method for EP measurement of biological tissues under wide range of frequencies and specimen size. The latter is particularly important for measuring EP of specimens routinely acquired from surgeries as these types of specimens are usually small and have irregular shapes. Furthermore, such tissues frequently include some level of inhomogeneity. For example, the breast volume mainly consists of fibroglandular and adipose tissue where these tissues are often intertwined. This is also true with breast tumors and other types of breast lesions which always involve a significant level of inhomogeneity. In Section 2.2.7, we conducted a simulation study to assess the impact of such inhomogeneity in measuring ε_r using the conventional and the proposed measurement techniques. With such inhomogeneous breast tissue specimens, results indicated that the conventional method may lead to errors of as high as 270% compared to a maximum error of only 16% obtained with the proposed method. This indicates that proposed method's sensitivity is significantly lower than the conventional methods' sensitivity to inevitable tissue inhomogeneity. In the proposed method, specimen geometry is an important input especially for measuring the permittivity of complex shaped tissue specimens acquired from surgeries. This geometry can be acquired by manual measurement or using imaging with digital cameras or by Computed Tomography (CT). The latter is advantageous as it is more accurate while it can provide information about tissue extent of inhomogeneity. To investigate the impact of errors in specimens geometry on the tissue estimated ε_r, three geometry error scenarios were investigated. One scenario involved large geometry alteration corresponding to gross geometry acquisition while the other two scenarios involved geometry alterations corresponding to image segmentation errors. This investigation indicated EP estimation errors of 3.4±17.1%, 0.6±8.7% and 0.1±4.3% corresponding to the first gross geometry acquisition, and two levels of image segmentation errors, respectively. These errors indicate that while ε_r estimation errors can be significant with geometry gross errors pertaining to manual measurement, they are insignificant with errors expected from image segmentation. To assess its accuracy, the proposed method was applied to measure the relative permittivity of a plexiglas specimen. At a frequency of 32 kHz, this measurement led to an average ε_r value of 2.9.

Unfortunately, the ground truth EP value of the Plexiglas specimen is not available at this frequency and values are available at frequencies of 60 Hz and 100 kHz. Using linear interpolation, an ε_r value of 3.24 was obtained which indicates an error of 10%. However, using more realistic convex interpolation function, which better represents ε_r variation versus frequency, leads to lower error. Such low error is anticipated given that the method is founded on a solid theoretical background in conjunction with the high sensitivity of the sensor and measurement system. The technique was used to measure ε_r of several fresh bovine tissue specimens including myocardium (left and right ventricles), liver and trabecular bone. Table 2.2 shows the ε_r values from the proposed technique for the heart, trabecular bone and liver specimens are within the reported ε_r range in the literature by previous researchers such as Gabriel et al. [7,8]. Due to the accuracy of the capacitance data processing model used in the proposed technique, the ε_r values obtained in this study are expected to have improved accuracy compared to the ones reported in the literature. To assess the effect of specimen geometry complexity on the measurement accuracy, some of the left ventricle tissue specimens were cut into curved shape samples while the rest were cut into block shaped samples. T-test at $p = 0.01$ indicated that the ε_r values obtained for the two groups of the left ventricle tissue specimens were not significantly different. It is noteworthy that temperature and dehydration can affect dielectric values of biological tissue. However, in this study the dielectric measurements of all bovine tissue specimens were conducted at room temperature (20° C) within 4 hours post-mortem and specimens were continuously kept moist during the experiment by using water spray.

Table 2.2. Comparison between bovine relative EP values obtained from the proposed technique and corresponding values reported in the literature for the same type of tissues at 32 kHz

Specimen's Type	**Mean ε_r ± STD**	**Reported ε_r in the Literature**
Bovine heart (LV, n=16)	12162±1800	10000 -20000 [6,7]
Bovine heart (LV, n=5)	11630±1403	
Bovine liver (n=9)	31550 ±2391	10000-30000 [6,7]
Bovine trabecular bone (n=5)	283 ± 19.5	200-300 [6,7]

The standard deviation of the measured relative EP values were at 7% to 14% of their corresponding average values. These values indicate high measurement repeatability as the corresponding variances include inter- and intra-specimen variability in addition to experimental errors. The ε_r measurement of bovine specimens in this study was performed at frequency of 32 kHz only. However, the proposed technique, can be used to measure ε_r of tissues at a wide range of frequencies. While feasible, this was beyond the scope of this work as the main objective of this research was to introduce the novel measurement technique and inverse FE based data processing algorithm and to demonstrate the effectiveness of ε_r measurement of tissues at low frequencies.

Funding

This research was supported by NSERC in addition to WGRS provided by Western University.

References

[1] Ryan J. Halter, Alex Hartov, John A. Heaney, Keith D. Paulsen, Alan R. Schned, Electrical Impedance Spectroscopy of the Human Prostate, IEEE Transactions on Biomedical Engineering, Vol. 54, No. 7, July 2007.

[2] Ryan J. Halter, Alan Schned, John Heaney, Alex Hartov, Keith D. Paulsen; Electrical Impedance Spectroscopy of Benign and Malignant Prostatic Tissues, DOI 10.1016/j.juro.2007.11.043.

[3] Ryan J. Halter, Alex Hartov, Keith D. Paulsen, A Broadband High-Frequency Electrical Impedance Tomography System for Breast Imaging, IEEE Transactions on Biomedical Engineering, Vol. 55, NO. 2, February 2008.

[4] Ryan J. Halter, Alan R. Schned, John A. Heaney, Alex Hartov; Passive Bioelectrical Properties for Assessing High- and Low-Grade Prostate Adenocarcinoma, The Prostate 71:1759-1767 (2011).

[5] Paul M. Meaney, Tian Zhou, Douglas Goodwin, Amir Golnabi, Elia A. Attardo, Keith D. Paulsen; Bone Dielectric Property Variation as a Function of Mineralization at Microwave Frequencies, International Journal of Biomedical Imaging, Volume 2012, Article ID 649612, 9 pages, doi:10.1155/2012/649612.

[6] Fernando A. Angarita, Ashlie Nadler, Siham Zerhouni, Jaime Escallon, Perioperative measures to optimize margin clearance in breast conserving surgery, Surgical Oncology 23 (2014) 81-91.

[7] S Gabriel, R W Lau and C Gabriel, The dielectric properties of biological tissues: III. Parametric models for the dielectric spectrum of tissues, Phys. Med. Biol. 41 (1996) 2271–2293.

[8] S Gabriel, R W Lau and C Gabriel, The dielectric properties of biological tissues: II. Measurements in the frequency range 10 Hz to 20 GHz, Phys. Med. Biol. 41 (1996) 2251–2269.

[9] A Peyman, A A Rezazadeh, C Gabriel; Changes in the dielectric properties of rat tissue as a function of age at microwave frequencies, Phys. Med. Biol. 46 (2001) 1617–1629 S0031-9155(01)21688-1.

[10] C Gabriel, A. Peyman, E. H. Grant; Electrical conductivity of tissue at frequencies below 1MHz, Phys. Med. Biol. 54 (2009) 4863–4878; doi:10.1088/0031-9155/54/16/002.

[11] C Gabriel and A. Peyman; Dielectric measurement: error analysis and assessment of uncertainty, Phys. Med. Biol. 51 (2006) 6033–6046.

[12] A Peyman, S J Holden, S Watts, R Perrott, C Gabriel; Dielectric properties of porcine cerebrospinal tissues at microwave frequencies: in vivo, in vitro and systematic variation with age, Phys. Med. Biol. 52 (2007) 2229–2245, doi:10.1088/0031-9155/52/8/013.

[13] A Peyman, C Gabriel, H R Benedickter, J Frohlich; Dielectric properties of human placenta, umbilical cord and amniotic fluid, Phys. Med. Biol. 56 (2011) N93–N98 doi:10.1088/0031-9155/56/7/N01.

[14] A Peyman, C Gabriel; Dielectric properties of porcine glands, gonads and body fluids, Phys. Med. Biol. 57 (2012) N339–N344, doi:10.1088/0031-9155/57/19/N339.

[15] David K. Cheng, P.215,5-7, Field and Wave Electromagnetics, Addison-Wesley, 1989.

[16] William T. Joines, Randy L. Jirtle, Marc D. Rafal, Daniel J. Schaefer; Microwave power absorption differences between normal and malignant tissue, International Journal of Radiation Oncology Biology Physics, Volume 6, Issue 6, June 1980, Pages 681–687.

[17] William T. Joines, Yang Zhang, Chenxing Li, Randy L. Jirtle; The measured electrical properties of normal and malignant human tissues from 50 to 900 MHz, Med. Phys. 21, 547 (1994).

[18] James Baker Jarvis, Michael D. Janezic, Paul D. Domich, Richard G. Geyer; Analysis of an Open-Ended Coaxial Probe with Lift-off for Nondestructive Testing, IEEE Transactions on Instrumentation and Measurement, Vol. 43, No. 5, October 1994.

[19] James Baker Jarvis, Michael D. Janezic, Bill F. Riddle, Robert T. Johnk, Pavel Kabos, Christopher L. Holloway, Richard G. Geyer, Chriss A. Grosvenor; Measuring the Permittivity and Permeability of Lossy Materials: Solids, Liquids, Metals, Building Materials, and Negative-Index Materials; Electromagnetics Division, National Institute of standards and Technology, U.S. Department of Commerce, 2004.

[20] S W Smye, J M Chamberlain, A J Fitzgerald, E Berry; The interaction between Terahertz radiation and biological tissue, Phys. Med. Biol. 2001, 46(9) R101 doi:10.1088/0031-9155/46/9/201.

[21] H Kawai, K Ito, M Takahashi, K Saito, T Ueda, M Saito, H Ito, H Osada, Y Koyanagi, K Ogawa; Simple modelling of an abdomen of pregnant women and its application to SAR estimation IEICE Trans. Commun.2006, E89-B 3401–10.

[22] P J Dimbylow, Development of pregnant female, hybrid voxel-mathematical models and their application to the dosimetry of applied magnetic and electric fields at 50 Hz Phys. Med. Biol.2006, 51 2383–94.

[23] P J Dimbylow; SAR in the mother and foetus for RF plane wave irradiation Phys. Med. Biol. 2007, 52 3791–802.

[24] Nagaoka T, Togashi T and Saito K, An anatomically realistic whole body pregnant woman model and specific absorption rates for pregnant woman exposure to electromagnetic plane waves from 10 MHz to 2 GHz Phys. Med. Biol. 2007, 52 6731–45.

[25] Togashi t, Nagaoka T, Kikuchi S, Kazuyuki S, Watanabe S, Takahashi M and Ito K, FDTD Calculations of specific absorption rate in foetus caused by electromagnetic waves from mobile radio terminal using pregnant woman model, IEEE Trans. Microw. Theory Tech. 2008, 56 554–9.

[26] Dimbylow P J, Nagaoka T and Xu X G 2009 A comparison of foetal SAR in three sets of pregnant female models, Phys. Med. Biol. 54 2755–67.

[27] McIntosh R L, Deppeler L, OlivaM, Parente J, Tambuwala F, Turner S,Winship D and Wood A W2010 Comparison, of radiofrequency exposure of a mouse dam and foetuses at 900 MHz Phys. Med. Biol. 55 N111–22.

[28] W.H. Press, S.A. Teukolsky, W.T. Vetterling, B.P. Flannery, 1992. Numerical Recipes in Fortran 77. The Art of Scientific Computing. Cambridge University Press, Cambridge.

[29] Physical Properties of 0.236" Plexiglas sheet (ACP Noxtat base substrate material), ACP Noxtat, Santa Ana, CA, USA.

[30] Schwan HP; Linear and nonlinear electrode polarization and biological materials, Ann Biomed Eng. 1992; 20(3): 269-88.

[31] M. Lazebnik, L. McCartney, D. Popovic, C.B. Watkins, M.J. Lindstrom, J. Harter, S. Sewall, A. Magliocco, J.H. Booske1, M. Okoniewski, and S.C. Hagness, "A large-scale study of the ultrawideband microwave dielectric properties of normal breast tissue obtained from reduction surgeries," Phys. Med. Biol., vol. 52, pp. 2637-2656, 2007.

[32] M. Lazebnik, D. Popovic, L. McCartney, C.B. Watkins, M.J.Lindstrom, J. Harter, S. Swall, T. Ogilvie, A. Magliocco, T. M. Breslin, W. Temple, D. Mew, J.H. Booske1, M. Okoniewski, and S.C. Hagness, "A large-scale study of the ultrawideband microwave dielectric properties of normal, benign and malignant breast tissues obtained from cancer surgeries," Phys. Med. Biol., vol. 52, pp. 6093-6115, 2007.

[33] Majid Ostadrahimi, Arman Vahedi, Faezeh Safari, Ryan Reopelle, Sima Noghanian, Stephen Pistorius, A Heterogeneous Breast Phantom for Microwave Breast Imaging, 31st Annual International Conference of the IEEE EMBS, Minneapolis, Minnesota, USA, September 2-6, 2009.

[34] H. Mokhtari, A. Nyeck, C. Tosser-Roussey, A. Tosser-Roussey; Finite difference method and Pspice simulation applied to the coaxial cable in a linear temperature gradient; IEEE Proceedings-A, Vol. 139, No. I, January 1992.

[35] B. Hyland; An Improved and Simple Cable Simulation Model; APP 5141: Oct 22, 2012; Maxim Integrated Products, Inc.; San Jose, California, USA.

[36] David M. Pozar; Microwave Engineering, Fourth edition, Wiley Global Education, 2011, P28-29.

Chapter 3

Dielectric Properties of the Normal and Malignant Breast Tissues in Xenograft Mice at Low Frequencies (100Hz-1MHz)

The material presented in this chapter has been submitted to the Measurement journal.

Authors' Contributions Statement: *The main idea of this chapter is conceived by the principal author, Seyyed M. Hesabgar. The research, experiments and tissue dielectric measurements presented in this chapter have been conducted by Seyyed M. Hesabgar and guided by the research supervisor Dr. Abbas Samani. The preparation of the xenograft mice model for this study were instructed by the collaborators of this study, Dr. Ali Sadeghi Nainai and Dr. Gregory Czarnota at University of Toronto. The injection of the breast cancer cell lines and excision of the breast tumors from xenograft mice for this study were conducted by the collaborators' technicians in the Odette Cancer Centre in Toronto, Ontario.*

3.1. Introduction

Breast cancer is the most common type of cancer in women. In 2012, ~1.7 million new cases were diagnosed worldwide, accounting for 25% of all new cancer cases in women [1]. Breast cancer survival rate in low-income countries is only 40% compared to over 80% in North America [2]. Low survival rates in less developed countries is mainly attributed to lack of early detection. This indicates the paramount role that early detection plays in increasing breast cancer survival rate. Among methods developed for breast cancer early detection, novel medical

imaging techniques are very promising. One of the methods pursued for this purpose is based on imaging tissue electrical properties as it does not involve ionizing radiation.

Tissue dielectric properties (e.g. electrical permittivity (EP)) span a wide range of values [4,5]. Particularly, malignant tumors have been shown to have substantially different EP from healthy breast tissue [6-9]. These differences stem from tissue structural alterations associated with cancer biology. Research has shown that higher dielectric properties of malignant breast tissues is due to their higher than normal water and ions concentration [10] and lower than normal fat content [11]. While higher concentration of ions and salt in the tissue intra and extra cellular matrix leads to a higher conductivity and permittivity at all frequencies [5], lower concentration or lack of adipose elevates its dielectric properties. This is consistent with the breast's lower dielectric properties of adipose tissue compared to those of fibroglandular and connective tissues [4,5]. Another source of dielectric properties elevation is higher cell density which is a well-known feature characterising cancerous tissue [12]. This implies that dielectric properties imaging can potentially produce high contrast images with rich diagnostic information, hence it holds a good promise for breast cancer early detection and diagnosis. As such, accurate dielectric measurement of healthy and pathological breast tissues can help further development of dielectric property imaging techniques as having reliable EC and EP data pertaining to various breast tissues is essential for effective interpretation of EC and EP images.

Dielectric properties of normal and malignant tissues such as those of the breast and liver have been studied by many researchers in the past century [13-17]. While valuable in terms of laying theoretical foundations of the field, many of these studies including most of the early works, involve theoretical over-simplification and measurement setups capable of providing only limited accuracy [3]. More recent studies in this area are dominated by tissue dielectric properties measurement at high frequencies using vector network analyzer (VNA) and coaxial probe. These studies have shown that dielectric properties of pathological tissues at high frequency (10 MHz-20 GHz) are substantially different from their healthy tissue counterparts. This demonstrates good potential of imaging these properties at high frequencies for detecting and classifying tissue abnormalities especially those arising from cancer.

Despite that imaging dielectric properties at low frequencies (100 Hz-1MHz) has substantial merits, relatively little research has been carried out for reliable electrical characterization of tissues at such frequencies. Among those who have conducted dielectric measurements on

biological tissues at high frequencies, Joines et al. [10] measured electrical conductivity and permittivity of various normal and malignant human tissues at 50-900 MHz They concluded that, at all frequencies, both conductivity and permittivity parameters have greater values in malignant tumors than in corresponding normal tissue. O'Rourke et al. [17] measured dielectric properties of *ex vivo* and *in vivo* normal and malignant cirrhotic liver tissues at frequency range of 0.5-20 GHz. They indicated that at the mentioned frequency range, the dielectric properties of *ex vivo* malignant liver tissue are higher than those of normal liver tissues while differences in the dielectric properties of *in vivo* malignant and normal liver tissues are not statistically significant.

Preclinical animal tumor models, including tumor xenografts, are known to share main characteristics of their human tumor counterparts. As such, they are commonly used in novel techniques developmental stages or to acquire preliminary data. Xenograft mice models have been used extensively in breast cancer studies over the past decades. Despite some limitations, the similarities between these models and clinical human breast cancer are quite substantial. Histological studies of various adenocarcinoma xenograft models show close similarities between these models and their human counterparts [18]. In the area of breast cancer, studies have also shown that breast cancer xenograft models exhibit similar structural and functional characteristics of corresponding human breast cancers [19, 20]. Among those who used xenograft mice models for dielectric measurement, Yoo et al. [21] conducted EP measurement on brain, breast, gastric and colon carcinomas at 0.5-5 GHz using a measurement system consisting of vector network analyzer (VNA) and coaxial cable. Their finding suggests that relative permittivity values of the brain, breast and colon cancer tissues at these frequencies are higher than those of their normal tissue counterpart. Cho et al. [22] also conducted *in vivo* measurements of breast carcinoma dielectric properties in xenograft mice at 0.5-20 GHz frequency range using a similar system comprised of VNA and coaxial cable. Based on significant differences they observed in the dielectric properties of the tested tissues, they concluded that imaging tissue dielectric properties at microwave frequencies can be used to detect cancer with high sensitivity and specificity. These studies indicate that while breast tissue dielectric properties at high frequencies are relatively well studied, data that can be reliably used to interpret breast dielectric property images acquired at low frequencies are scarce. It is noteworthy that imaging dielectric properties at low frequencies is advantageous as the dissipation of electromagnetic field and energy absorption of biological tissues is low due to the

tissue low conductance at such frequencies [3-5]. This may imply higher level of safety with imaging dielectric properties at low frequencies. Furthermore, at these frequencies generation of electromagnetic waves necessary for tissue stimulation and data acquisition is easier and more cost-effective as the electronics involved in imaging at such frequencies is simpler and more readily available.

Conventional VNA-based dielectric measurement techniques assume semi-infinite geometry model as well as a high frequency excitation for tissue specimens [5,9,23]. The semi-infinite geometry model is reasonably accurate with relatively large tissue specimens excited at high frequencies. As such while these techniques provide reasonably good measurement accuracy to measure dielectric properties of large tissue specimens at high frequencies, they are inadequate for measuring low frequency dielectric properties of small tissue routinely obtained from surgical procedures.

The goal of this study is to estimate low frequency electrical permittivity and conductivity of small samples of human breast cancer tumor using a xenograft mice model. Comparison of these parameters in tumors and their normal surrounding tissues can help assessing the viability of imaging systems designed to image these properties at low frequencies as well as evaluating their efficacy for breast cancer screening or diagnosis.

3.2. Methods

When a biological tissue is placed inside an electric filed, energy of the field inside the tissue is primarily lost by either frictional motion of the tissue constituent charge carriers (resistive loss), or stored by polarization. As such, the response of tissue stimulated by electric field is described by its conductivity (σ, in S/m) and permittivity (ε, in F/m). Conductivity is a measure of the tissue ability to let charges pass through it, whereas permittivity is a measure of resistance the tissue exhibits when electric field is formed inside it. In the proposed tissue dielectric measurement technique, the sample excitation and data acquisition was performed by using a custom-made measurement setup. To measure tissue specimen's conductivity and permittivity the acquired data is processed within an inverse problem framework as described in the following sections.

3.2.1. Tissue Sample Preparation

In this study, experiments were conducted using human breast cancer (MDA-MB-231) tumor xenografts grown on hind legs of severely compromised immunedeficient (SCID) mice (n = 5). Tumors reached a size of 8–10 mm in diameter at 8 weeks after injection of cells subcutaneously. Cell lines were obtained from American Type Culture Collection (ATCC, Manassas, VA). For ultrasound imaging, the mice were anesthetized using (100 mg/kg ketamine, 5 mg/kg of xylazine, and 1 mg/kg of acepromazine, CDMV, St. Hyacinthe, Quebec, Canada) and the tumor and surrounding tissue were epilated before scanning (NairTM Church & Dwight Co., Canada). For in vivo tumor visualization, low and high frequency ultrasound b-mode images were acquired using a Sonix RP (Ultrasonix, Vancouver, Canada) system with a L14-5/38 transducer (10 MHz transmit frequency), and a Vevo 770 system (Visual Sonics, Toronto, Canada) with a RMV-707B transducer (30 MHz transmit frequency). The animals were subsequently euthanized and the tumor and surrounding normal tissue were excised. The specimens included five breast tumors and five normal surrounding tissue samples. The dimensions of each sample were measured and recorded for their FE mesh generation which is required for the specimen's dielectric calculation as described later. Histological analysis was carried out on tumor and normal tissue samples immediately after the electrical data acquisition. The samples were fixed in 5% formalin for 24–48 h and then sectioned in two representative planes with haematoxylin and eosin (H&E) staining. Microscopy was carried out using a Leica DC100 microscope with 20× and 40× objectives and a Leica DC100 camera connected to a 2 GHz PC running Leica IM1000 software (Leica GmbH, Germany). This study was conducted with research ethics approval from the Animal Care Committee of Sunnybrook Research Institute, Toronto, Canada (Protocol No. 11-440).

3.2.2. Experimental Setup for Impedance Measurement

As depicted in Figure 3.1, the setup consists of a plexiglas holder, electrodes, wires, a 1 nF ceramic capacitor, a high input impedance buffer, an excitation source and an oscilloscope. The electrodes are made from brass and they are 3 mm in diameter. Within few minutes from excision, each freshly excised specimen at room temperature (20° C) was placed between the electrodes such that its top and bottom surfaces only touched by the two electrodes. The top

electrode was connected to an excitation source which provided sinusoidal signal with 4 V_{p-p} amplitude and 100 Hz to 1 MHz frequency. The bottom electrode was connected to one end of a 1 nF ceramic capacitor. The other end of this capacitor, which forms a series circuit with the tissue sample at higher frequencies, was connected to ground. The phase angle and amplitude of the capacitor's voltage at each frequency was measured by an oscilloscope through a high input impedance buffer. This buffer, which is made from a unity-gain wideband operational amplifier (AD811, Analog Devices, USA), isolates the impedance of the tissue sample and the 1 nF series capacitor from the low impedance of the oscilloscope's probe such that the probe's low impedance does not interfere with the sample's impedance.

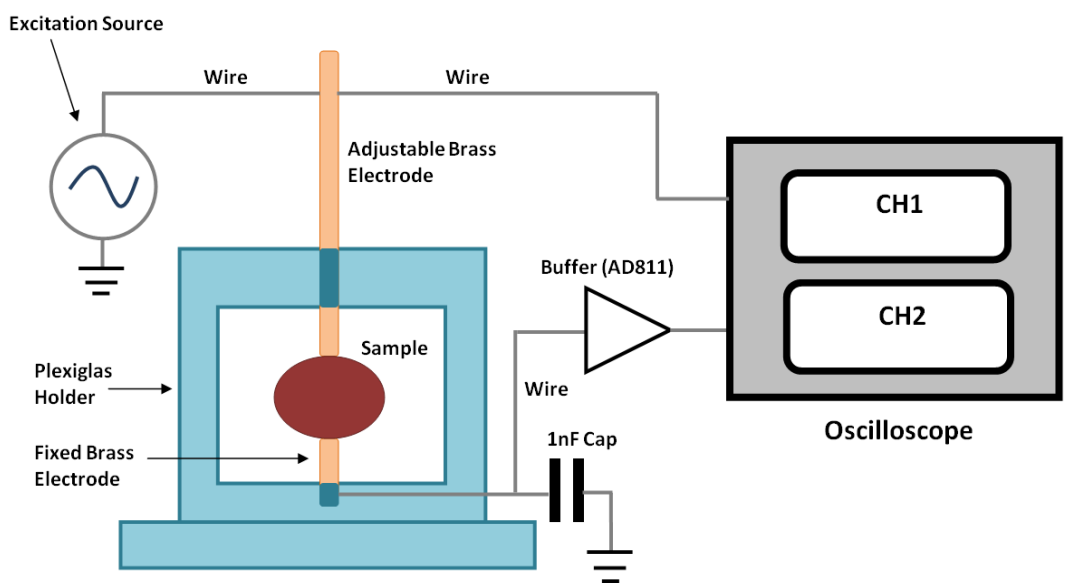

Figure 3.1. Schematic of the experimental setup for measuring a tissue specimen impedance

3.2.3. Electrical Model of the Tissue Sample in the Impedance Measurement Setup

The proposed technique involves measuring the specimen's lumped model electrical impedance amplitude and phase angle, Z_s and Φ_s shown in Figure 3.2. This is followed by FE model based data processing of Z_s and Φ_s to estimate the tissue's electrical permittivity and conductivity. Circuit analysis necessary to derive relationships used to estimate Z_s and Φ_s from data acquired from the apparatus is described here. Figure 3.2 shows the electrical model of the tissue sample

along with the circuit schematic used for measuring the sample's impedance. As shown in this figure, the tissue sample is modeled as an unknown impedance ($Z_s\angle\Phi_s$) which is connected to the 1 nF capacitance in series. R_2 and C_3 are the input resistance and capacitance of the buffer (AD811). In the figure, Vs and θ_1 are the amplitude and phase of the excitation voltage source, respectively while V_0 and θ_0 are the amplitude and phase of the voltage of the 1 nF series capacitance, respectively. Both of $Vs\angle\theta_1$ and $Vo\angle\theta_0$ are measured by the oscilloscope in the setup.

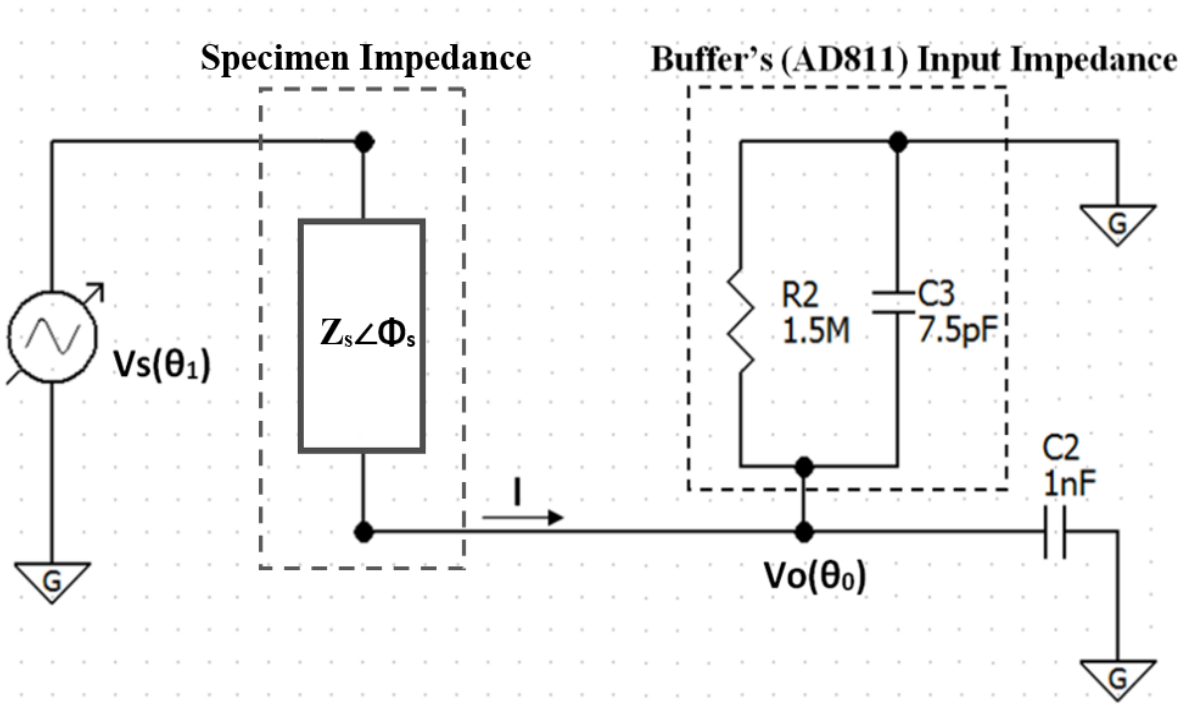

Figure 3.2. Electrical model of the tissue sample and required circuit for measuring sample's impedance

I is the current that passes through the main branch of the circuit. Specimen's electrical permittivity and conductivity are estimated using the amplitudes and phase angle of the sample's Z_s and Φ_s which are calculated as follows. Kirchhoff's current and voltage laws (KCL and KVL [24]) in phasor format lead to:

$$(Vo\angle\theta_0)/(Vs\angle\theta_1) = [Z_0\angle\Phi_0]/ [Z_s\angle\Phi_s + Z_0\angle\Phi_0] \qquad (3.1)$$

where $Z_0\angle\Phi_0 = (R_2 \parallel C_3 \parallel C_2)$ and $Z_s\angle\Phi_s$ is the specimen impedance, which is in series with $Z_0\angle\Phi_0$ leads to:

$Z_s = Z_0(Vs-Vo)/Vo$ (3.2) which in turn yields the following:

$Z_s\angle\Phi_s = Z_0\angle\Phi_0\,[Vs\angle\theta_1 - Vo\angle\theta_0] / Vo\angle\theta_0$ (3.3)

$\Gamma\angle\beta$ is defined as: $\Gamma\angle\beta = Vs\angle\theta_1 - Vo\angle\theta_0$ which yields the following:

$$\Gamma = \sqrt{(Vs\,\mathrm{Cos}\,\theta_1 - Vo\,\mathrm{Cos}\,\theta_0)^2 + (Vs\,\mathrm{Sin}\,\theta_1 - Vo\,\mathrm{Sin}\,\theta_0)^2},\ \beta = \mathrm{Arctg}\left(\frac{Vs\,\mathrm{Sin}\,\theta_1 - Vo\,\mathrm{Sin}\,\theta_0}{Vs\,\mathrm{Cos}\,\theta_1 - Vo\,\mathrm{Cos}\,\theta_0}\right)$$

(3.4)

$\Phi_s = \Phi_0 + \beta - \theta_0$ (3.5)

3.2.4. Tissue Conductivity and Permittivity Calculation

To calculate the specimen's tissue conductivity and permittivity, the calculated Z_s and Φ_s are used within an inverse FE framework. Figure 3.3 shows a flowchart summarizing the inverse finite element algorithm applied to estimate the tissue's conductivity and permittivity using the acquired impedance amplitude and phase angle data. In the inverse FE framework, FE model of the tissue specimen's impedance amplitude and phase angle including the two electrodes in the experimental setup represent the forward model. Given the known geometry of the electrodes and specimen and the electrical properties of the electrodes including their electrical conductance and permittivity, for any input tissue σ and ε values, the forward model outputs the impedance amplitude and phase angle. As such, the inverse problem was formulated as a 2D optimization problem where σ and ε are the unknown parameters to be determined. In this optimization problem, the calculation starts with the initial guess value for σ_0 and ε_0. These values are modified iteratively using the optimization algorithm until the difference between the specimen's impedance amplitude and phase values, Z_c and Φ_c calculated using the FE model and their measured counterparts (Z_s and Φ_s) become minimum. The last σ and ε value, which corresponds to this minimum difference, will be taken as the specimen's EC and EP values.

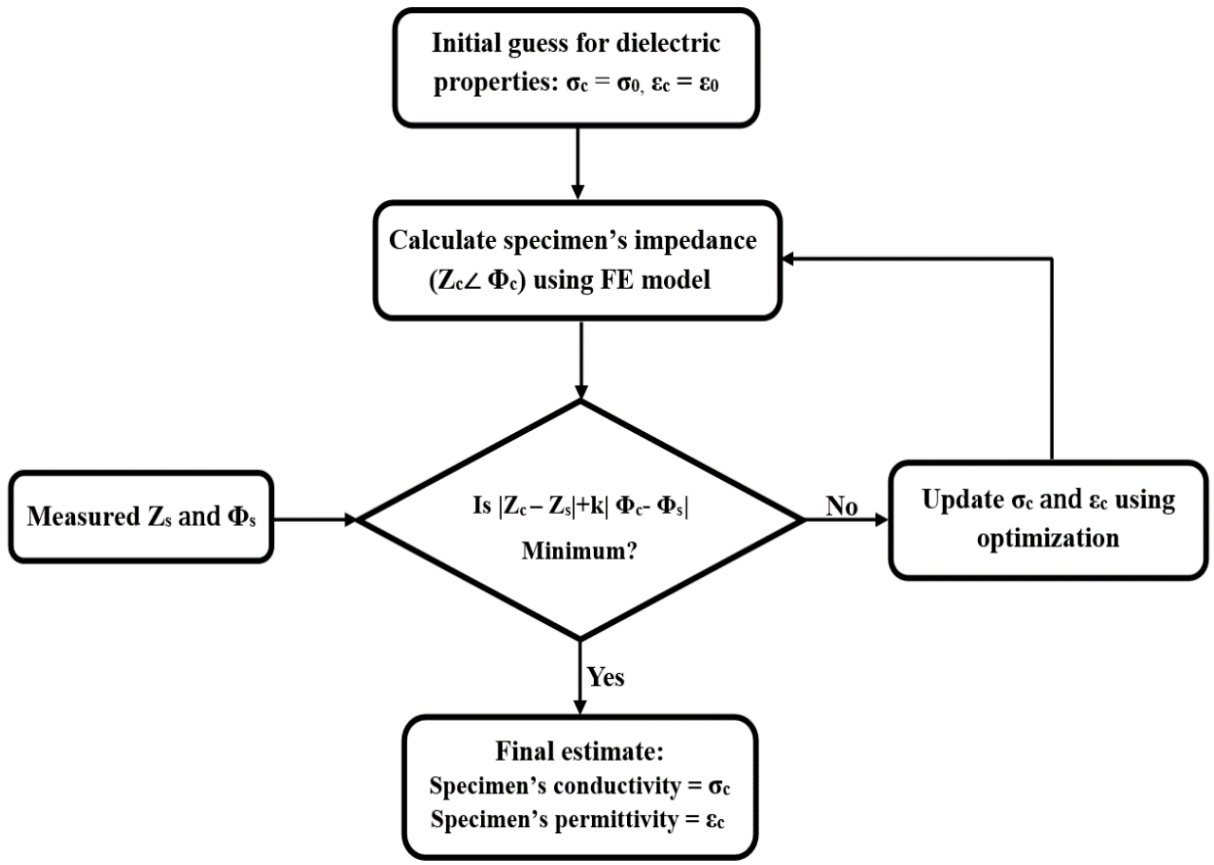

Figure 3.3. Flowchart of the inverse finite element algorithm used to estimate tissue specimen dielectric properties

3.2.5. Specimen FE Model and Maxwell Equations

To develop specimen's finite element (FE) model in this study, Comsol Multiphysics software package (COMSOL, Inc., MA, USA) was used. This software package uses finite element computational method to calculate the electric field and obtain the sample's impedance amplitude and phase angle values by solving the governing Maxwell's equations. For a nonmagnetic material such as biological tissues, the general format of Maxwell's equations in time domain with the inclusion of displacement current and continuity equation are [25]:

$$\nabla \cdot \mathbf{J}(r, t) = -\frac{\partial \rho(r, t)}{\partial t} \quad \text{(continuity equation)} \qquad (3.6)$$

$$\nabla \cdot \mathbf{D}(r, t) = \rho(r, t) \qquad (3.7)$$

$$\nabla \times \mathbf{H}(r, t) = \mathbf{J}(r, t) + \frac{\partial \mathbf{D}(\mathbf{r},\mathbf{t})}{\partial t} \quad (3.8)$$

$$\nabla \cdot \mathbf{B}(r, t) = 0 \quad (3.9)$$

$$\nabla \times \mathbf{E}(r, t) = -\frac{\partial \mathbf{B}(r,t)}{\partial t} \quad (3.10)$$

Where ρ(r, t) is electric charge density, J(r, t) is electric current density, E(r, t) is electric field, D(r, t) = εE(r, t) is electric displacement current, ε is electric permittivity, B(r, t) is the magnetic field, H(r, t) = B(r, t)/μ is magnetic intensity and μ *is* magnetic permeability which is considered to be as the same as the permeability of vacuum for the biological tissues. It is assumed in this study that B (r, t) = 0 and impedance measurements are done at low frequencies (1MHz or lower) where voltage source frequency is low enough for the electromagnetic field propagation delay to be neglected [25]. Using the phasor format of the above equation and dropping the time harmonic, the format of Maxwell equations which are used by Comsol Multiphysics [26] in frequency domain is:

$$\nabla \cdot \mathbf{J}(\omega) = \mathbf{Q}_j(\omega) \quad (3.11)$$

$$\mathbf{J}(\omega) = \sigma\mathbf{E}(\omega) + j\omega\mathbf{D}(\omega) + \mathbf{J}_e(\omega) \quad (3.12)$$

$$\mathbf{E}(\omega) = -\nabla\mathbf{V}(\omega) \quad (3.13)$$

n. J = 0 (current density is set to zero for boundary condition)

Where Q_j represents current source, σ electrical conductivity, ω natural frequency, J_e externally induced current density and V electric potential [25]. Comsol uses finite element method to solve equations 3.11- 3.13 and obtain the impedance amplitude and phase angle for each specimen in the forward problem.

3.2.6. Inverse Finite-Element Approach for EP Calculation

The measurement technique proposed in this study follows an inverse FE framework. The forward model in this framework is the tissue specimen FE model while the inversion part utilizes a constrained optimization algorithm which finds EP and EC values that leads to the best match between dielectric values obtained from the specimen's FE model and its measured counterpart.

3.2.6.1. Specimen FE Model

To develop a specimen's FE model in this study, Comsol Multiphysics software is used. As described earlier, this software package uses the FEM computational method to calculate the electric field in the specimen by solving the governing Maxwell's equations before determining the impedance amplitude and phase angle values. Figure 3.4 illustrates a coarse FE mesh of a tissue sample used in this study. This coarse mesh is illustrated for the purpose of clear visualization only as the specimens' FE meshes generated by Comsol to achieve desired accuracy through iterative refinement typically consist of ~0.7-1.2 million 8-noded hexahedral elements in this application. The FE model requires the electrical conductance (EC) and electrical permittivity value of each material used in the experimental setup including the EC and EP of the specimen. As stated earlier, the tissue EC and EP values are the key parameters that affects the overall impedance amplitude and phase angle. The EC and EP values of the electrodes and Plexiglas holder are known while those of the specimen's tissue are unknown. In brief, for known excitation voltage and geometry and EC and EP parameters of various material parts in the sensor, the FE model outputs the impedance amplitude and phase angle of the electrodes/specimen assembly.

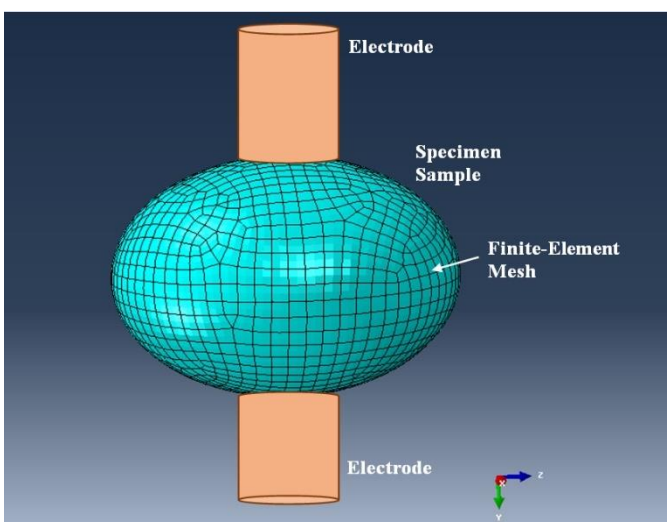

Figure 3.4. Finite-element model of one of the specimens used for measuring permittivity.

3.2.7. Tissue Dielectric Calculation Using Optimization

As indicated earlier, for obtaining the specimens' conductivity and permittivity using the measured impedance ($Z_s\angle\ \Phi_s$), optimization was used to solve the nonlinear inverse finite element problem developed in the proposed technique. In this optimization algorithm, we seek a conductance (σ) and permittivity (ε) values that leads to the closest match between the impedance values obtained from the FE model and its experimental counterpart. For this purpose, an objective cost function representing the absolute weighted difference between experimental and simulated impedance values (amplitude and phase angle) was defined. As such, conductance and permittivity values (σ and ε) that minimize the objective cost function are the desired conductivity and permittivity values. Given that the range of conductivity and permittivity for biological tissues are known based on the literature, constrained (bounded) optimization was developed to determine tissue conductivity and permittivity such that the risk of convergence to local minima is minimized. Therefore, the constrained minimization problem is formulated as follows:

$$f(\sigma, \varepsilon) = |Z_s(\sigma, \varepsilon) - Z_c(\sigma, \varepsilon)| + K\,|\Phi_s(\sigma, \varepsilon) - \Phi_c(\sigma, \varepsilon)| \qquad (3.16)$$

$$\begin{cases} Min.\, f(\sigma, \varepsilon) \\ sub.\, to\ \sigma_L \le \varepsilon \le \sigma_U\ and\ \varepsilon_L \le \varepsilon \le \varepsilon_U \end{cases}$$

Where $Z_s(\sigma, \varepsilon)$ and $\Phi_s(\sigma, \varepsilon)$ are amplitude and phase angle values of the specimen's impedance which are obtained experimentally and $Z_c(\sigma, \varepsilon)$ and $\Phi_c(\sigma, \varepsilon)$ are the amplitude and phase angle values of the specimen's impedance which are acquired from the FE computational model. K is the scaler coefficient with the value of 150. We used the lower bound values (σ_L and ε_L) of 10^{-3} and 1 and the upper bound values (σ_U and ε_U) of 10^2 and 10^7 for the specimen's conductance and relative permittivity, respectively. The algorithm is launched with an initial input values for the σ and ε. To systematically change these values, the 2-dimensinal Bi-section search algorithm [27] was used which finds a uni-modal function's minimum by successively narrowing the range of values where the minimum occurs. The optimization process is terminated when the current range becomes sufficiently small.

3.2.8. Methods Validation

The proposed method in this study was validated by measuring the conductivity and relative permittivity (ε_r) of a Plexiglas block at 60Hz-100kHz using the proposed measurement technique. The conductivity and relative permittivity of the Plexiglas is known at 60Hz-100kHz frequency range. According to the specifications provided by the manufacturer, from frequencies of 60Hz-100 kHz the σ and ε_r of the Plexiglas ranges from 0.0001 to 0.00016 and 3.5 to 2.7, respectively [28]. This measurement was conducted for 10 times to account for experimental errors. The mentioned Plexiglas specimen was plate shaped with dimensions of 28mm×28mm×1mm which led to a fine FE mesh of 77800 elements. This model was incorporated into the mathematical cost function in the optimization algorithm used to calculate the conductivity and permittivity.

3.3. Results

3.3.1. Results Validation

For the methods validation, relative permittivity of the three Plexiglas samples were measured at 60Hz, 500Hz, 1KHz, 10KHz and 100KHz using the proposed technique. The average measured relative EP for the three Plexiglas samples at the mentioned frequency were found to be 3.45±0.11, 3.3±0.12, 3.25±0.09, 3±0.13, and 2.8±0.1, respectively. It is noteworthy to mention that these values are fairly close to the relative permittivity range of 3.5-2.7 which is provided by the manufactures at 50Hz-100 kHz [28].

3.3.2. Specimen Dielectric Measurement Results

Table 3.1 indicates the relative electrical permittivity and conductivity values of five xenograft breast cancer tumors and five samples of healthy surrounding tissue calculated using the proposed technique. These results in addition to electrical conductivity and relative electrical permittivity of breast adipose [3-5] are also shown in Figure 3.5 and Figure 3.6. Furthermore, comparison between the ratios of the mean conductivity and permittivity values of the malignant to normal tissues at 100Hz-1MHz is summarized in table 3.2. These results indicate that the average conductivity of the normal tissue samples measured over the range of frequencies of 100 Hz to 1 MHz, range from 0.00256 to 0.88275 S/m. While the average conductivity of the

xenograft breast tumor samples over the same frequency range varies between 0.009375 to 2.364 S/m. The average relative permittivity of the normal tissue specimens over this frequency range varies from 360361 to 44, while for the xenograft tumor specimens it varies from 4846300 to 453 over the same frequency range. These values clearly indicate that the relative permittivity and conductivity of the xenograft tumors are significantly higher than those of the healthy surrounding tissue. It is noteworthy that the difference between the relative permittivity values of the tumor and normal tissue samples is higher than the difference in their corresponding conductivity values. This indicates that electrical permittivity maybe a more powerful biomarker for breast malignancies detection compared to electrical conductivity. The standard deviation of the relative permittivity values pertaining to the xenograft tumor tissue samples at 100 Hz-1MHz are only 8.3% - 16.2%, while the standard deviation corresponding to the healthy tissue specimens are within 12% - 21.4%. The standard deviation of the conductivity values pertaining to the xenograft tumor samples at the same frequency range varies from 29% to 65% while the standard deviation of the conductance pertaining to the healthy surrounding tissues corresponding to the same frequency range are within 20% to 45%.

The standard deviation values include inter and intra specimen variability in addition to experimental errors. The reported standard deviation values indicate less inter and intra specimen variability of the electrical permittivity compared to electrical conductivity. This may consolidate the higher suitability of electrical permittivity as a biomarker for breast cancer diagnosis.

Histology images obtained from representative xenograft tissue samples are shown in Figure 3.7. The images demonstrate considerable differences in composition, nuclear density and micro-structures of cancerous and normal surrounding tissues. In contrast to the normal tissue, the tumor tissue consists of packed carcinoma cells with high nuclear density and low extra cellular space. The ultrasound b-mode images acquired from the tumor and surrounding tissues are shown in figure 3.8. The low and high-frequency ultrasound images demonstrate a lower echogenicity within the tumor area in comparison to the normal surrounding tissue. Such contrast in tissue echnogenicity is mainly due to substantial differences in micro-structures of the two tissue types as observed within the histology images.

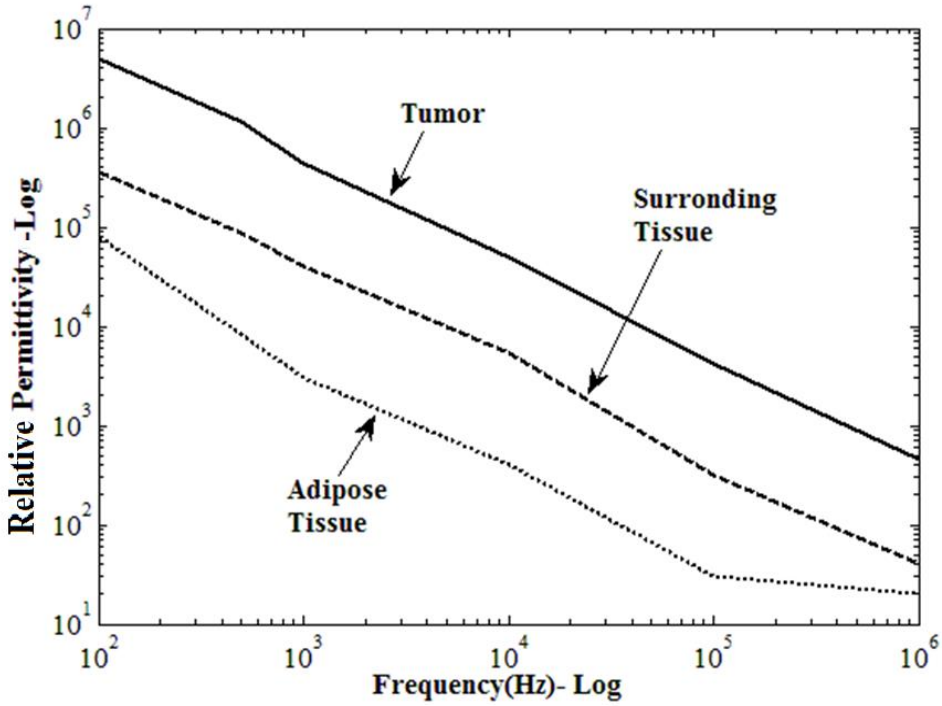

Figure 3.5. The average relative permittivity of the tumor and surrounding tissue samples at 100Hz-1MHz

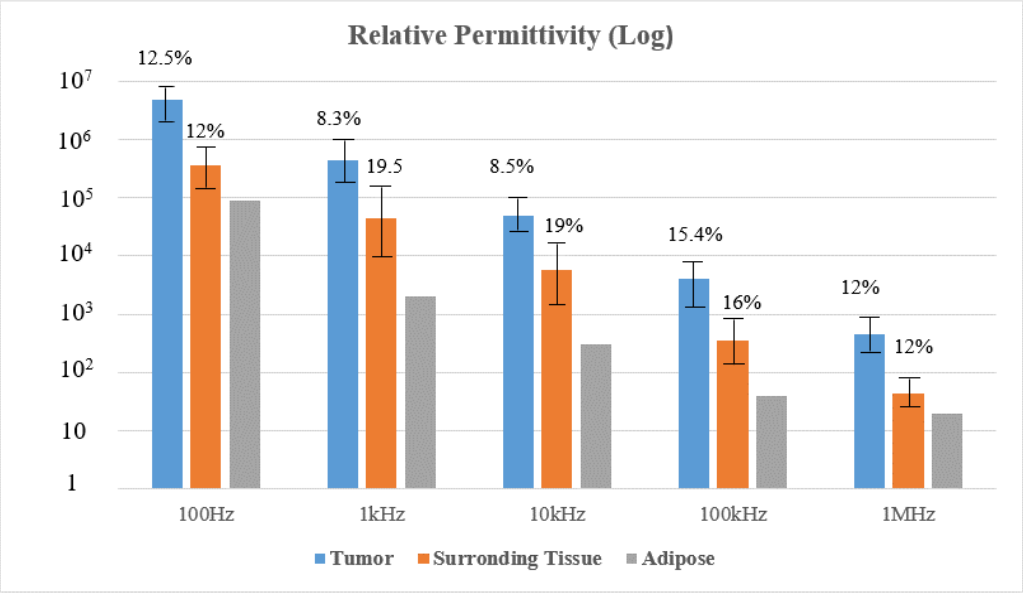

Figure 3.6. The mean and standard deviation of the tumors and surrounding tissues' relative permittivity at 100Hz-1MHz. The standard deviation bars are not to scale. The magnitude of each standard deviation is shown in percentage on each bar.

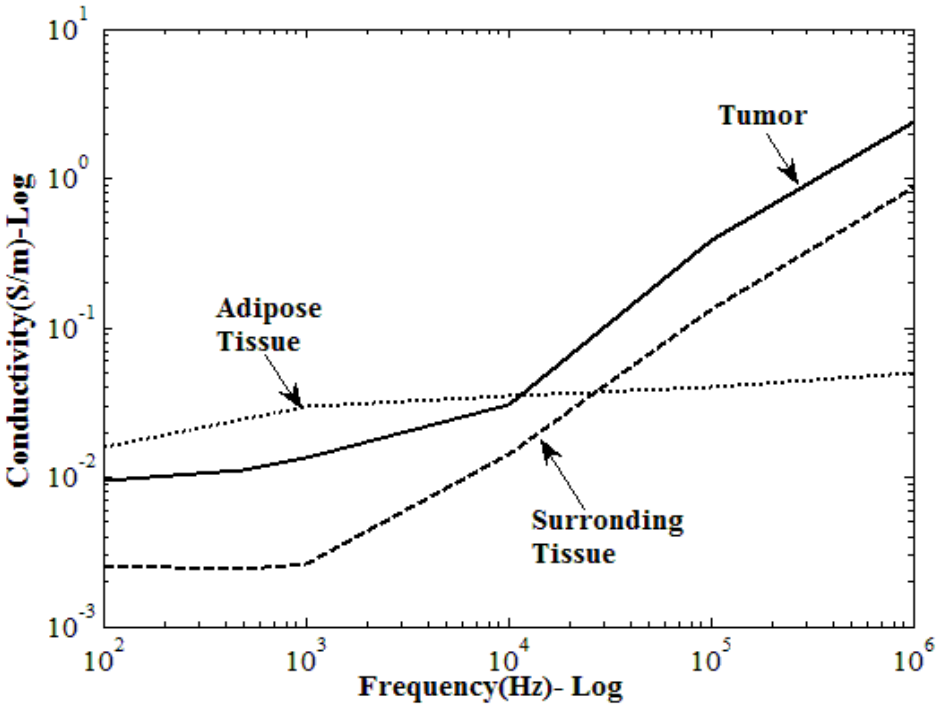

Figure 3.7. The average conductivity of the tumor and surrounding tissue samples at 100Hz-1MHz

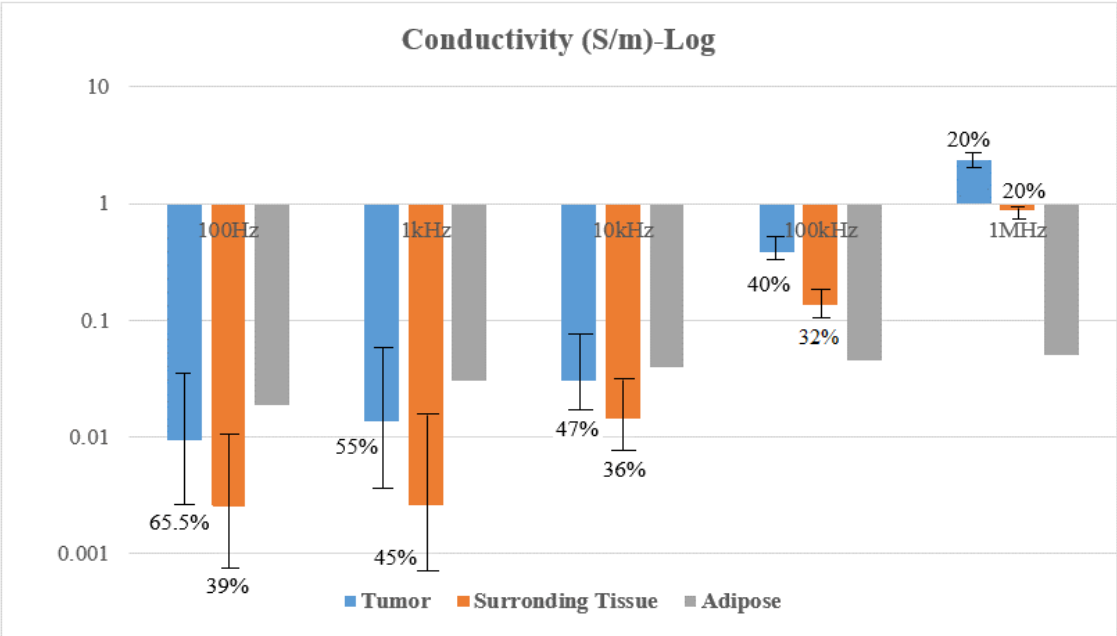

Figure 3.8 The mean and standard deviation of the tumors and surrounding tissues' conductivity at 100Hz-1MHz. The standard deviation bars are not to scale. The magnitude of each standard deviation is shown in percentage on each bar.

Table 3.1. Relative Electrical permittivity (ε_r) and electrical conductivity (σ) of five breast tumor samples and their normal surrounding tissues at 100Hz - 1MHz .

Tissue type/ Sample No.	ε_r @ 100Hz (Relative EP)	Mean ε_r ±STD @ 100Hz	σ @ 100Hz (S/m)	Mean σ ±STD @ 100Hz
Breast Tumor 1	4095555	4846300±607901	0.00497	0.009375±0.006164
Breast Tumor 2	4956390		0.00707	
Breast Tumor 3	5035382		0.01565	
Breast Tumor 4	4453730		0.01621	
Breast Tumor 5	5690443		0.00296	
Tissue type/ Sample No.	55% ε_r @ 500Hz	Mean ε_r ±STD @ 500Hz	σ @ 500Hz (S/m)	Mean σ ±STD @ 500Hz (S/m)
Breast Tumor 1	1012112	1160402±188056	0.01646	0.01109±0.00558
Breast Tumor 2	1112577		0.00775	
Breast Tumor 3	1151011		0.01557	
Breast Tumor 4	1482221		0.01248	
Breast Tumor 5	1044091		0.00312	
Tissue type/ Sample No.	ε_r @ 1KHz	Mean ε_r ±STD @ 1KHz	σ @ 1KHz (S/m)	Mean σ ±STD @ 1KHz (S/m)
Breast Tumor 1	445690	437278±36506	0.01854	0.01355±0.00741
Breast Tumor 2	414314		0.00818	
Breast Tumor 3	428107		0.02083	
Breast Tumor 4	495870		0.01678	
Breast Tumor 5	402412		0.00342	
Tissue type/ Sample No.	ε_r @ 10KHz	Mean ε_r ±STD @ 10KHz	σ @ 10KHz (S/m)	Mean σ ±STD @ 10KHz (S/m)
Breast Tumor 1	55862	49707±4243	0.05485	0.03055±0.01446
Breast Tumor 2	47775		0.01718	
Breast Tumor 3	52330		0.03074	
Breast Tumor 4	46481		0.02333	
Breast Tumor 5	46085		0.02664	
Tissue type/ Sample No.	ε_r @ 100KHz	Mean ε_r ±STD @ 100KHz	σ @ 100KHz (S/m)	Mean σ ±STD @ 100KHz (S/m)
Breast Tumor 1	3358		0.64416	0.38701±0.15704

Breast Tumor 2	3771	4139±639	0.23621	
Breast Tumor 3	4487		0.41070	
Breast Tumor 4	5011		0.34159	
Breast Tumor 5	4068		0.30240	
Tissue type/ Sample No.	ε_r @ 1MHz	Mean ε_r ±STD @ 1MHz	σ @ 1MHz (S/m)	Mean σ ±STD @ 1MHz (S/m)
Breast Tumor 1	483	453.7±58	2.5704	2.364±0.7033
Breast Tumor 2	389		1.2856	
Breast Tumor 3	442.8		2.6850	
Breast Tumor 4	537.2		2.1303	
Breast Tumor 5	416		3.1485	
Tissue type/ Sample No.	ε_r @ 100Hz	Mean ε_r ±STD @ 100Hz	σ @ 100Hz (S/m)	Mean σ ±STD @ 100Hz (S/m)
Normal Tissue 1	297037	360361.5±43537	0.00359	0.00256±0.001
Normal Tissue 2	373932		0.00165	
Normal Tissue 3	412200.8		0.00178	
Normal Tissue 4	340633		0.00209	
Normal Tissue 5	378004		0.00370	
Tissue type/ Sample No.	ε_r @ 500Hz	Mean ε_r ±STD @ 500Hz	σ @ 500Hz (S/m)	Mean σ ±STD @ 500Hz (S/m)
Normal Tissue 1	109753	96471±20656.6	0.00432	0.00246±0.00109
Normal Tissue 2	125641.7		0.00210	
Normal Tissue 3	76152		0.00185	
Normal Tissue 4	82116		0.01248	
Normal Tissue 5	88691		0.002415	
Tissue type/ Sample No.	ε_r @ 1KHz	Mean ε_r ±STD @ 1KHz	σ @ 1KHz (S/m)	Mean σ ±STD @ 1KHz (S/m)
Normal Tissue 1	56007.4	45269.7±8820.5	0.00472	0.00263±0.00120
Normal Tissue 2	44362.8		0.00217	
Normal Tissue 3	35728		0.00177	
Normal Tissue 4	52336		0.00195	
Normal Tissue 5	37914		0.00256	
Tissue type/ Sample No.	ε_r @ 10KHz	Mean ε_r ±STD @ 10KHz	σ @ 10KHz (S/m)	Mean σ ±STD @ 10KHz (S/m)
Normal Tissue 1	5283.9	5871.5±1131	0.01698	0.01434±0.00517
Normal Tissue 2	5108.6		0.00786	
Normal Tissue 3	4927		0.01016	
Normal Tissue 4	7595.3		0.02036	
Normal Tissue 5	6442.7		0.01634	
Tissue type/ Sample No.	ε_r @ 100KHz	Mean ε_r ±STD @ 100KHz	σ @ 100KHz (S/m)	Mean σ ±STD @ 100KHz (S/m)
Normal Tissue 1	383.1		0.13080	
Normal Tissue 2	312.4		0.11977	

Normal Tissue 3	276	355.5±58	0.08249	0.13407±0.04314
Normal Tissue 4	395.6		0.20166	
Normal Tissue 5	410.3		0.13563	
Tissue type/ Sample No.	ε_r @ 1MHz	Mean ε_r ±STD @ 1MHz	σ @ 1MHz (S/m)	Mean σ ±STD @ 1MHz (S/m)
Normal Tissue 1	37	44±5.3	1	0.88275±0.18319
Normal Tissue 2	51.4		0.78716	
Normal Tissue 3	41.5		0.71957	
Normal Tissue 4	44		1.13016	
Normal Tissue 5	46		0.75	

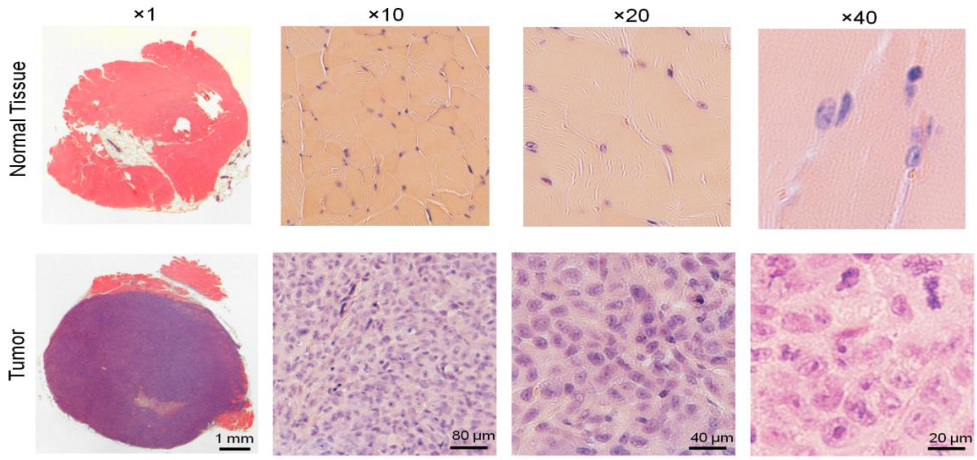

Figure 3.9. Light microscopy images of Hematoxylin and eosin (H&E) stained tissue sections at different magnifications obtained from a representative xenograft sample. The top row (from left to right) shows the normal surrounding tissue at 1-40x magnifications. The bottom row shows the breast tumor tissue containing invasive ductal carcinoma at 1-40x magnifications.

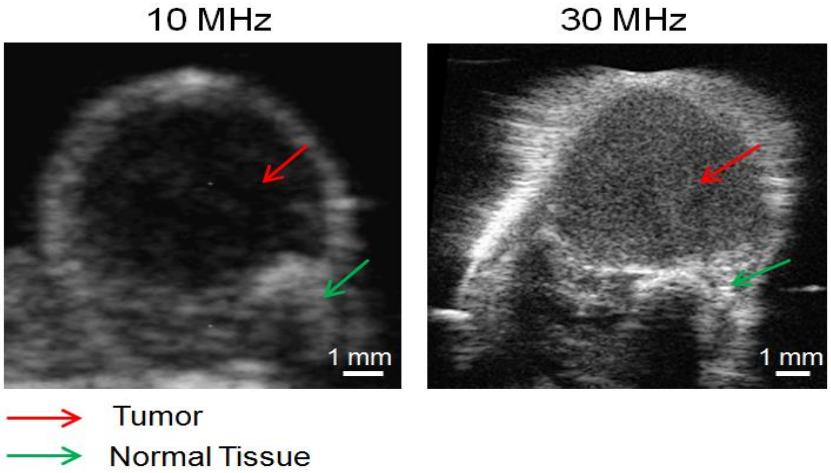

Figure 3.10. Low and high-frequency ultrasound images of a representative breast tumor xenograft and its normal surrounding tissue obtained before euthanizing the animal.

3.4. Discussion and Conclusions

The study presented in this paper involves using a recently developed technique for measuring the dielectric properties of *ex vivo* tissue specimens of a mouse xenograft model at low frequencies. The technique applies a relatively simple hardware configuration consisting of signal generator, oscilloscope, buffer, plexiglas holder and two electrodes. The tissue sample being tested is placed between the two electrodes such that the electrodes and tissue sample assembly form a capacitive-resistive load with the sample acting as the dielectric. The setup is capable of measuring the impedance of tissue specimens with reasonably high accuracy, providing dielectric data which carries the tissue EP and EC data. The measurement method follows an inverse finite element algorithm framework which inputs the setup's configuration data, known electrical properties of the electrodes and excitation voltage in order to output the tissue specimen's dielectric properties. Conventional dielectric measurement techniques were previously developed based on admittance data analysis models which assume semi-infinite geometry model [5,9,23]. The semi-infinite geometry model is reasonably accurate with relatively large tissue specimens excited with high frequencies. As such these techniques provide reasonably good measurement accuracy to measure high frequency dielectric properties of large tissue specimens. To measure the low frequency dielectric properties of small tissue specimens, the technique described in this study models the specimen's geometry, boundary conditions, the data pertaining to the measurement's setup and the excitation frequency highly accurately through finite element simulation. Therefore, in principle, this technique offers a more rigorous method of measuring dielectric characteristics of tissues under a wide range of frequencies and specimen sizes. The latter is particularly important for measuring dielectric properties of human tissues as tissue specimens routinely acquired from surgeries are usually small. To assess the accuracy of the proposed technique, the method was applied to measure the relative permittivity of plexiglas specimens at a frequency range of 60 Hz – 100 KHz, this measurement led to an average relative permittivity value of 3.45-2.8 with maximum error of 3.7% in comparison with the permittivity range provided by the manufacturer. Such low error is anticipated given that the

method is founded on a solid theoretical background. The technique was used in a preclinical study on animal tumor models to measure and compare the dielectric properties of several normal and cancerous tissue specimens *ex vivo*. The obtained measurement result from this study which is summarised in table 3.2 indicates that the average conductivity of breast tumors are 2.1-5.1 times higher than the average conductivity of surrounding healthy tissues at 100 Hz-1 MHz frequencies, while the average permittivity of the breast tumors are 8.4-13.4 times higher than the average permittivity of the surrounding normal tissues and about 80 times larger than permittivity values of adipose tissue reported at the same frequency range [3-5]. This substantially higher ratio lends more credibility to the effectiveness of electrical permittivity imaging at low frequencies for cancer diagnosis especially with older women whose breasts mainly consist of adipose tissue. The higher ratio of permittivity versus conductivity of the tumors to healthy tissue specimens (8.4-13.4 vs. 2.1-5.1) shows that electrical permittivity may be a better parameter than electrical conductivity for distinguishing between healthy and malignant breast tissues at low frequencies. It is noteworthy that the tumor-to-background EP ratios measured in this study are significantly higher than ratios obtained for some other tissue physical properties (e.g. light absorption). For instance in optical imaging, near infrared (NIR) absorption and hemoglobin concentration levels in tumors are only 2-4 higher in comparison with healthy breast tissues [29].

The measured dielectric properties of the ten specimens also indicated that the standard deviation of the permittivity values are reasonably low (8%-21%) at all frequencies. This implies that the technique used for measuring tissue electrical permittivity is reasonably accurate while inter and intra specimen variability is relatively low. The standard deviation of the conductance values are higher (20%-65%) at the 100 Hz-1 MHz frequency range. Based on what Epstein et al. findings [30], this higher standard deviation can be justified by the higher anisotropy in tissues conductance in comparison with tissues permittivity at frequencies below 1MHz.

Table 3.2. Comparison between ratios of the mean conductivity and relative permittivity of the tumor- background tissue specimens at 100 Hz-1 MHz .

Frequency (KHz)	Mean Tumor EP(n=5) to Mean Background Tissue EP(n=5) Ratio	Mean Tumor EC(n=5) to Mean Background Tissue EC(n=5) Ratio
0.1	13.45:1	3.7:1
0.5	12:1	4.5:1
1	9.7:1	5.1:1
10	8.5:1	2.1:1
100	11.6:1	2.9:1
1000	10.3:1	2.7:1

References

[1] http://www.wcrf.org, Nov. 3, 2016

[2] Coleman MP, Quaresma M, Berrino F, Lutz JM, De Angelis R, Capocaccia R, Baili P, Rachet B, Gatta G, Hakulinen T, Micheli A, Sant M, Weir HK, Elwood JM, Tsukuma H, Koifman S, E Silva GA, Francisci S, Santaquilani M, Verdecchia A, Storm HH, Young JL; CONCORD Working Group, Cancer survival in five continents: a worldwide population-based study (CONCORD), Lancet Oncol. 2008 Aug; 9(8):730-56. doi: 10.1016/S1470-2045(08)70179-7. Epub 2008 Jul 17

[3] The dielectric properties of biological tissues: I. Literature survey, C Gabriel, S Gabriely and E Corthout, Phys. Med. Biol. 41 (1996) 2231–2249. Printed in the UK

[4] S Gabriel, R W Lau and C Gabriel, The dielectric properties of biological tissues: II. Measurements in the frequency range 10 Hz to 20 GHz, Phys. Med. Biol. 41 (1996) 2251–2269. Printed in the UK

[5] S Gabriel, R W Lau and C Gabriel, The dielectric properties of biological tissues: III. Parametric models for the dielectric spectrum of tissues, Phys. Med. Biol. 41 (1996) 2271–2293. Printed in the UK

[6] Ryan J. Halter, Alan Schned, John Heaney, Alex Hartov, Keith D. Paulsen; Electrical Impedance Spectroscopy of Benign and Malignant Prostatic Tissues, DOI 10.1016/j.juro.2007.11.043

[7] Ryan J. Halter, Alex Hartov, Keith D. Paulsen, A Broadband High-Frequency Electrical Impedance Tomography System for Breast Imaging, IEEE TRANSACTIONS ON BIOMEDICAL ENGINEERING, VOL. 55, NO. 2, FEBRUARY 2008

[8] Ryan J. Halter, Alan R. Schned, John A. Heaney, Alex Hartov; Passive Bioelectrical Properties for Assessing High- and Low-Grade Prostate Adenocarcinoma, The Prostate 71:1759-1767 (2011)

[9] William T. Joines, Yang Zhang, Chenxing Li, Randy L. Jirtle; The measured electrical properties of normal and malignant human tissues from 50 to 900 MHz, Med. Phys. 21, 547 (1994)

[10] William T. Joines, Randy L. Jirtle, Marc D. Rafal, Daniel J. Schaefer; Microwave power absorption differences between normal and malignant tissue, International Journal of Radiation Oncology Biology Physics, Volume 6, Issue 6, June 1980, Pages 681–687

[11] Thakur, S. B., S. B. Brennan, N. M. Ishill, E. A. Morris, L. Liberman, D. D. Dershaw, L. Bartella, J. A. Koutcher, and W. Huang, Diagnostic usefulness of water-to-fat ratio and choline concentration in malignant and benign breast lesions and normal breast parenchyma: an in vivo 1H MRS study. J. Magn. Res. Imaging 33:855–863, 2011

[12] Gerard H. Markxa, Christopher L. Daveyb, The dielectric properties of biological cells at radiofrequencies: Applications in biotechnology, Enzyme and Microbial Technology 25 (1999) 161–171

[13] H. Fricke and S. Morse, “The electric capacity of tumors of the breast,” J. Cancer Res., vol. 16, pp. 310-376, 1926

[14] T. S. England and N. A. Sharples, “Dielectric properties of the human body in the microwave region of the spectrum,” Nature, vol. 163, pp. 487-488, 1949.

[15] T. S. England, “Dielectric properties of the human body for wave lengths in the 1-10 cm range,” Nature, vol. 166, pp. 480-481, 1950

[16] J. Surowiec, S.S. Stuchly, J.B. Barr, and A. Swarup, “Dielectric properties of breast carcinoma and the surrounding tissues”, IEEE Trans. on Biomed. Engr., vol. 35, pp. 257–63, April 1988

[17] Ann P O’Rourke, Mariya Lazebnik, John M Bertram, Mark C Converse, Susan C Hagness, John G Webster, David M Mahvi; Dielectric properties of human normal, malignant and cirrhotic liver tissue: in vivo and ex vivo measurements from 0.5 to 20 GHz using a precision open-ended coaxial probe; Phys. Med. Biol. 52 (2007) 4707–4719 doi:10.1088/0031-9155/52/15/022

[18] R Clarke, Human breast cancer cell line xenografts as models of breast cancer—the immunobiologies of recipient mice and the characteristics of several tumorigenic cell lines, Breast cancer research and treatment, 1996 – Springer

[19] Shirakawa K, Kobayashi H, Sobajima J, Hashimoto D, Shimizu A, Wakasugi H; Inflammatory breast cancer: vasculogenic mimicry and its hemodynamics of an inflammatory breast cancer xenograft model, Breast Cancer Res. 5(3): 136-139, 2003

[20] Depreeuw J, Hermans E, Schrauwen S, Annibali D, Coenegrachts L, Thomas D, Luyckx M, Gutierrez-Roelens I, Debruyne D, Konings K1, Moerman P, Vergote I, Lambrechts D, Amant F; Characterization of patient-derived tumor xenograft models of endometrial cancer for preclinical evaluation of targeted therapies, 139(1): 118–126, 2015

[21] Done-Sik Yoo “The dielectric properties of cancerous tissues in a nude mouse xenograft model” Bioelectromagnetics Volume 25, Issue 7, pages 492–497, October 2004

[22] Jeiwon Cho, Jeonghoon Yoon, Sungjoon Cho, Kihyun Kwon, Sungkyu Lim, Daeduk Kim, Eun Sook Lee, Chul Hwan Kim, Jin Wook Choi, Changyul Cheon, Youngwoo Kwon; In-vivo measurements of the dielectric properties of breast carcinoma xenografted on nude mice; Int. J. Cancer: 119, 593–598 (2006)

[23] James Baker Jarvis, Michael D. Janezic, Paul D. Domich, Richard G. Geyer; Analysis of an Open-Ended Coaxial Probe with Lift-off for Nondestructive Testing, IEEE TRANSACTIONS ON INSTRUMENTATION AND MEASUREMENT, VOL. 43, NO. 5, OCTOBER 1994

[24] Allan R. Hambley, Electrical Engineering Principle and applications

[25] Roberto Cardu, Philip H W Leong, Craig T Jin, Alistair McEwan, Electrode contact impedance sensitivity to variations in geometry, Physiol. Meas. 33 (2012) 817–830 doi:10.1088/0967-3334/33/5/817

[26] Comsol 4.3, AC/DC Module User's Guide, 2012

[27] W.H. Press, S.A. Teukolsky, W.T. Vetterling, B.P. Flannery, 1992. Numerical Recipes in Fortran 77. The Art of Scientific Computing. Cambridge University Press, Cambridge

[28] Physical Properties of 0.236" Plexiglas sheet (ACP Noxtat base substrate material), ACP Noxtat, Santa Ana, CA, USA

[29] Huabei Jiang, Nicusor V. Iftimia, Yong Xu, Julia A. Eggert, Laurie L. Fajardo, Karen L. Klove; Near-Infrared Optical Imaging of the Breast with Model-based Reconstruction; Acad Radiol 2002; 9:186–194

[30] B.R. Epstein, K.R Foster; Anisotropy in the dielectric properties of skeletal muscle; Med. & Biol. Eng. & Comput. 1983, 21, 51-55

Chapter 4

Toward Medical Electrical Impedance Mammography Using Low Frequency Excitation

The material presented in this chapter is currently pending submission to the peer-reviewed journal papers due to the US Patent W-15-036 filed in August, 2015 by the authors.

Authors' Contributions Statement: *The main idea of this chapter is conceived by the principle author of this study, Seyyed M. Hesabgar. The research, experiments, and measurements presented in this chapter have been conducted by Seyyed M. Hesabgar and guided by the research supervisor, Dr. Abbas Samani.*

4.1. Introduction

Breast cancer is the most common type of cancer among women, leading to more than 40,000 deaths in the US each year. Approximately 12.3% of women (one in every eight women) are diagnosed with breast cancer at some point during their lifetime, and current research shows that the prevalence of breast cancer will continue to increase throughout the world [1]. Breast screening offers the opportunity for early detection of breast cancer, leading to higher chances of survival, less extensive treatments and better overall outcomes [2]. The most commonly used imaging modality for breast cancer screening is x-ray mammography, however the use of ionizing radiation limits the frequency of employing this modality for breast cancer detection. Furthermore, x-ray mammography has been shown to be less effective for breast cancer detection among young women who have dense breasts. In this regard, studies have shown that among this group of women, corresponding to each 10 acquired mammograms, as many as one in two women will have at least one false positive [3-5]. As an alternative to x-ray mammography, magnetic resonance imaging (MRI) has proven to be a powerful tool in monitoring high-risk women, however its high cost and variable specificity limits its usage for breast cancer screening [3,5]. Ultrasound imaging is commonly used as a second-line diagnostic

tool to differentiate masses detected by x-ray mammography, however, its low sensitivity and specificity makes it unsuitable as a front-line screening system [3,5].

Over the past three decades, electrical impedance tomography (EIT) and electrical impedance mammography (EIM) have emerged as novel biomedical imaging modalities with the aim of addressing the shortcomings of other breast imaging modalities [6-8]. EIT and EIM modalities use low energy electric field to probe and characterize electrical impedance of biological tissues. The use of non-ionizing electric field as well as the simplicity and low cost of these imaging modalities make them ideal for breast cancer screening. EIT and EIM produce images that display the distribution of tissue electrical impedance (electrical conductivity and electrical permittivity). Studies aimed at characterizing the electrical properties of normal and pathological tissue have shown that electrical conductivity and electrical permittivity of breast malignancies are significantly higher than those of benign and normal breast tissues [11-13]. Some of these studies have concluded up to 20-40-fold higher values for both parameters in breast tumors compared to normal breast tissue [12]. This elevation in the electrical properties of malignant tissues stems from the higher intra and extra cellular water content, higher cell density and changes in the membrane orientation of the malignant cells [14-17]. EIT and EIM methods take advantage of this elevation for breast tumor detection. As such, over the past three decades many researchers such as Halter et al. [18], Ye et al [19, 20], Zhang et al. [21], Choi et al. [22] and Cherepenin et al. [23] have proposed various EIT and EIM systems for the detection of breast lesions.

While EIT and EIM have been developed and significantly improved over the past three decades, they still suffer from shortcomings that have limited their clinical utility for breast cancer imaging. The first major issue in this regard is that tissue impedance is usually approximated by tissue conductance. Consequently, most proposed EIT and EIM systems only generate one type of image which displays tissue conductance distribution or projection. Based on recent literature, while the range of conductance variations of biological tissues is relatively small, corresponding range of tissue permittivity variation is broad. For instance, Gabriel et al. [24, 25] have shown that the range of electrical conductivity of biological tissues at 10 Hz-20 GHz is within 0.01-40 S/m while their relative permittivity is in the $1\text{-}10^8$ range. This implies that imaging tissue conductance at 10 Hz-20 GHz frequency may not be suitable for generating high contrast images, whereas imaging tissue permittivity may potentially produce high contrast images.

Furthermore, while tissue impedance phase angle is known to carry important biological information [34,35], its utility in the context of imaging has not been explored significantly. The second issue in EIT and EIM pertains to data acquisition where a large number of impedance measurements are usually required to produce an image. Although conceptually simple, in practice the number of electrodes that can be placed on the patient`s body to perform the measurements is limited, rendering the data acquisition step difficult to implement [8,26]. Moreover, image reconstruction in EIT is a challenging inverse problem, as it is both nonlinear and ill-posed [26]. As such, it requires iterative and time-consuming algorithms necessary for image reconstruction. In contrast to EIT, in EIM the image reconstruction step is significantly less involved. Among the studies that have investigated the possibility of using EIM for breast cancer detection, Assenheimer et al. [33] demonstrated that current EIM technologies such as TransScan 2000 (Siemens Medical, Germany, and TransScan, Ramsey, NJ, USA), are only capable of detecting low impedance inclusions located close to the breast surface. The primary goal of this research is to introduce a novel EIM technique which may potentially mitigate the aforementioned issues encountered in this technique. For this purpose, we present an electrical impedance imaging system consisting of a parallel plate sensor, where its utility for breast mammography is explored. This investigation involves *in silico* and tissue mimicking phantom studies conducted to present a proof of concept for the proposed technique and to demonstrate its potential application for breast screening.

4.2. Methods

4.2.1. Governing Equations

The electromagnetic field generated by applying current density to a body surface is governed by Maxwell's equations. For a nonmagnetic material such as biological tissues, the general form of Maxwell's equations in the time domain with the inclusion of displacement current and continuity equation is as follows [27]:

$$\nabla \cdot \mathbf{J}(r, t) = -\frac{\partial \rho(r, t)}{\partial t} \qquad (4.1)$$

$$\nabla \cdot \mathbf{D}(r, t) = \rho(r, t) \qquad (4.2)$$

$$\nabla \times \mathbf{H}(r, t) = \mathbf{J}(r, t) + \frac{\partial \mathbf{D}(r,t)}{\partial t} = \sigma E(r, t) + \mathbf{J_e}(r, t) + \frac{\partial \mathbf{D}(r,t)}{\partial t} \quad (4.3)$$

$$\nabla \cdot \mathbf{B}(r, t) = 0 \quad (4.4)$$

$$\nabla \times \mathbf{E}(r, t) = -\frac{\partial \mathbf{B}(r,t)}{\partial t} \quad (4.5)$$

where ρ(r,t) is the electric charge density, J is the electric current density, E is the electric field, D = εE is the electric displacement current, ε is the electric permittivity, B is the magnetic field, H = B/μ is the magnetic intensity and μ is the magnetic permeability which is considered to be the same as the permeability of vacuum for biological tissues. In this study, we assume that the external magnetic field is negligible (B = 0). We also assume that impedance measurement is performed at low frequencies (1MHz or lower) where the frequency of the voltage source is low enough for the EM propagation delay to be neglected [28]. Using the phasor format of equations 1 to 5 and dropping the time harmonic, leads to the following equations in the frequency domain. This was performed to facilitate the equations' computational solution consistent with the COMSOL Multiphysics software package (COMSOL, Inc., MA, USA) used in this investigation.

$$\nabla \cdot \mathbf{J}(r, \omega) = \mathbf{Q}_j(r, \omega) \quad (4.6)$$

$$\mathbf{J}(r, \omega) = \boldsymbol{\sigma}\mathbf{E}(r, \omega) + j\omega\mathbf{D}(r, \omega) + Je(r, \omega) \quad (4.7)$$

$$\mathbf{E}(r, \omega) = -\nabla\mathbf{V}(r, \omega) \quad (4.8)$$

where Q_j represents current source, σ is tissue electrical conductivity, ω is the natural frequency, J_e is an externally induced current density and V is the electric potential [29]. We use COMSOL which uses the finite element method (FEM) to solve equations 4.6-4.8 and obtain the impedance amplitude and phase angle in the breast models involved in this investigation.

4.2.2. Overview of the Proposed Electrical Impedance Mammography

Similar to x-ray mammography where the breast is placed in a parallel-plate compression unit and projections of x-ray are measured and converted into mammograms, in the proposed EIM technique, the breast is gently compressed between the two parallel plates of an impedance sensor. While the breast is gently compressed, the electrical impedance its tissue is measured as projection data before they are converted into a mammogram. Depending on the excitation frequency in the proposed technique, different types of image reconstruction methods such as image impedance, resistance, capacitance and phase angle may be employed to generate respective images. While imaging impedance and resistance are feasible at all excitation frequencies, for the capacitance and phase angle imaging, choosing the right excitation frequency is critical. It is assumed throughout this study that the dielectric values of the breast malignancies are significantly higher than the dielectric values of the normal breast tissues.

4.2.3. Electrical Model of Tissues at Low Frequencies

In order to study the electrical behaviour of a biological tissue, a proper electrical model of it is required. A lumped electric model (equivalent circuit) of a tissue part of the breast located between two electrodes of the two parallel plates at low frequencies is shown in Figure 4.1. It consists of a parallel resistor and capacitor.

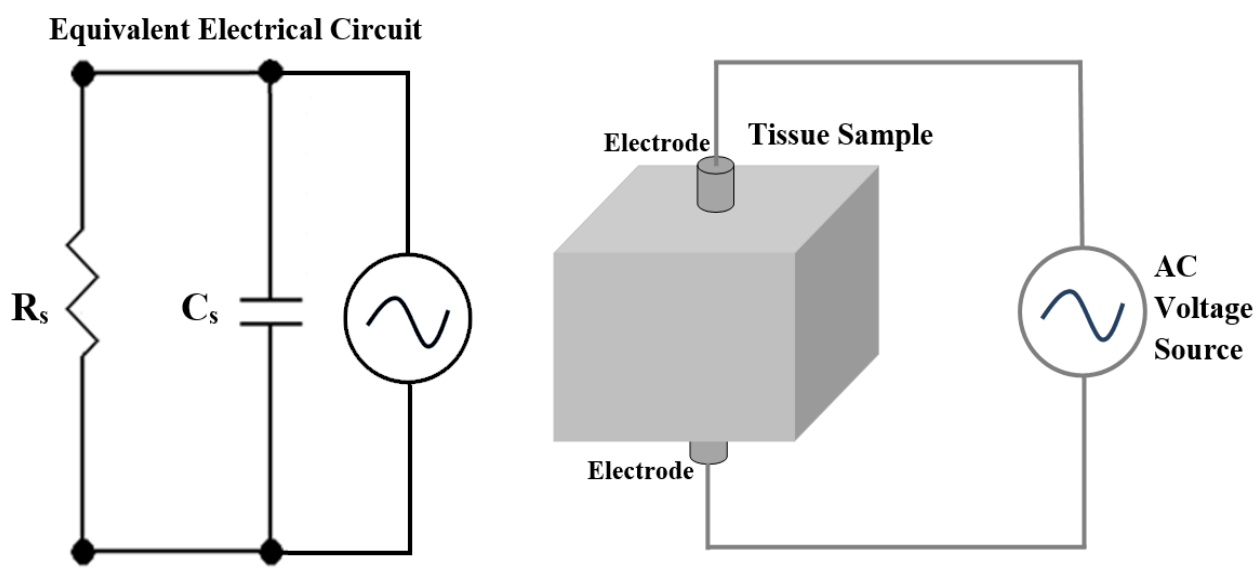

Figure 4.1. Schematic of a breast tissue sample held between two cylindrical-shaped electrodes (right) and its equivalent electrical circuit at low frequencies (left).

It is noteworthy that the electrical model of biological tissues, which is used extensively in the literature [32], has an additional series resistor with capacitance C_s. However, at low frequencies, the value of this resistor, which represents the resistance of intracellular fluids, becomes negligible [32]. The relationship between electrical impedance, resistance, capacitance, and phase angle of a biological tissue sample derived from its equivalent circuit, is:

$$Z_s \angle\theta_s = [(R_s/\omega C_s) / (R_s^2 + (1/\omega C_s)^2)^{1/2}] \angle -90^o + \mathrm{Arctg}\,(1/R_s C_s \omega) \qquad (4.9)$$

where Z_s and θ_s are the measured amplitude and phase angle of the tissue's electrical impedance, ω is the natural frequency of the excitation signal, and R_s and C_s are the tissue's electrical resistance and capacitance, respectively.

4.2.4. Electrical Property Image Reconstruction Types

In order to examine how the impedance components of a typical biological tissue (e.g. adipose) changes with frequency, we conducted a computational simulation involving an adipose tissue specimen. Here an electrical model of a 50mm×50mm×50mm block-shaped adipose tissue specimen was constructed, and its electrical impedance ($Z_s \angle\theta_s$) was measured at frequencies of 10 Hz to 1 MHz via simulation using COMSOL. The electrical conductivity and permittivity of the tissue specimen at these frequencies, which were input to reconstruct the model, were obtained from the literature [24,25]. The measurement was assumed to be conducted using two different configurations, leading to two corresponding finite element (FE) models. In one configuration the specimen was assumed to be placed between two cylindrical brass electrodes with a radius of 1.5 mm and height of 2mm. In the other configuration, the specimen was assumed to be held between the parallel plates of the proposed EIM imaging sensor. Each of these models consisted of ~2.2 tetrahedral finite elements.

Using COMSOL solver in conjunction with equation 4.9, the capacitance and resistance data of the adipose tissue specimen at the 10 Hz-1MHz frequency range were obtained for each

configuration. These data, which are illustrated in Figure 4.2, show that at frequencies higher than 1kHz, the adipose tissue capacitance component diminishes, hence the tissue's impedance becomes predominantly resistive at such frequencies. This implies that the reconstruction of capacitance, permittivity and phase angle images that require the capacitive component of the tissue's impedance are not feasible at excitation frequencies higher than 1 kHz. Based on these observations, the following three types of image reconstruction can be derived.

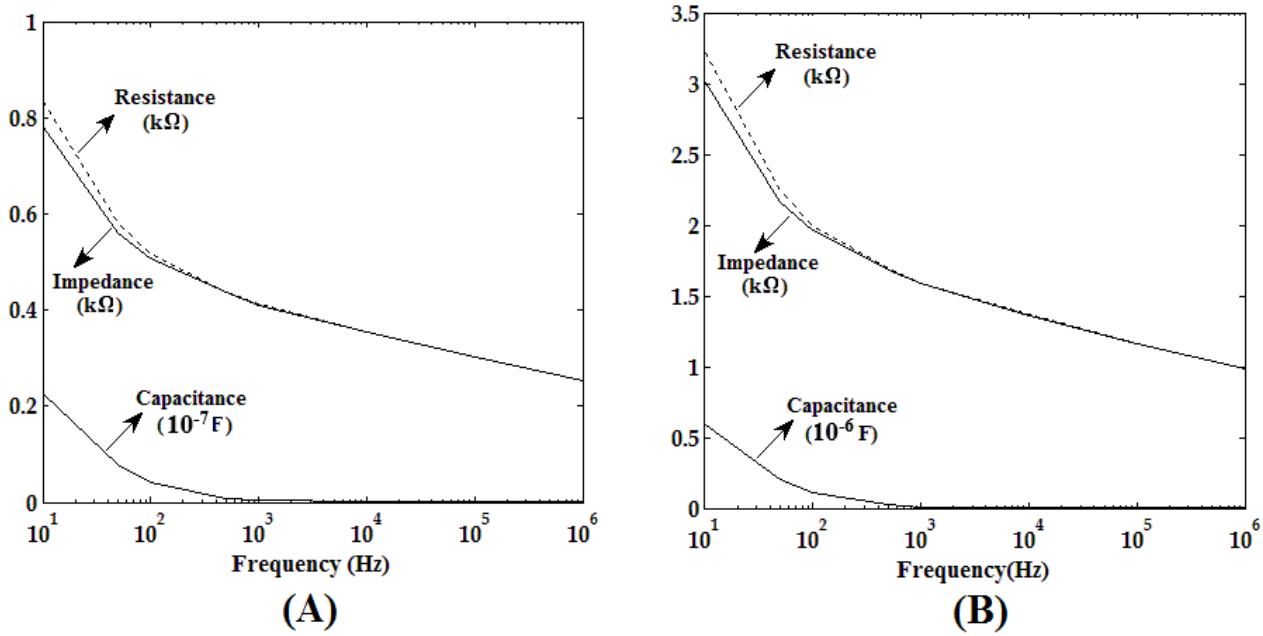

Figure 4.2. Electrical resistance, impedance and capacitance of the adipose tissue model at 10Hz-1MHz while placed between: two electrodes (A) and two parallel plates of the proposed scanner (B).

4.2.4.1. Electrical Resistivity and Conductivity Image Reconstructions in EIT and EIM

Electrical conductivity image reconstruction is the easiest and most common type of electrical impedance image reconstruction. This method has been used in the majority of EIT (electrical

impedance tomography) applications in the past three decades. The following equation shows the fundamental relationship between tissue electrical resistivity and its conductivity [30],

$$R = \frac{V}{I} = \frac{\int E.\ dl}{\oint \sigma E.\ ds} \qquad (4.10)$$

where R is the tissue electrical resistance, V is the potential difference between the two electrodes where the voltage is being measured, I is the electric current, E is the electric field and σ is the tissue electrical conductivity. In the context of breast imaging, electrical resistance and electrical conductivity image reconstruction may be performed in the whole frequency range of 10Hz-1MHz, as according to Figure 4.2 the measured resistance at this frequency range is appreciably high. As such, in the majority of EIT image reconstruction methods which mainly use frequencies higher than 1kHz, the measured amplitude of tissue's impedance is simply approximated by its electrical resistance. However, the major problem with conductivity image reconstruction stems from the complex relationship between R and σ and its high dependence on the electric field. Consequently, this type of image reconstruction leads to an ill-posed problem, which requires iterative and non-linear image reconstruction algorithms. Furthermore, previous studies have shown that the variation range of conductivities for biological tissues at 10Hz-20GHz is limited [24,25]. This implies that conductivity and resistance imaging of biological tissues may not produce images with high contrast.

The following equation, which is derived from the lumped electrical model of the tissue (parallel capacitor and resistor in Figure 4.1), shows the relationship between the tissue resistance (R_s), their electrical impedance (Z_s) and phase angle (θ_s).

$$R_s = \frac{Z_s\ \mathrm{tg}(90+\theta_s)}{\sqrt{(1+\mathrm{tg}^2(90+\theta_s)}} \qquad (4.11)$$

In EIM, resistance image reconstruction involves obtaining resistance projection data for each point on the breast surface plane, and converting this data into 2D mammograms. As such, in this study we measured the breast tissue's impedance projections on the breast surface plane using the proposed impedance sensor. Then by using Equation (4.11), the resistance projection data of the breast tissue was calculated and converted into 2D resistance mammograms. As solving

Equation 10 for σ is not feasible, to obtain an estimate of the breast tissue's conductivity projection on the breast surface plane, we may assume uniform electric field leading to the inverted resistance image can be used.

4.2.4.2. Electrical Permittivity and Capacitance Image Reconstructions

Electrical permittivity is an intrinsic property of materials, which may be obtained via the material's electrical capacitance. For measuring tissue electrical capacitance, the amplitude and phase angle of the tissue's impedance must be measured reliably. The following equation shows the relationship between the tissue capacitance (C_s), their electrical impedance (Z_s) and phase angle (θ_s) based on the lumped electrical model shown in Figure 4.1.

$$C_s = \frac{1}{Z_s\,\omega\sqrt{(1+\mathrm{tg}^2(90+\theta_s)}} \qquad (4.12)$$

According to Figure 4.2, for a breast adipose tissue specimen placed between two electrodes, measuring the capacitance (C_s) and phase angle (θ_s) at frequencies higher than 1kHz may not be feasible, as the tissue capacitance becomes too small to be reliably measured. As such, for breast imaging, capacitance, permittivity and phase angle image reconstructions cannot be performed at high frequencies. However, at lower frequencies (e.g. 1 KHz or lower) where the electrical capacitance is sufficiently large, a reliable measurement of C_s is feasible.

Measurement of tissue electrical permittivity (ε) can be achieved by measuring its electrical capacitance (C_s) as direct measurement of permittivity is not feasible. The following equation shows the fundamental relationship between electrical capacitance (C) and electrical permittivity (ε) [30]:

$$C = \frac{Q}{V} = \frac{\oint \varepsilon E.\ ds}{\int E.\ dl} \qquad (4.13)$$

where Q represents the electric charge, V is the potential difference between the two electrodes where the measurement is performed, E is the electric field and ε is the tissue electrical permittivity. This equation shows that the relationship between C and ε is complex and highly dependent on the electric field. As such, tissue permittivity image reconstruction also leads to ill-posed problems that require iterative and non-linear inverse problem solution algorithms. However, as the variation range of permittivity of biological tissues is very broad in comparison

with that of conductivity [24, 25], permittivity and capacitance imaging is expected to produce images with higher contrast; hence they are preferable over resistance and conductivity imaging.

In EIM, capacitance image reconstruction involves obtaining capacitance projection data for each point on the breast surface plane followed by converting the data into 2D capacitance mammograms. In this study we measured the capacitance projections of the breast models on their surface plane using the proposed impedance sensor. Using Equation (4.12), the capacitance projection data of the breast tissue was calculated from the impedance data before they were converted into 2D capacitance mammograms. As solving Equation 13 for ε is not feasible, to obtain an estimate of the breast tissue's permittivity projection on the breast surface plane, the capacitance image can be used as capacitance and permittivity are approximately proportional.

4.2.4.3. Phase Angle Image Reconstruction

Impedance phase angle of a tissue (θ_s) may be obtained from Equation (9), leading to the following equation:

$$\theta_s = -90^o + \text{Arctg}\,(1/R_s C_s \omega) \qquad (4.14)$$

Using the discrete form of Equations (4.10) and (4.13) leads to:

$$\frac{1}{R_S C_S\,\omega} = \frac{\sum_{i=1}^{m} \sigma_i\, E_i\,.\,\Delta S_i}{\omega \sum_{i=1}^{m} E_i\,.\,\Delta L_i} \times \frac{\sum_{i=1}^{m} E_i\,.\,\Delta L_i}{\sum_{i=1}^{m} \varepsilon_i\, E_i\,.\,\Delta S_i} \qquad (4.15)$$

Assuming equal ΔS_i and ΔL_i spacing within each element where tissue homogeneity is a good approximation, this relationship may be simplified to the following:

$$\frac{1}{R_S C_S\,\omega} = \frac{\sigma}{\varepsilon\,\omega} \qquad (4.16)$$

Substituting the above in Equation 15 leads to:

$$\theta_s = -90^o + \text{Arctg}\,\left(\frac{\sigma}{\varepsilon\,\omega}\right) \qquad (4.17)$$

This equation shows that, unlike resistance and capacitance that depend on the electric field and element geometry in addition to the tissue intrinsic properties, the impedance phase angle is dependent on the intrinsic electrical properties of the tissue only. As such, phase angle images

are expected to be of higher quality compared to resistance and capacitance images. Moreover, phase angle imaging of the breast is feasible at lower frequencies (e.g. 10Hz-1kHz) only where the capacitance and phase angle components of the measured impedance are non-zero. It is noteworthy that at frequencies close to zero, the reactance and phase angle of a biological tissue also tend to zero and can not be measured reliably. Therefore, this type of image reconstruction may not be feasible at frequencies close to zero.

It is noteworthy that in this study it is assumed that breast tissue is almost homogenous consisting mainly of adipose tissue. As such, the impedance phase angle for the breast tissue at low frequencies can be approximated by equation 4.17.

4.2.5. Proposed Electrical Impedance Mammography System

A custom-made electrical impedance mammography scanner was constructed for our experimental studies. It consists of two parallel plates where the breast is placed in between before image acquisition is performed. One plate is used for excitation while the other is a sensor plate. The excitation plate includes the excitation board while the other is a hand-held plate which consists of a sensor board and analog and digital boards. The excitation board consists of a large conductive plate and an electronic board on the back, which generates the excitation sinusoidal signals with selectable frequency at 5 $V_{p\text{-}p}$. The sensor board consists of a 1-D circular cells array moved at 5 mm increments along the top surface of the breast to scan its entire volume. The 1-D array consists of thirty circular cells. The radius of each cell is 1.5 mm; each one is separated from the next by a gap of 0.125 mm on the printed circuit board (PCB). For data acquisition, the breast was squeezed gently between the scanner and excitation board. The impedance signals, which were obtained from the cells of the 1-D array, were first amplified by the analog circuit board before they were sent to the digital board. The digital circuit board consists of multiple 24 bit analog to digital converters (AD7766, Analog Devices, Massachusetts, USA) and a microcontroller (ATmega320, Atmel, California, USA). AD7766 converts the analog impedance signal into 24 bits digital packets and sends them through the USB port to a computer. A Matlab (MathWorks, Massachusetts, USA) code on the computer side, which is connected to the scanner through the USB port, receives the digital impedance

data and converts them into 2D digital images. The microcontrollers on the digital board of the scanner does all the coordination between the A/D converter and computer. The whole procedure is completed in less than 10 seconds.

A schematic of the proposed sensor in this study is illustrated in Figure 4.3. Each conductive cell on the sensor board is connected to a custom-made impedance measurement circuit that measures the impedance amplitude and phase angle of the adjacent breast tissue with 0.1Ω and 0.01° accuracy, respectively.

The measured tissue's impedance components (the tissue's resistant and capacitance) by the proposed sensor, can be described theoretically by equations (4.10) and (4.13). As these equations show, the measured tissue's resistance (R) and capacitance (C) are highly dependant on the electric field (E) inside the tissue between the parallel plates, the contact area of each conductive cell (A), separation between the sensor plates (L) and dielectric property of the tissue (σ and ε). If the electric field between the sensor plates was uniform, the equations (4.10) and (4.13) could be simplified to $R = \frac{L}{\sigma A}$ and $C = \frac{\varepsilon A}{L}$, respectively. This implies if E was uniform, for a constant A and L, the measured tissue's resistance and capacitance would be functions of tissue dielectric properties, σ and ε only.

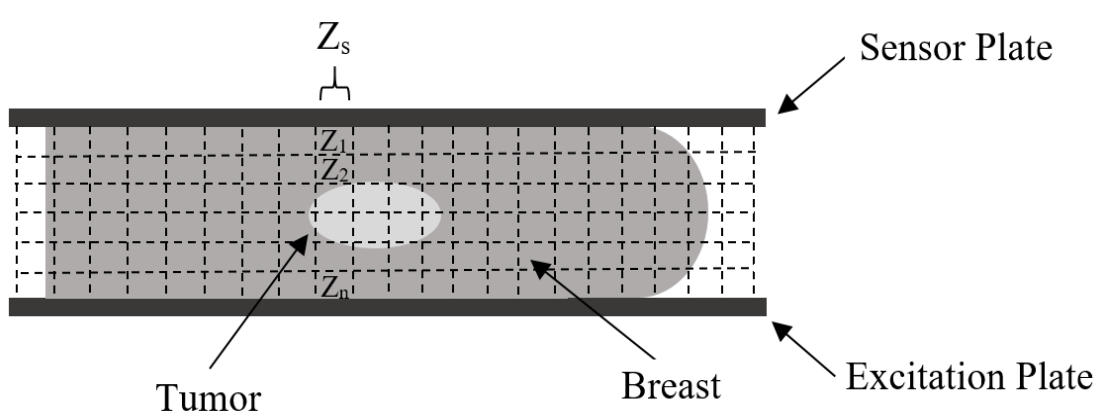

Figure 4.3. Schematic of the proposed EIM sensor consisting of two conductive parallel plates where the breast is gently squeezed in between. The breast is discretized using a uniform grid size where unknown impedance values are assigned to each pixel.

4.2.6. *In silico* Breast Phantom Study

To assess the capability of the proposed sensor for breast cancer detection, and to evaluate the three methods of conductance, permittivity and phase angle imaging, a series of computer simulations were carried out on a phantom following the configuration shown in Figure 4. The simulations were carried out using the COMSOL Multiphysics software package. The phantom mimics a breast gently compressed by two plates, hence it consists of a half-cylinder with a radius of 75 mm and height of 50 mm. It embeds a cylindrical inclusion with a radius and thickness of 10mm and 20mm, respectively. In order to increase the simulation's realism, the inclusion was positioned as illustrated in Figure 4 in order to mimic the upper outer quadrant where the majority of breast cancer tumors are found [31]. The location of the inclusion along the height of the cylindrical phantom was set to be variable such that the inclusion's centre was located at the centres of the bottom, middle and top thirds along the height. The permittivity and conductivity values assigned to the breast model were chosen based on values reported in the literature for breast tissue at 0.5 kHz. The inclusion's permittivity and conductivity values were assumed to be 6 and 8 times higher than normal breast tissue's conductivity and permittivity, respectively. The breast phantom's FE mesh, which is illustrated in Figure 4.4, consisted of ~2.7 million tetrahedral elements. Similar to the proposed sensor, one conductive plate was modeled to touch the breast model from the bottom to provide an excitation signal, while the top plate (sensor) was considered to measure the impedance. The sensor plate consisted of 30 circular conductive cells, each with a radius of 1.5 mm and separation of 0.2 mm. The COMSOL solver used the FEM approach to numerically solve Maxwell's equations and compute the amplitude and phase angle of the electric current that passed through each sensor cell. From these computations, the impedance values of the breast tissue located between each cell and excitation plate was acquired sequentially. To obtain the projected mammography image of the resistance and capacitance, the required projection value for each cell was calculated using Equations 4.11 and 4.12.

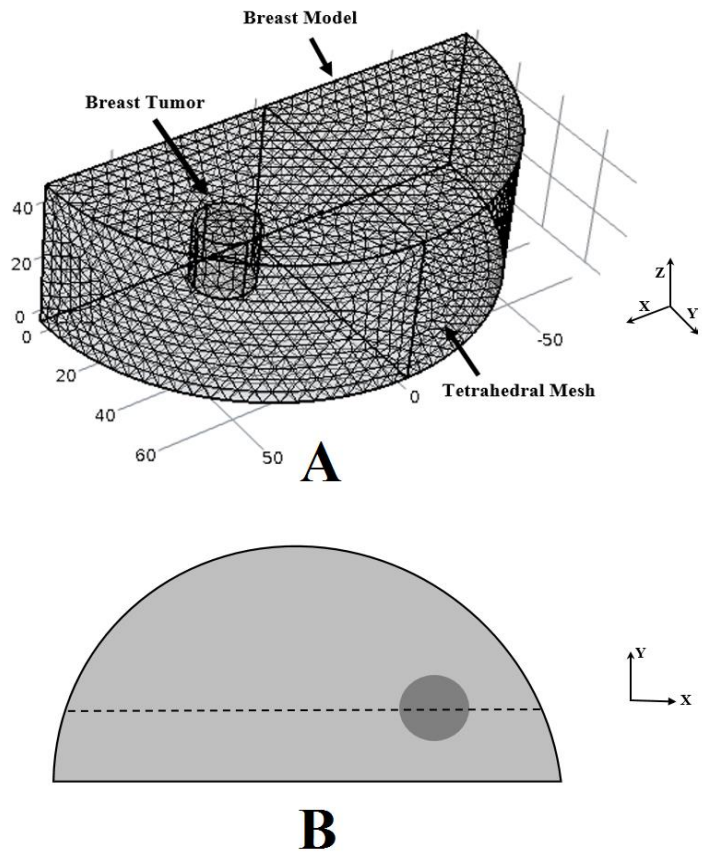

Figure 4.4. A: FE mesh of the in silico breast phantom consisting of half a cylinder embedding an inclusion. **B:** Top view of the breast model with the inclusion on the bottom right side to mimic the breast upper outer quadrant.

4.2.7. Tissue Mimicking Breast Phantom Study

A tissue mimicking phantom study was performed to assess the effectiveness of the proposed imaging techniques. As shown in Figure 4.5, the gelatine phantom consists of half a cylinder background tissue embedding a cylindrical inclusion constructed of gelatin and common salt. The background half cylinder part was 150 mm in diameter and 50 mm in height while the diameter and height of the cylindrical inclusion were both 20 mm. Along the phantom's height, the inclusion was placed in the middle. The conductivity and permittivity of the background and inclusion tissues were measured independently prior to image data acquisition. At 0.5 kHz, their conductivity were 0.23 S/m and 1.2 S/m while their relative permittivity were 1,084,454 and 8,546,138 for the background and inclusion, respectively. Each of these values were obtained by placing a small block shape representative sample between the two electrodes of the apparatus

shown in Figure 1 followed by measuring the resultant resistance and capacitance values. The conductivity and permittivity values of each tissue were then calculated using a 2-D optimization algorithm where the samples' FE models were used to calculate the resultant resistance and capacitance values corresponding to the current estimates of conductivity and permittivity values in the optimization process. The algorithm altered the conductivity and permittivity of the sample's FE model systematically until the mismatch between the calculated and experimentally measured resistance and capacitance values was minimum. To construct the phantom, gelatin and common salt with various concentrations were used. For the background, 12% concentration of gelatin in distilled water was used while for making the inclusion 12% of gelatin and 0.09% common salt was used. The experimental setup consisted of the data acquisition described earlier where an excitation voltage of the sensor was set to 5 $V_{p\text{-}p}$ at 0.5 kHz.

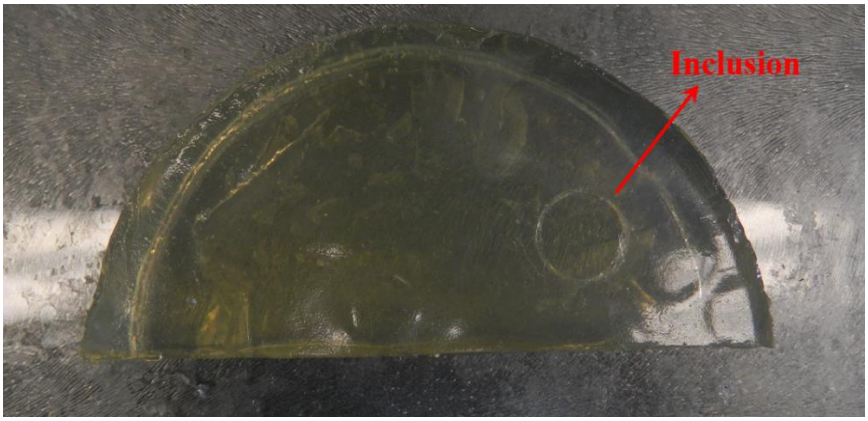

Figure 4.5. Gelatin breast phantom with inclusion located in the bottom right side to mimic the breast upper right quadrant.

4.3. Results

4.3.1. *In silico* Breast Phantom

Images reconstructed from the *in silico* breast phantom are shown in Figure 4.6. They show 2D mammography images obtained by projection of the impedance, resistance, capacitance, and phase angle of the breast phantom corresponding to three different tumor positions along its height (z-axis). The images were produced from raw simulation data with no additional filtering

or manipulation. As described earlier, the permittivity images is similar to the capacitance images while the conductivity images are similar to inverted resistance images. Thus, the permittivity and conductivity images of the breast phantom are not shown. Variation profiles of the measured impedance, resistance, capacitance and phase angle of the *in silico* breast phantom along the section crossing the inclusion (shown in Figure 4B) are also illustrated in Figure 4.6. Due to symmetry, the reconstructed images of the phantom with the inclusion located at the centres of low and top height thirds quadrants (rows 1, 2 and 5, 6) are identical. As expected, image contrast pertaining to these two cases is higher compared to the case where the inclusion is located in the middle of the phantom's height. This is particularly more important with the impedance and resistance images where the respective images can hardly detect the inclusion. Among the reconstructed images, the capacitance and phase angle images exhibited higher contrast and better quality compared to the impedance and resistance images.

The results revealed that there are artifacts seen as intensity variations around the phantom and inclusion's periphery in the reconstructed impedance, resistance, and capacitance images. These artifacts were caused by the nonlinearity and non-uniformity of the electric field. This led to about 9% higher measured impedance and resistance, and about 10% lower measured capacitance around the peripheries as shown in the 2nd, 4th, and 6th rows of Figure 4.6.

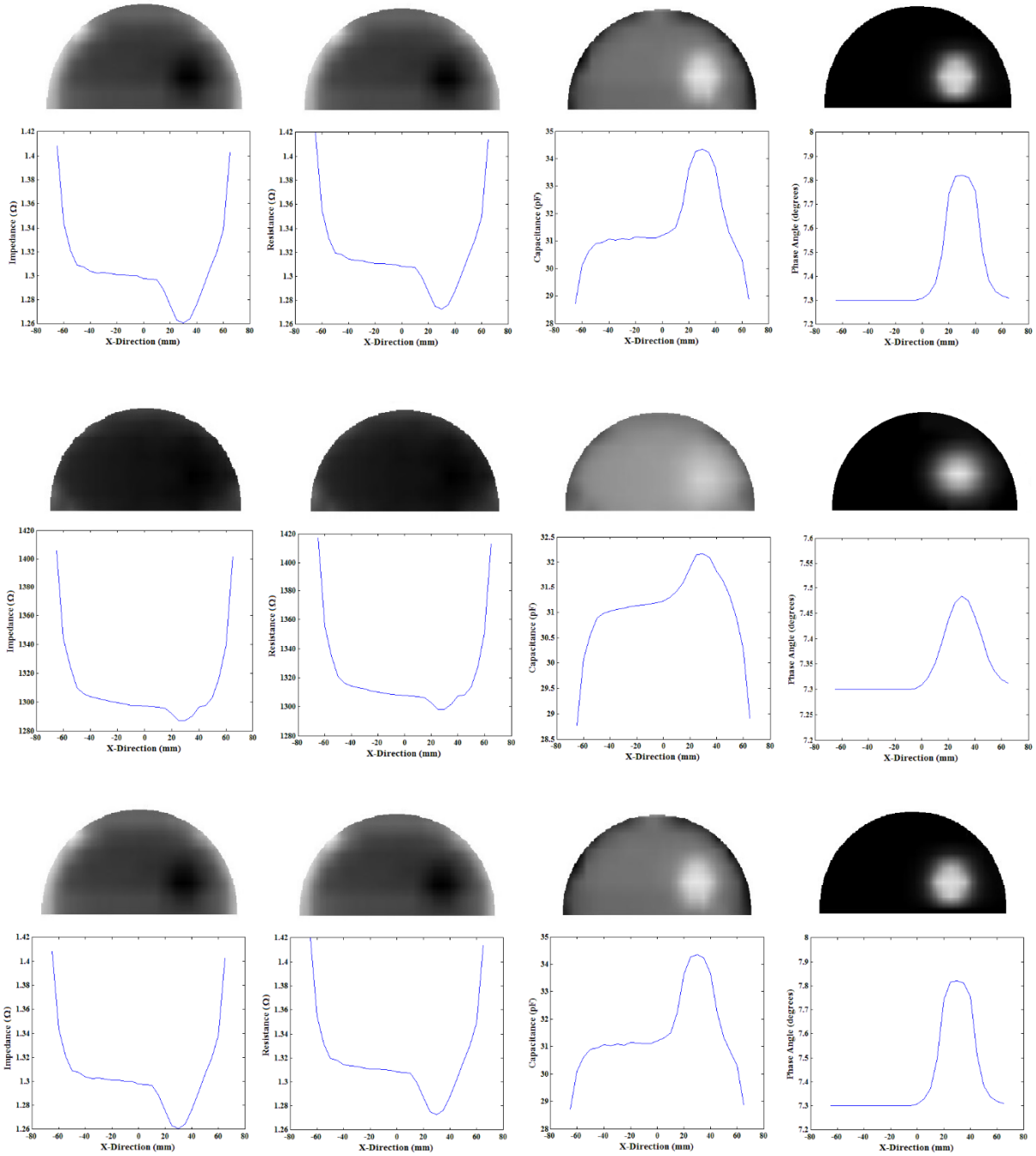

Figure 4.6. From left to right: reconstructed impedance, resistance, capacitance and phase angle images of the in silico breast phantom where the inclusion is located at the centers of the height's of a) top third (1st row), b) middle third (3rd row) and c) bottom third (5th row). Also, from left to right: variations profile of the impedance, resistance, capacitance and phase angle along a section crossing the middle of the inclusion corresponding to the in silico breast phantom where the inclusion is located at the centers of the height's of a) top third (2nd row), b) middle third (4th row) and c) bottom third (6th row).

4.3.2. Tissue Mimicking Breast Phantom

Reconstructed images obtained from the tissue mimicking breast phantom study are shown in Figure 4.7. Pixel size in these images is 3 mm×5 mm. This figure demonstrates that the inclusion can be clearly distinguished from the background on the capacitance and phase angle images. Similar to the reconstructed images obtained from the *in silico* breast phantom study, the inclusion in the impedance and resistance images of the gelatin phantom cannot be clearly differentiated from its background. The second row of Figure 4.7 illustrates the variation profiles of the impedance, resistance, capacitance, and phase angle signals along the section crossing the inclusion.

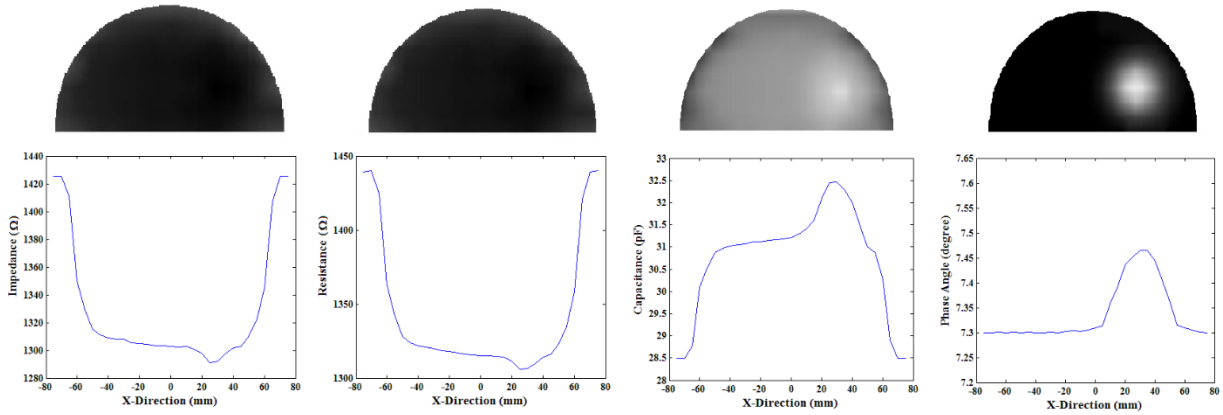

Figure 4.7. Top row from left to right: Reconstructed impedance, resistance, capacitance and phase angle images obtained from the tissue mimicking breast phantom study. Bottom row from left to right: variation profiles of the impedance, resistance, capacitance and phase angle signals along the section crossing the inclusion.

4.4. Discussion and Conclusions

It is known that breast tissue in women undergoes significant changes because of different factors such as pregnancy, aging, menstrual cycle, menopause, etc. These changes are expected to affect the intrinsic properties of the breast tissue such as dielectric properties. However, previous studies have shown whatever the intrinsic properties of the breast tissues are, cancer tumors tend to have significantly higher dielectric values than their healthy counterparts. In this

study, we introduced an electrical impedance mammography approach which takes advantage of this higher dielectric values in order to detect breast abnormalities in an effective, safe, simple and cost effective way. Based on the components of tissue electrical impedance, we introduced methods to obtain three independent images of the breast. These images can be constructed using data obtained from a single data acquisition procedure while only extra computer resources are required for constructing the three images. Our *in silico* and tissue mimicking phantom studies indicated that, among these images, the permittivity, capacitance and phase angle images were shown to be more effective than the impedance, resistance and conductivity images. Moreover, the studies demonstrated that the phase angle image reconstruction was capable of producing the highest quality images consistent with Equation 4.17, which implied strict dependence on the tissue intrinsic properties.

Based on the simulation results obtained from an adipose tissue specimen, an excitation frequency of 0.5 kHz was chosen to reconstruct the capacitance, permittivity and phase angle images of the breast phantom. The data presented in Section 4.2.4 demonstrated that significantly higher excitation frequencies may not be effective for producing images with high quality, as the capacitance component of the tissue's impedance at higher frequencies becomes too small to be measured reliably. Based on dielectric parameter values of different tissues at frequencies of 10 Hz – 20 GHz [24, 25], the same trend is expected to be observed for other soft tissue types at high frequencies.

Results obtained in this study suggest that breast inclusions with higher dielectric values are highly detectable when they are located in the top outer quadrant of the breast. This may be highly advantageous for breast cancer detection, as previous research has shown that the majority of cancer tumors form in the top outer quadrant of breast [31]. Higher conductivity and permittivity of an inclusion also leads to improved tumor detection characterized by higher image contrast. Previous studies have shown that the dielectric values of breast cancer tumors are 20-40-fold higher than those of normal breast tissue [12]. In this investigation however, we assigned only conservative 6 and 8 times higher values of conductivity and permittivity to the inclusion in the *in silico* and tissue mimicking phantom studies. Figures 4.8 and 4.9 show the real location and size of the inclusion using red dotted outlines on the projection images obtained from the *in silico* and phantom mimicking studies, respectively. These figures indicate that the

projection images are be able to properly capture the location of inclusions with higher dielectric parameter values. However, the size of the inclusion in these images increase with depth. For example, the inclusion in the image corresponding to the case where the inclusion is located in the breast's mid-height appears more diffused, hence its sizes is overestimated in comparison with the images corresponding to cases where the inclusion is located in the top or bottom one-third heights. These size variations are due to the electric field nonuniformity. Results obtained from this investigation indicate that, among images produced by the proposed method, the phase angle image is superior in terms of cancer detectability. These results also suggest that the proposed EIM technique is capable of detecting inclusions located deep inside the breast while other EIM technologies such as TransScan are only capable of detecting inclusions located close to the breast surface [33].

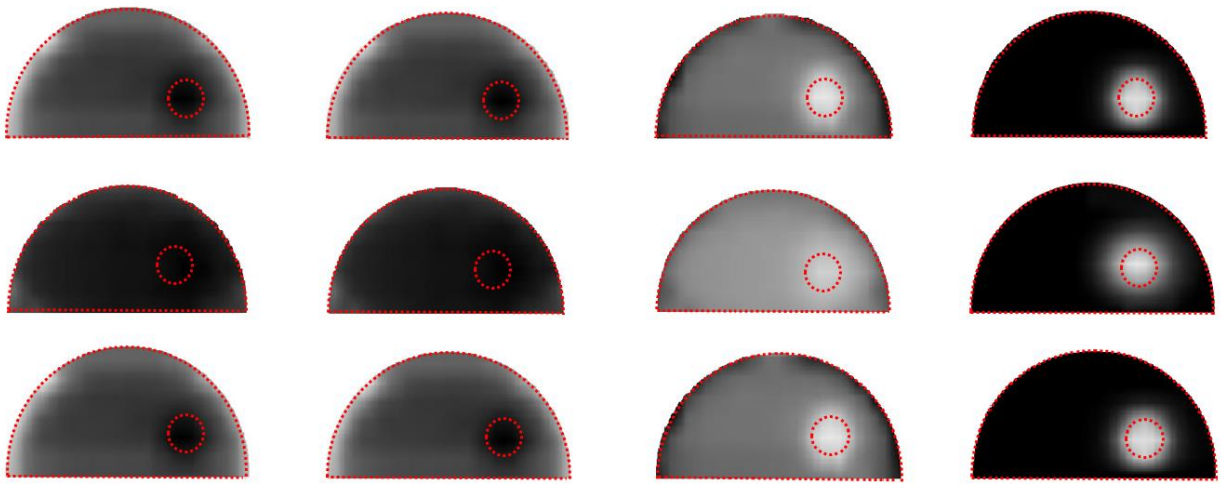

Figure 4.8. Reconstructed impedance, resistance, capacitance and phase angle images of the in silico breast phantoms previously shown in Figure 4.6 where the true location and size of the inclusion is shown using red dotted outlines.

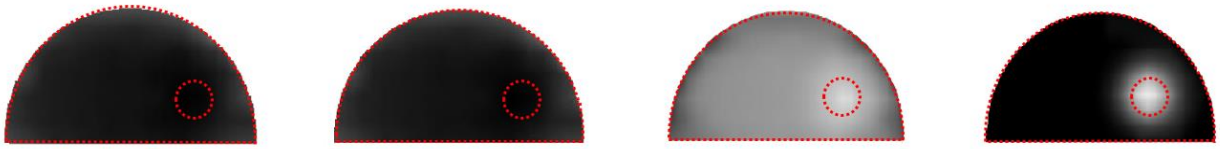

Figure 4.9. Reconstructed impedance, resistance, capacitance and phase angle images of the tissue mimicking breast phantom previously shown in Figure 4.7 where the true location and size of the inclusion is shown using red dotted outlines.

References

[1] Howlader N, Noone AM, Krapcho M, Garshell J, Miller D, Altekruse SF, Kosary CL, Yu M, Ruhl J, Tatalovich Z, Mariotto A, Lewis DR, Chen HS, Feuer EJ, Cronin KA (eds). SEER Cancer Statistics Review, 1975-2012, National Cancer Institute. Bethesda, MD, http://seer.cancer.gov/csr/1975_2012/, based on November 2014 SEER data submission, posted to the SEER web site, April 2015, last access to the website: Nov. 3, 2016

[2] American Cancer Society. Cancer Facts & Figures 2015. Atlanta: American Cancer Society; 2015

[3] J. G. Elmore, K. Armstrong, C. D. Lehman, and S.W. Fletcher, "Screening for breast cancer," *J. Am. Med. Assoc.* 293(10), 1245–1256 (2005)

[4] J. G. Elmore, M. B. Barton, V. M. Moceri, S. Polk, P. J. Arena, and S.W. Fletcher, "Ten-year risk of false positive screening mammograms and clinical breast examinations, "*N.Engl. J. Med.* 338(16), 1089–1096 (1998)

[5] Molly L. Flexman, Michael A. Khalil, Rabah Al Abdi, Hyun K. Kim, Christopher J. Fong, Elise Desperito, Dawn L. Hershman, Randall L. Barbour and Andreas H. Hielscher; Digital optical tomography system for dynamic breast imaging; Journal of Biomedical Optics 16(7), 076014 (July 2011)

[6] A. Malicha, T. B. ohmb, M. Faciusa, I. Kleinteicha, M. Flecka, D. Saunera, R. Andersonc, W.A. Kaisera; Electrical impedance scanning as a new imaging modality in breast cancer detection—a short review of clinical value on breast application, limitations and perspectives; Nuclear Instruments and Methods in Physics Research A 497 (2003) 75–81

[7] O V Trokhanova, M B Okhapkin and A V Korjenevsky; Dual-frequency electrical impedance mammography for the diagnosis of non-malignant breast disease; Physiol. Meas. 29 (2008) S331–S344 doi:10.1088/0967-3334/29/6/S28

[8] Y. Zou, Z. Guo, A review of electrical impedance techniques for breast cancer detection, Medical Engineering & Physics 25 (2003) 79–90

[9] William T. Joines, Randy L. Jirtle, Marc D. Rafal, Daniel J. Schaefer; Microwave power absorption differences between normal and malignant tissue, International Journal of Radiation Oncology Biology Physics, Volume 6, Issue 6, June 1980, Pages 681–687

[10] Gerard H. Markxa, Christopher L. Daveyb, The dielectric properties of biological cells at radiofrequencies: Applications in biotechnology, Enzyme and Microbial Technology 25 (1999) 161–171

[11] H. Fricke, S. Morse, The Electric Capacity of Tumors of the Breast, J. Cancer Res. 16 (1926) 340

[12] ANDRZEJ J. SUROWIEC, STANISLAW S. STUCHLY, J. ROBIN BARR, AND ARVIND SWARUP, Dielectric Properties of Breast Carcinoma and the Surrounding Tissues, IEEE TRANSACTIONS ON BIOMEDICAL ENGINEERING, VOL. 35, NO. 4, APRIL 1988

[13] Hardik J. Pandya1, Hyun Tae Kim, Rajarshi Roy, Wenjin Chen, Lei Cong, Hua Zhong, David J. Foran, and Jaydev P. Desai, Towards an Automated MEMS-based Characterization of Benign and Cancerous Breast Tissue using Bioimpedance Measurements, Sens Actuators B Chem. 2014 August 1; 199: 259–268. doi:10.1016/j.snb.2014.03.065

[14] William T. Joines, Randy L. Jirtle, Marc D. Rafal, Daniel J. Schaefer; Microwave power absorption differences between normal and malignant tissue, International Journal of Radiation Oncology Biology Physics, Volume 6, Issue 6, June 1980, Pages 681–687

[15] B. Rigaud, J.P. Morucci, N. Chauveau, Bioelectrical impedance techniques in medicine. Part I: Bioimpedance measurement. Second section: impedance spectrometry, Clin. Rev. Biomed. Eng. 24 (1996) 257

[16] J. Cuzick, R. Holland, V. Barth, R. Davies, M. Faupel, I. Fentiman, H.J. Frischbier, J.L. LaMarque, M. Merson, V. Sacchini, D. Vanel, U. Veronesi, Electropotential measurements as a new diagnostic modality for breast cancer, Lancet 352(9125) (1998) 359-363

[17] Gerard H. Markxa, Christopher L. Daveyb, The dielectric properties of biological cells at radiofrequencies: Applications in biotechnology, Enzyme and Microbial Technology 25 (1999) 161–171

[18] Ryan J. Halter, Member, IEEE, Alex Hartov and Keith D. Paulsen, A Broadband High-Frequency Electrical Impedance Tomography System for Breast Imaging, 650 IEEE TRANSACTIONS ON BIOMEDICAL ENGINEERING, VOL. 55, NO. 2, FEBRUARY 2008

[19] Ye, G., Lim, K. H., George, R., Ybarra, G., Joines, W. T., & Liu, Q. H. (2006). A 3D EIT system for breast cancer imaging. 2006 3rd Ieee International Symposium on Biomedical Imaging: Macro to Nano, Vols 1-3, 1092-1095

[20] Ye, G., Lim, K. H., George, R. T., Ybarra, G. A., Joines, W. T., & Liu, Q. H. (2008). 3d Eit for Breast Cancer Imaging: System, Measurements, and Reconstruction. Microwave and Optical Technology Letters, 50(12), 3261-3271

[21] X Zhang, C Chatwin, and D C Barber, A feasibility study of a rotary planar electrode array for electrical impedance mammography using a digital breast phantom, Physiol. Meas. 36 (2015) 1311–1335

[22] Myoung Hwan Choi, Tzu-Jen Kao, David Isaacson, Gary J. Saulnier, and Jonathan C. Newell , A Reconstruction Algorithm for Breast Cancer Imaging With Electrical Impedance Tomography in Mammography Geometry, IEEE TRANSACTIONS ON BIOMEDICAL ENGINEERING, VOL. 54, NO. 4, APRIL 2007

[23] V Cherepenin, A Karpov, A Korjenevsky, V Kornienko, A Mazaletskaya, D Mazourov and D Meister, A 3D electrical impedance tomography (EIT) system for breast cancer detection, V Cherepenin, A Karpov, A Korjenevsky, V Kornienko, A Mazaletskaya, D Mazourov and D Meister, Physiol. Meas. **22** (2001) 9–18

[24] The dielectric properties of biological tissues: I. Literature survey, C Gabriel, S Gabriely and E Corthout, Phys. Med. Biol. 41 (1996) 2231–2249. Printed in the UK

[25] S Gabriel, R W Lau and C Gabriel, The dielectric properties of biological tissues: II. Measurements in the frequency range 10 Hz to 20 GHz, Phys. Med. Biol. 41 (1996) 2251–2269. Printed in the UK

[26] Cheney M, Isaacson D, Newell JC. Electrical impedance tomography, SIAM Rev 1999;41(1):85–101

[27] Roberto Cardu, Philip H W Leong, Craig T Jin, Alistair McEwan, Electrode contact impedance sensitivity to variations in geometry, Physiol. Meas. 33 (2012) 817–830 doi:10.1088/0967-3334/33/5/817

[28] Wang W and Eisenberg S R 1994 A three-dimensional finite element method for computing magnetically induced currents in tissues *IEEE Trans. Magn.* 30 5015–23

[29] Comsol 4.3, AC/DC Module User's Guide, 2012

[30] David K. Cheng, Field and Wave Electromagnetics, 1989

[31] Vance Y. Sohn, M.D. , Zachary M. Arthurs, M.D., James A. Sebesta, M.D., Tommy A. Brown, M.D., Primary tumor location impacts breast cancer survival, The American Journal of Surgery (2008) 195, 641–644

[32] Ursula G. Kyle, Ingvar Bosaeus, Antonio D. De Lorenzo, Paul Deurenberg, Marinos Elia, Jose Manuel Gomez, Berit Lilienthal Heitmann, Luisa Kent-Smith, Jean-Claude Melchior, Matthias Pirlich, Hermann Scharfetter, Annemie M.W.J. Schols, Claude Pichard,

Bioelectrical impedance analysis part I: review of principles and methods, Clinical Nutrition (2004) 23, 1226–1243

[33] Michel Assenheimer, Orah Laver-Moskovitz, Dov Malonek, David Manor, Udi Nahaliel, Ron Nitzan1 and Abraham Saad, The T-SCANTM technology: electrical impedance as a diagnostic tool for breast cancer detection, Physiol. Meas. 22 (2001) 1–8

[34] Gupta D, Lammersfeld CA, Burrows JL, Dahlk SL, Vashi PG, Grutsch JF, Hoffman S, Lis CG, Bioelectrical impedance phase angle in clinical practice: implications for prognosis in advanced colorectal cancer. Am J Clin Nutr. 2004 Dec;80(6):1634-8

[35] Barbosa-Silva, Maria Cristina G, Barros, Aluísio JD, Bioelectrical impedance analysis in clinical practice: a new perspective on its use beyond body composition equations, Current Opinion in Clinical Nutrition & Metabolic Care: Pharmaceutical aspects, devices and techniques; May 2005 - Volume 8 - Issue 3 - p 311–317

Chapter 5

Conclusions and Future Work

5.1. Conclusions

A low frequency bio-electrical impedance mammography technique with different types of impedance data projections in conjunction with low frequency tissue dielectric measurement techniques were introduced in this investigation. As described earlier, the proposed impedance mammography technique is founded on the assumption that the dielectric values of breast malignancies at low frequencies are significantly higher than the dielectric values of healthy breast tissues; therefore, they are detectable through impedance measurement of the breast tissue. In the mammography technique proposed in this study, the breast is gently compressed between the two plates of the impedance sensor and impedance projections of the breast tissue on the breast surface plane are measured and converted into 2D mammograms. The impedance sensor consists of an excitation and sensor plates. The excitation plate provides a low voltage sin-wave excitation signal at low frequencies. The sensor plate consists of a 2D array of electrodes that measure the amplitude and phase of the impedance on the breast surface plane. Previous studies have indicated that existing impedance mammography systems such the TransScan 2000 (Siemens Medical, Germany, and TransScan, Ramsey, NJ, USA) are only capable of detecting malignancies located close to the breast surface. Based on *in silico* and tissue mimicking phantom studies carried out in this investigation we showed that our proposed impedance mammography technique in conjunction with phase angle image reconstruction is capable of detecting malignancies which are located deep inside or close to the surface of breast.

In order to assess the validity of the assumption that breast malignancies at low frequencies have substantially higher dielectric values than normal breast tissues, we conducted dielectric measurements on normal and malignant breast tissues in a xenograft mice model at 100 Hz-1 MHz. The outcome of this measurement indicated that both conductivity and permittivity values were significantly higher in breast cancer in comparison with normal breast tissues. The average conductivity of malignant to normal breast tissues were 2.1 to 5.1 times higher than that of surrounding normal tissues at 100 Hz-1 MHz, while the average permittivity of the breast tumors

were 8.4 to 13.4 times higher than that of the surrounding normal tissues. Permittivity values of the tumors in this study were ~80 times higher than reported values of permittivity of breast adipose at 100Hz-1MHz. The higher permittivity than conductivity ratios of malignant to normal breast tissue, shows the merit of permittivity and phase angle image reconstructions for detecting the breast malignancies. To reliably measure the dielectric properties of biological tissues at low frequencies, an inverse finite element computational approach in conjunction with using a parallel plate impedance sensor was presented in Chapter 2 of this study. In this approach the tissue specimen is placed between the plates of the impedance sensor and the amplitude and phase of the specimen's impedance is measured. The measured phase and amplitude of the impedance, or extracted resistance and capacitance of the tissue specimen are then used in an inverse finite element algorithm for calculating the permittivity and conductivity of the tissue specimen. The permittivity measurements of the bovine specimens and *in silico* studies of Chapter 2 suggest that the proposed dielectric measurement technique is comparable and even superior to the conventional VNA-based approach of measuring dielectric properties of biological tissue at low frequencies. It was shown through computer simulation that the inaccuracy of the conventional VNA-based approach in measuring the dielectric properties of a tissue such as breast which consist of layers of adipose and fibro-glandular tissues can be as high as 270%, while the maximum error associated with our proposed dielectric measurement technique in this study for the same breast tissue is only 4%. An improved version of the proposed dielectric measurement technique which uses cylindrical shaped electrodes instead of parallel plates sensor, was presented in the Chapter 3 of this work. This technique was employed to estimate the conductivity and permittivity values of breast tumors at low frequencies of 100 Hz-1 MHz using a xenograft mice model.

5.2. Future Directions

5.2.1. Chapter 2: A Novel Technique for Measuring Electrical Permittivity of Biological Tissues at Low Frequencies

In this chapter a novel method for measuring the electrical permittivity of biological tissues at low frequencies was presented, and the permittivity of several bovine liver, heart and bone tissue specimens were measured by the proposed technique. Furthermore, a comparison between the

performance of the proposed and conventional VNA-based approaches for measuring the permittivity of a breast tissue model which consisted of layers of adipose and fibro-glandular tissues, was conducted through the *in silico* studies. To study the viability of impedance imaging and tissue characterization (i.e. differentiation of healthy and diseased tissues) for different organs (such as liver, lung, prostate, etc.), more variety of soft and hard tissue specimens, including human tissues specimens can be measured by the proposed and conventional technique in future works. The measurements for these tissue specimens can be carried out through a broad range of low frequencies such as 10Hz-10MHz. Resulting dielectric values from these two measurement methods can be compared to each other and to dielectric values reported in the literature. The proposed measurement method can also be modified to utilize different types and configurations of impedance sensors with different conductive plates and electrodes, in order to be suitable for different types of biomedical applications. Furthermore, the possibility of *in vivo* dielectric measurement of biological tissues should be investigated in future works. For this purpose, the possibility of using CT and MRI for obtaining the real geometries of organs and tissues maybe considered. The dielectric measurement of blood vessels in cancer tumors and in diseases such as sepsis can also be taken into account for future works. Furthermore, the sensitivity of dielectric variation to the blood oxygenation for detection of hypoxia can be investigated.

5.2.2. Chapter 3: Dielectric Properties of the Normal and Malignant Breast Tissues in Xenograft Mice at Low Frequencies (100Hz-1MHz)

The dielectric properties of normal and malignant breast tissues in xenograft mice model at frequencies of 100 Hz-1 MHz were investigated in Chapter 3 of this work. The results indicated that both conductivity and permittivity values in breast cancer tissues were significantly higher than normal breast tissues. In the future, more investigations can be conducted at low frequencies for measuring and comparing the dielectric values of normal and malignant human breast tissues obtained from surgeries. Also, more dielectric measurements can be carried out on different types of benign lesions and various breast malignancies to examine the possibility of using the tissue dielectric properties for differentiation between different categories and stages of benign and cancer breast lesions. Furthermore, the feasibility of the in vivo breast cancer dielectric

measurements both on human and on xenograft breast cancer model at low frequencies should be taken into consideration. The possibility of detecting hypoxia based on the changes in the dielectric values of oxygenated and deoxygenated blood, as well as the impact of the denser vasculature on dielectric values of cancer tumors can also be studied. Finally, the feasibility of using the electrical conductivity, permittivity and phase angle of breast tissues at low frequencies for finding tumor margins in breast lumpectomy procedure can be investigated.

5.2.3. Chapter 4: Towards Medical Electrical Impedance Mammography Using Low Frequency Excitation

The possibility of using electrical properties of biological tissues, such as electrical conductivity and electrical permittivity at low frequencies, for screening the breast and detecting its malignancies were investigated in Chapter 4 of this thesis. As described earlier, the results of this investigation is based on *in silico* and tissue mimicking phantom studies. A potential future research project can be directed toward clinical examination of the proposed impedance mammography system on breast cancer patients. Other future projects maybe designed to determine the minimum inclusion size that can be detected by the proposed impedance mammography system at different breast depths. Another future research project may involve determining the maximum resolution that can be obtained from the proposed impedance mammography technique and the relationship between this resolution and the sensor cell's area and plates separation. The viability of using different types and configurations of impedance sensor in conjunction with utilizing multiple excitation voltages and frequencies for obtaining the optimum projection signal from the impedance sensor at different inclusion's depth is also of interest, hence maybe considered as a future research project.

Appendix 1: Invention Report

UWO4-0050PCT PATENT

ELECTRICAL IMPEDANCE IMAGING

BACKGROUND OF THE INVENTION

Field of the Invention

I. The present invention relates to electrical impedance imaging, and more particularly to electrical impedance imaging for medical applications.

Description of the Related Art

II. Many current medical imaging methods have limitations such as tissue ionization, noise and high cost, which may impact their effectiveness in the clinic. For instance, X-ray and Computer Tomography (CT) imaging techniques, which are based on tissue attenuation coefficient, both expose patients to radiation and also are not capable of generating images with high contrast for many soft tissue regions. In contrast to X-ray and CT, MRI does not involve exposure to radiation, but is expensive and often requires contrast agents for imaging tissues. Another common imaging modality is ultrasound which visualizes tissue acoustic properties. This modality often suffers from high levels of noise, frequently leading to low quality imaging. In addition to these limitations, it is known that various imaging modalities display only specific types of data (e.g. morphology, microcalcification, etc.) pertaining to tissue pathology. As such, clinicians often use the approach of fusing data obtained from different modalities for more accurate diagnosis.

III. Imaging techniques are founded on tissue physical properties that are reconstructed by processing measured data using a mathematical framework which describes the physics of interaction between tissue and its excitation. The heterogeneity various tissues exhibit in terms of the physical property used in an imaging technique influences the medical image contrast in clinical applications, and affects the technique's sensitivity and specificity. Among tissue physical properties that have not been sufficiently explored for developing effective medical imaging techniques, electrical properties have good potential. While tissue electrical impedance (EI) has been somewhat explored for medical imaging, leading to the Electrical Impedance Tomography (EIT) technique, electrical permittivity (EP) or electrical capacitance (EC) have not been given significant attention in the medical imaging field. [Does this last sentence imply that EI is mutually exclusive of EC and EP? Does EI encompass EP and EC?] While EIT has been developed and significantly improved over the past two decades, it still suffers from two major drawbacks which have limited its clinical utility. The first is that the range of EI variation for most biological tissues at low frequencies, i.e. 100 KHz or lower, is limited (S Gabriel, R W Lau and C Gabriel, The dielectric properties of biological tissues: III. Parametric models for the dielectric spectrum of tissues, Phys. Med. Biol. 41 (1996) 2271–2293. S Gabriel, R W Lau and C Gabriel, The dielectric properties of biological tissues: II. Measurements in the frequency range 10 Hz to 20 GHz, Phys. Med. Biol. 41 (1996) 2251–2269). This means that obtaining high contrast EI images at low frequencies is often not feasible. The second is that imaging tissue with

EI requires the use of contacting electrodes. However, in many clinical applications, contacting electrodes either cannot be used or using the required number of electrodes is impractical.

IV. Accordingly, there is a continuing need for alternative medical imaging techniques.

V.

SUMMARY OF THE INVENTION

VI. In an aspect there is provided an electrical permittivity tomography sensor, comprising:

VII. a first planar plate comprising a plurality of excitation cells;

VIII. a second planar plate comprising a plurality of detector cells**;**

IX. the first planar plate held in spaced parallel relation to the second planar plate and defining a chamber therebetween;

X. the first and second planar plates arranged to align each excitation cell with a corresponding detector cell in a one-to-one paired relationship; and

XI. each paired excitation cell and detector cell configured for synchronized activation with a substantially uniform electric field communicating therebetween.

XII.

BRIEF DESCRIPTION OF THE DRAWINGS

XIII. Figure 1 shows a schematic view of a capacitive sensor;

XIV. Figure 2 shows a schematic cross-sectional view of a prior art capacitive sensor;

XV. Figure 3 shows a 2D non-uniform electric field in a homogeneous medium within the prior art capacitive sensor shown in Figure 2;

XVI. Figure 4 shows a computer controlled imaging system comprising the capacitive sensor shown in Figure 1;

XVII. Figure 5 shows a schematic of a sample section of a phantom consisting of two tissues (e.g. background healthy tissue and tumor) placed between two-parallel-plates of a diaphragm variant of the capacitive sensor shown in Figure 1;

XVIII. Figure 6 shows block shape phantoms with cylindrical inclusions with various sizes mimicking tumor in healthy background tissue used in an *in silico* phantom study for permittivity image reconstruction using data back propagation;

XIX. Figure 7 shows a tissue mimicking phantom consisting of background and inclusion with permittivity values of 180 F/m and 420 F/m, respectively;

XX. Figure 8 shows plots of deviation error from linear approximation vs. frequency along the centreline of *in silico* breast phantoms with 10, 15 and 25mm diameter spherical inclusions with permittivity values three times higher than the background tissue permittivity;

XXI. Figure 9 shows plots of deviation error from linear approximation vs. frequency along the centreline of *in silico* bone-muscle phantom for the 10, 15 and 25mm diameter cylindrical inclusions with permittivity values twenty times lower than the background tissue permittivity;

XXII. Figure 10 shows plots of deviation error from linear approximation along the diaphragm's motion axis in the *in silico* breast phantom consisting of a block with 15mm, 20mm and 25mm diameter cylindrical inclusions with permittivity values three times higher than the background tissue permittivity;

XXIII. Figure 11 shows reconstructed tomography images of the block phantoms shown in Figure 6 with 15, 20 and 25 mm inclusions (top row) and corresponding segmented images obtained with a threshold value of 2000F/m (bottom row);

XXIV. Figure 12 shows a plot of an experimentally acquired projection along the X-axis of the tissue mimicking phantom shown in Figure 7;

XXV. Figure 13 shows plots of (A) average values and (B) maximum values of the metric Δc as a function of permittivity and plate separation (phantom height);

XXVI. Figure 14 shows a schematic of a capacitive sensor plate with a guard surrounding each excitation cell; and

XXVII. Figure 15 shows a schematic of a needle biopsy variant of the capacitive sensor shown in Figure 1.

XXVIII.

DETAILED DESCRIPTION OF PREFERRED EMBODIMENTS

XXIX. In contrast to EI, EP of biological tissues has a broad range. For example, at 100MHz, EP of biological tissues varies from 6 F/m for fat to 56.2 F/m for brain white matter, and to 98 F/m for the kidney. The difference in tissue EP becomes even more significant at lower frequencies, so that at 1 KHz the EP values of the aforementioned tissues are 24104 F/m, 69811 F/m and 212900 F/m, respectively. Therefore, it can be concluded that image contrast and hence quality in EP imaging is potentially high. Table 1 presents EP values of six different human tissues at 100Hz, 100 KHz and 100 MHz (S Gabriel, R W Lau and C Gabriel, The dielectric properties of biological tissues: III. Parametric models for the dielectric spectrum of tissues, Phys. Med. Biol. 41 (1996) 2271–2293. S Gabriel, R W Lau and C Gabriel, The dielectric properties of biological tissues: II. Measurements in the frequency range 10 Hz to 20 GHz, Phys. Med. Biol. 41 (1996) 2251–2269). Table 1 shows that tissue EP values decrease significantly with higher frequencies. The significant variation observed in tissue EP while excited with different frequencies indicates an important potential advantage of EP imaging where excitation frequency may be determined/tuned for given anatomical sites to improve image contrast.

XXX. **Table1.** Frequency dependent variation of Electrical Permittivity of human tissues

Tissue name	Muscle	Bone (Cortical)	Blood	Brain (White m.)	Brain (Grey m.)	Fat
ε @ 100 Hz	9329000	5852.8	5259.8	1667700	3906100	457060
ε @ 100KHz	8089	227.6	5120	2108	3221	92.89
ε @ 100MHz	65.9	15.3	76.8	56.8	80.14	6.07

XXXI.

XXXII. Another important advantage of imaging EP over EI [Does this imply that EI is mutually exclusive of EP? Does EI encompass EP?]is the possibility of image data acquisition through capacitance measurement. Capacitive sensors usually consist of a number of electrodes or metal plates, and the electrical capacitance is usually estimated through measurement of the voltage and current that passes through them. Achieving high image resolution using capacitive sensors with electrodes is not practical because of the small number of relatively large electrodes used for data acquisition. Electrodes are discrete elements attached to the skin. Given the size of electrodes it is not possible to place a large enough number of such electrodes to achieve high image resolution - for example although 16 to 32 electrodes are typically used for imaging a thorax, this number of electrodes still does not produce a high resolution image.

XXXIII. Now referring to the drawings, Figure 1 shows an example of a capacitive sensor 10 that can be used for medical impedance imaging including, for example, medical electrical permittivity imaging or impedance phase angle imaging. The capacitive sensor 10 comprises two parallel planar plates, a first planar plate 12 housing a plurality of electrically

conductive excitation cells 14 arranged in a first array and a second planar plate 16 housing a plurality of electrically conductive detector cells 18 arranged in a corresponding second array. Each excitation cell 14 is electrically isolated from other neighboring excitation cells by surrounding a perimeter of the excitation cell 14 with a non-conductive insulating gap 20. Each detector cell 18 is electrically isolated from other neighboring detector cells by surrounding a perimeter of the detector cell 18 with a non-conductive insulating gap 20. Thus, the first and second planar plates are segmented by the non-conductive insulating material 20, with each segment of the first planar plate including a single excitation cell and each segment of the second planar plate including a single detector cell.

XXXIV. Each of the first and second planar plates are bound by first and second surfaces with an insulation layer 22 covering the first surface and a grounding shield 24 covering the second surface. The first and second planar plates are arranged so that their respective insulation layers 22 face each other.

XXXV. The first and second planar plates are maintained in a substantially parallel spaced relation defining a chamber 26 for receiving a biological sample in between the first and second planar plates. More specifically, the chamber 26 is defined in between the insulation layers 22 covering the first surfaces of the first and second planar plates. The insulation layers 22 provide contacting surfaces for the biological sample. The spacing between the first and second planar plates is adjustable so that surfaces of variously sized biological samples can be maintained in abutting contact with both the insulation layers 22 of the first and second planar plates.

XXXVI. The first and second planar plates are oriented so that an excitation cell and a corresponding detector cell are held in opposing alignment. When in use, each excitation cell and its corresponding detector cell are located on opposing sides of a biological sample. The plurality of excitation cells and the plurality of detector cells are typically equal in number so that each excitation cell opposes a detector cell in a one-to-one relationship (C'_1 to C_1, … , C'n to Cn). Each excitation cell and each detector cell can each be independently electrically controlled. A first multiplexer 28 comprises an input connector 30 in electrical communication with a voltage source and a plurality of relays, each relay 32 controlling electrical activation of a single excitation cell. The input connector 30 communicates an excitation signal from the voltage source through a closed relay to a corresponding excitation cell. The excitation signal may be modulated with respect to amplitude, frequency, or both amplitude and frequency. A second multiplexer 34 comprises an output connector 36 in electrical communication with data acquisition circuitry and a plurality of relays, each relay 38 controlling electrical communication of a single detector cell.

XXXVII. The first and second multiplexers function to synchronize any desired pattern of sequential activation or simultaneous activation of corresponding opposing pairs of excitation cells and detector cells to generate a substantially 1D uniform electric field traversing the chamber space through a biological sample, the substantially 1D uniform electric field having an orientation substantially perpendicular/normal to both the first and second planar plates. The data acquisition circuitry can measure an electrical property of a substantially 1D uniform electric field generated between each oppositely aligned pairing of a single excitation cell and a corresponding single detector cell. Typically, the measured electrical property is permittivity, conductivity or both permittivity and conductivity. [Insert here impedance for phase angle?]

XXXVIII. The schematic capacitive sensor has been validated experimentally. The following experimental examples are for illustration purposes only and are not intended to be a limiting description.

XXXIX. In a first set of experimental examples the capacitive sensor is used to determine electrical permittivity (EP) of a sample held between the two parallel plates and process the EP data to generate an image of the sample.

XL. Electrical permittivity (denoted by ε), is a parameter that shows how much electric field is generated per unit charge in a medium. It is usually measured through measuring electrical capacitance (C) as direct measurement of ε may not be feasible. Electrical Capacitance (C) is a physical property of capacitors consisting of two conductors with a material (medium) between them and it can be measured using capacitive sensors. It is a property of the capacitor which depends on the geometry of the conductors and the permittivity of the medium between them; it does not depend on the charge or potential difference between the conductors. The following is a fundamental relationship used to express C:

XLI. $$C = \frac{\mathrm{Q}}{\mathrm{V}} = \frac{\oint \varepsilon E.\ ds}{\int E.\ dl} \quad (1)$$

XLII. where Q is the electric charge, V the voltage between electrodes and E is the electric field. The surface integral in the numerator is carried out over the surface enclosing the conductor while the line integral in the denominator is calculated from the negative to positive conductor or low to high potential. As it can be seen from this relationship, if E is uniform, C will be proportional to the permittivity of medium between the electrodes or plates of the capacitive sensor.

XLIII. Most current Electrical Capacitance Tomography (ECT) systems have used a relatively simple electrode configuration with electrodes arranged around the periphery of the object being imaged. For data acquisition, one pair of the electrodes is activated at a time and the corresponding capacitance is measured. Another approach of medium excitation involves exciting one electrode with a positive potential while the other electrodes are activated with a negative voltage. For data acquisition, again the capacitance values between pairs of the positive electrode with each negative electrode are measured. Figure 2 shows a typical configuration of a capacitive sensor which is used by most researchers in the field, including, for example, Soleimani et al. (Manuchehr Soleimani, Phaneendra K. Yalavarthy, Hamid Dehghani; Helmholtz-Type Regularization Method for Permittivity Reconstruction Using Experimental Phantom Data of Electrical Capacitance Tomography; IEEE TRANSACTIONS ON INSTRUMENTATION AND MEASUREMENT, VOL. 59, NO. 1, January 2010), Alme et al. (Kjell Joar Alme, Saba Mylvaganam, Electrical Capacitance Tomography, Sensor Models, Design, Simulations, and Experimental Verification, IEEE SENSORS JOURNAL, VOL. 6, NO. 5, October 2006), Warsito et al. (Warsito Warsito, Qussai Marashdeh, Liang-Shih Fan, Electrical Capacitance Volume Tomography IEEE SENSORS JOURNAL, VOL. 7, NO. 4, April 2007) and Cao et al. (Zhang Cao, Lijun Xu, Wenru Fan, Huaxiang Wang, Electrical Capacitance Tomography for Sensors of Square Cross Sections Using Calderon's Method, IEEE TRANSACTIONS ON INSTRUMENTATION AND MEASUREMENT, VOL. 60, NO. 3, March 2011). A major issue with such capacitive sensors is that the electric field inside the sensor between pairs of electrodes is neither uniform nor 1-dimensional, leading to a nonlinear relationship between the measured capacitance and medium permittivity distribution. A typical electric field developed in such sensors can be obtained using computational simulation and is depicted in Figure 3. This field was created within a homogeneous medium (imaging area) which

has uniformly distributed permittivity (ε) values of 1. Inhomogeneous media is expected to create a more complex electric field. As the electric field in these sensors is dependent on the permittivity distribution, it is not possible to derive an explicit expression which relates permittivity distribution to the measured capacitance. As such, previous studies have developed complex iterative inverse finite-element solutions to reconstruct the medium's permittivity using measured sensor's capacitance data. Apart from high computer power and time demand, such solutions suffer from serious ill-conditioning and uniqueness issues.

XLIV. In contrast to prior art capacitive sensors, the capacitive sensor shown in Figure 1 produces a sufficiently uniform electric field within the medium (e.g. tissue) to facilitate straight forward image reconstruction using linear equations, such as linear back projection. While electrical permittivity (EP) is an intrinsic property of a material, the electric field is a function of the geometry and permittivity distribution of the object being imaged and the sensor's configuration and excitation scheme. The latter two can be designed in order to achieve a linear electric field.

XLV. Figure 4 shows the capacitive sensor from Figure 1 incorporated within a computer implemented imaging system. The sensor, consistent with Figure 1, comprises two parallel plates housing opposing excitation cells and detector cells. The imaging system includes the parallel plate capacitive sensor, multiplexers, analog board, data acquisition system (DAQ), microcontroller, data bus, address bus, computer interface and a computer. The microcontroller controls the performance of the whole system by providing proper addresses and control commands to the DAQ system and multiplexers via the address and data buses. It also communicates with the DAQ system via these buses to receive the A/D convergence data [elaborate on generation of A/D convergence data?]. After reading the convergence data from the DAQ system, the microcontroller sends this information to the computer via a serial interface. The convergence data can then be processed using an image reconstruction computer code [Confirm whether this computer code can easily be varied/substituted for the different imaging techniques shown in the new manuscript?] , leading to the image. In order to switch the electronic relays inside the multiplexers, the microcontroller changes the address from 0 to n-1 on the address bus.

XLVI. One option for an excitation/data acquisition scheme is that each pair of excitation cell and a corresponding opposite detector cell (e.g. C1 and C'1) is switched on and then off one at a time such that the linear cell array is excited and data acquired sequentially. Alternatively, the excitation/data acquisition scheme can involve simultaneous excitation and data acquisition from a plurality of pairs of opposing excitation cells and detector cells. Activation of cells can be accomplished through a number of multiplexers which are connected to each cell on the sensor plates. A multiplexer is an electronic chip which consists of one output and multiple input pins. The input pins are connected or disconnected from the output pin via internal electronic switches (relays). Multiplexers are significantly faster and produce less noise in comparison with electromechanical or mechanical switches. A single pass of the sequential or simultaneous excitation/data acquisition yields a projection corresponding to one angle. The sensor can be rotated incrementally to acquire sufficient data projections necessary for image reconstruction. [Is this rotation needed with impedance phase angle imaging?]

XLVII. In silico phantom studies were conducted using an alternative parallel plate capacitive sensor configuration comprising two parallel brass plates, each plate comprising a diaphragm, which can be opened and shut, on each plate side, the diaphragms maintained in opposing alignment. The opposing diaphragms are a functional equivalent of the opposing

excitation cell and detector cell pairing. Movement of the diaphragms is coordinated so that the diaphragms are always maintained in opposing alignment and are synchronized to either be both open or both closed. In order to achieve an approximately linear relationship necessary for efficient EC reconstruction, a two-stage measurement scheme is executed. At each position along the diaphragm's motion direction, two capacitance measurements are conducted in sequence while the diaphragm is shut and then open. This pair of measurements is repeated at pixel size intervals until an object's field of view (FOV) is swept. EP of each pixel can be obtained easily using the corresponding EC value of the pixel and Equation 2.

XLVIII. Discretization and EC Image Reconstruction with the diaphragm variant capacitive sensor: Figure 5 shows a schematic of two different tissue mimicking materials (e.g. background tissue and tumor) placed inside a parallel plate capacitive sensor. The medium is discretized into small pixels with the size of the diaphragm hole using the shown grid. A medium column bridging the diaphragm holes consisting of pixel array labelled by C1, C2, C3, …, Cn is also shown. These C parameters represent the capacitance of material portion enclosed by a pixel which can be considered as a small capacitor. If the dimension of each pixel between the sensor's plates is assumed to be small enough, the permittivity and electric field within each pixel can be considered to be uniform while its direction is along the column's axis. Therefore, for each pixel Equation 1 can be approximated as follows:

XLIX. $$C = \varepsilon A/L \quad (2)$$

L. where C, ε, A and L are the pixel's capacitance, permittivity, surface area and size, respectively.

LI. Given the approximately 1D uniform electric field directed perpendicular to the plates' plane, pixels along each column can be approximated as series capacitors. As such, the relationship between the measured ΔC (i.e. capacitance difference between closed and open diaphragm states) and these elements is:

LII. $$\frac{1}{\Delta C} = \frac{1}{C_1} + \frac{1}{C_2} + \cdots + \frac{1}{C_n} = \frac{L_1}{\varepsilon_1 A_1} + \frac{L_2}{\varepsilon_2 A_2} + \cdots + \frac{L_n}{\varepsilon_n A_n}$$

LIII. Assuming a uniform grid, this relationship can be simplified to the following:

LIV. $$\frac{1}{\Delta C} = \frac{L}{A} \sum_{i=1}^{n} \frac{1}{\varepsilon_i} \quad (3)$$

LV. This is a linear relationship between the reciprocals of the measured data and tissue permittivity. In principle, the plates can be rotated around the object to acquire data pertaining to a number of projections sufficient for image reconstruction using linear back projection.

LVI. *In silico* Phantom Study for Linearity Assessment with Different Frequencies: to assess the effect of voltage source frequency in the diaphragm variant imaging system and determine the range of frequencies where the linear relationship given in Equation 3 is still valid, an *in silico* phantom study was carried out on two sets of phantoms. The first set involved three phantoms consisting of 60mm×100mm×60mm block simulating background tissue with 10mm, 15mm and 25mm diameter spherical inclusions, respectively. To mimic soft tissue stiffening resulting from cancer (e.g. breast cancer), the permittivity of inclusions for each frequency was assumed to be 3 times larger than the permittivity of the background tissue. The second set involved three phantoms consisting of 60mm×100mm×60mm block simulating background tissue with 15mm, 20mm and 25mm diameter spherical inclusions, respectively. In this set of phantoms, the permittivity of inclusion for each frequency was assumed to be 20 times lower than the permittivity of the background tissue to mimic bone inside muscle tissue. Each of these phantoms was assumed to be placed between the two parallel plates of the sensor such that the two diaphragms were aligned with the inclusion's centre during data acquisition. A square-

shaped excitation voltage with 5v amplitude and frequencies varying from 10 kHz to 10 GHz was applied to the sensor. A finite-element mesh consisting of ~2.2 million 8-noded hexahedral elements was used for discretizing each phantom. The phantoms were analyzed under varying frequencies and corresponding electric fields were calculated using CST Studio Suite (Computer Simulation Technology AG, Darmstadt, Germany). Using this solver ΔC between the two diaphragm points arising from shutting and opening the diaphragm were also calculated and compared to the corresponding value obtained from Equation 3.

LVII. *In silico* Phantom Study for Linearity Assessment with Different Diaphragm Locations: to assess the validity of the linear approximation presented in Equation 3 along the plates' long axis (X direction), an *in silico* breast phantom study involving three phantoms was carried out. Each phantom consists of a 60mm×100mm×10mm block simulating background mimicking healthy fibroglandular tissue. To evaluate inclusion size in this study, cylindrical inclusions of 15mm, 20mm and 25mm in diameter were included in the phantoms to mimic breast tumors. The permittivity of inclusion for each phantom was assumed to be 3 times larger than the permittivity of the background tissue. Each of these phantoms was assumed to be placed between the two parallel plates of the sensor and the two diaphragms were moved along the X axis from -30mm to 30mm with 3mm increments during data acquisition. The sensor's diaphragms' diameter was assumed to be 2 mm. A square-shaped excitation voltage with 5v amplitude and 32 KHz frequency was applied to the sensor. In each step along the X axis, the capacitance of the sensor in the model with open and closed diaphragms was measured, and the deviation from Equation 3 linear approximation was calculated. Each phantom was discretized using ~ 2.2 million 8-noded hexahedral elements to obtain its respective FE model which was solved using CST Studio Suite (Computer Simulation Technology AG, Darmstadt, Germany) to obtain ΔC at each diaphragm location. These values were compared to values obtained from Equation 3.

LVIII. Image Reconstruction of a Phantom Using *in silico* Data: an *in silico* phantom study was conducted to investigate the quality of reconstructed permittivity images expected from the diaphragm variant capacitive sensor in conjunction with the linear back projection algorithm. In this study three thin block 60 mm × 60 mm × 20 mm phantoms with round inclusions of 15mm, 20mm and 25mm in diameter were used as illustrated in Figure 6. The phantom was assumed to consist of tissues with permittivity values of 858 F/m and 2574 F/m for the background and inclusion, respectively. In order to generate capacitance data required for the permittivity image reconstruction, each phantom was discretized using 8-noded hexahedral elements. To ensure high accuracy, a fine mesh consisting of 1.2 million elements was used for modelling. Using CST Studio Suite (Computer Simulation Technology AG, Darmstadt, Germany), the phantom and capacitive sensor were modeled and the electric field resulting from an excitation voltage source with amplitude of 5v and 32 kHz frequency was calculated. Using the obtained electric field in conjunction with the permittivity distribution, the sensor's capacitance was calculated. This calculation was performed with open and closed diaphragms with varying position ranging from -30mm ≤ x ≤ 30mm along the plates. To obtain sufficient data necessary for image reconstruction using parallel beam projection algorithm, capacitance data were similarly obtained after rotating the two plates and once again varying the diaphragms position along the plates from -30mm to 30mm. This was performed along angles ranging from 0 to 180 degrees with 5 degree increments. Data obtained from this simulation was fed into a Linear Back Projection image reconstruction algorithm and a tomography permittivity image was reconstructed for each phantom.

LIX. Tissue Mimicking Phantom Study: a study involving the tissue mimicking phantom shown in Figure 7 was conducted. This phantom consists of a background and an inclusion constructed from gelatin, agar and salt. Dimensions of the background and inclusion are 100mm × 100mm × 90mm and 50mm × 50mm × 25mm, respectively. Permittivity values of the background and inclusion tissues were measured at 180 F/m and 420 F/m at 32 KHz, respectively. Each of these values was obtained by placing a small block shape representative sample of the material inside the capacitive sensor and measuring the resultant capacitance value. Each permittivity value was then calculated using a 1-D minimization algorithm where the sample's finite-element model was used to calculate resultant capacitance corresponding to given permittivity value. This algorithm alters the permittivity of the sample's FE model systematically until the calculated capacitance matches the experimentally measured counterpart sufficiently closely. To construct the phantom, gelatin, agar and salt with various concentrations were used. For the background, 15% concentration of gelatin in distilled water was used while for the inclusion construction 15% gelatin and 1% agar in addition to 3% salt were used. The experimental setup consists of a data acquisition system with capability of measuring capacitance values as low as 10^{-18} F. The diameter of the diaphragms was 1.5mm. The diaphragms on the sensor's plates were moved along X-axis from -50mm to +50mm with 5mm increments. The data acquisition system was connected to the sensor's plates and continuously measured the sensor's capacitance at 32 KHz with open and closed diaphragms along this motion range. The excitation voltage of the sensor was set to 5V.

LX. Results of *in silico* Phantom Study for Linearity Assessment with Different Frequencies: simulation results of the phantom study for frequency dependence assessment are illustrated in Figures 8 and 9. Figures 8 and 9 summarize the percentage error between theoretical ΔC obtained from CST studio and corresponding values obtained from Equation 3 for various frequencies. For all of the phantoms, at low frequencies (e.g. 100 KHz or lower) the electrical behavior of the capacitive sensor becomes very close to linear. The maximum error occurs for the phantom with the 25 diameter inclusion. In this case, the maximum error with the inclusion with higher permittivity is ~7% as shown in Figure 8. This error is only ~0.5% for the phantom where the inclusion has significantly lower permittivity in comparison to the background tissue as shown in Figure 9 at frequencies lower than 100 KHz. This implies that at low frequencies, the electrical behaviour of the capacitive sensor is such that the discretization where the tissue enclosed in columns bridging the two diaphragm points is approximated by series capacitors with a capacitance value of $C_i = \varepsilon_i A_i/L_i$, (see Equation 2) is a reasonably good approximation.

LXI. Results of *in silico* Phantom Study for Linearity Assessment with Different Diaphragm Locations: simulation results of a phantom study for diaphragm location assessment along the longitudinal axis (diaphragm's motion axis) of the sensor plates is illustrated in Figure 10. Figure 10 shows ΔC errors corresponding to deviation of the linear model from the numerical FE model of the phantoms used for linearity assessment with different diaphragm locations. These errors were obtained from simulation with an excitation voltage of 5v amplitude and 32 kHz frequency with various diaphragm locations along the X axis. This figure shows that the errors increase sharply while approaching the inclusions' periphery and it remains almost constant outside the inclusions' width. As expected, the maximum errors correspond to the largest inclusion of 25 mm where the maximum errors within the inclusion and near its periphery are 3.7% and 14.8%, respectively.

LXII. Results of Image Reconstruction of a Phantom Using *in silico* Data: Figure 11 shows reconstructed permittivity images of the three tissue mimicking phantoms shown in Figure 6. These images indicate that an artifact known as smoothing (blurring) effect are present around the inclusions in the reconstructed images. In order to mitigate this problem and reduce the smoothing effect, the images were segmented using thresholding technique. For this purpose different permittivity threshold values ranging from 2000 F/m to 2800 F/m were chosen to assess the sensitivity of resulting inclusion size with the threshold value. Segmented images obtained with threshold value of 2000 F/m are illustrated in the bottom row of Figure 11. Segmentation results with the different threshold values indicate that the size of inclusions change by up to 5%, implying that the accuracy of inclusion geometry obtained by segmentation is not very sensitive to the threshold's value.

LXIII. Results of Tissue Mimicking Phantom Study: Figure 12 illustrates the acquired capacitance projection along the X axis. The amplitude of projection graph significantly rises as it reaches the inclusion and falls back to its initial value as it passes the inclusion which implies that the experimental setup was able to accurately detect the inclusion.

LXIV. Linearity Deviation Metric with Simultaneous Firing of Cells of the Capacitive Sensor variant shown in Figure 1: an *in silico* phantom study involving a block shaped phantom with a 10 mm inclusion was conducted to assess deviation from the 1D linearity assumption as a function of permittivity and plate separation. Permittivity values ranging from 10^2 F/m to 10^6 F/m consistent with the range of biological tissue permittivity were used for the background while 3 times greater permittivity values were used for the inclusion. Note that plate separation represents the breast's thickness after being held between the two plates of the capacitive sensor. This parameter was varied between 80 mm to 120 mm. Deviation from the 1D linearity assumption was characterized using the metric $\Delta c = 100*|(C_{FEM} - C_L/ C_{FEM}|$ where C_{FEM} and C_L are the capacitance between a cell pair using the FEM method taken as ground truth and using the analytical formula used to calculate capacitance of capacitors connected in series, respectively. Average and maximum values of this deviation metric are shown in Figures 13A and 13B, respectively, as functions of tissue permittivity and plate separation. Figures 13A and 13B indicate that there is very little variation of the deviation metric with respect to permittivity values for biological tissues while the maximum deviation from uniform 1D electric field is only 8%.

LXV. In a second set of experimental examples the capacitive sensor is used to determine phase angle of impedance measurements of a sample held between the two parallel plates and process the phase angle data to generate an image of the sample.

LXVI. Electrical impedance (EI) imaging modalities can address shortcomings of other medical imaging modalities currently used in medical imaging including, for example, cancer screening/imaging applications, such as X-ray, CT, ultrasound or MRI techniques. EI modalities use low energy electric field to probe and characterize electrical impedance of biological tissues. The use of non-ionizing electric field as well as the simplicity and low cost of these imaging modalities make them ideal for tumour screening/imaging including, for example, breast cancer screening. With regard to breast cancer screening/imaging EI modalities can include Electrical impedance tomography (EIT) and electrical impedance mammography (EIM). EIT and EIM produce images that display the distribution of tissue electrical impedance (electrical conductivity and electrical permittivity). Studies aimed at characterizing the electrical properties of normal and pathological tissue have shown that electrical conductivity and electrical

permittivity of breast malignancies are significantly higher than those of benign and normal breast tissues

LXVII. Despite recognized advantages of EI imaging, only a few studies have used EIM for breast cancer detection. Among them, Assenheimer et al. (Michel Assenheimer, Orah Laver-Moskovitz, Dov Malonek, David Manor, Udi Nahaliel, Ron Nitzan, Abraham Saad, The T-SCANTM technology: electrical impedance as a diagnostic tool for breast cancer detection, Physiol. Meas., Vol. 22(1), Feb 2001, 1-8) demonstrated that current EIM technologies such as TransScan 2000 (Siemens Medical, Germany, and TransScan, Ramsey, NJ, USA), are only capable of detecting high impedance inclusions located close to the breast surface. This research introduces a novel EIM technique which uses an electrical impedance imaging system consisting of a parallel plate sensor. This investigation involves in silico and tissue mimicking phantom studies conducted to demonstrate its application for medical diagnosis including, for example, breast cancer screening.

LXVIII. The electromagnetic field generated by applying current density to a body surface is governed by Maxwell's equations. For a nonmagnetic material such as biological tissues, the general form of Maxwell's equations in the time domain with the inclusion of displacement current and continuity equation is as follows:

$$\frac{\partial \rho(r,\ t)}{\partial t} + \nabla \cdot \mathbf{J}(r, t) = \sigma \qquad (4)$$

$$\nabla \cdot \mathbf{D}(r, t) = \rho(r,\ t) \qquad (5)$$

$$\nabla \times \mathbf{H}(r, t) = \mathbf{J}(r, t) + \frac{\partial \mathbf{D}(r,t)}{\partial t} = \sigma E(r, t) + \mathbf{J_e}(r, t) + \frac{\partial \mathbf{D}(r,t)}{\partial t} \qquad (6)$$

$$\nabla \cdot \mathbf{B}(r, t) = 0 \qquad (7)$$

$$\nabla \times \mathbf{E}(r, t) = -\frac{\partial \mathbf{B}(r,t)}{\partial t} \qquad (8)$$

LXIX. where ρ(r,t) is the electric charge density, J is the electric current density, E is the electric field, D = εE is the electric displacement current, ε is the electric permittivity, B is the magnetic field, H = B/μ is the magnetic intensity and μ is the magnetic permeability which is considered to be the same as the permeability of vacuum for biological tissues. In this study, the external magnetic field is assumed to be negligible (B = 0). A further assumption is that impedance measurement is performed at low frequencies (1MHz or lower) where the frequency of the voltage source is low enough for the EM propagation delay to be neglected. Using the phasor format of Equations 4 to 8 and dropping the time harmonic, leads to the following equations in the frequency domain. This was performed to facilitate the equations' computational solution consistent with the COMSOL Multiphysics software package (COMSOL, Inc., MA, USA) used in this second set of experiments.

$$\nabla \cdot \mathbf{J}(r, \omega) = \mathbf{Q}_j(r, \omega) \qquad (9)$$

$$\mathbf{J}(r, \omega) = \sigma\mathbf{E}(r, \omega) + j\omega\mathbf{D}(r, \omega) + \mathbf{J}_e(r, \omega) \qquad (10)$$

$$\mathbf{E}(r, \omega) = -\nabla\mathbf{V}(r, \omega) \qquad (11)$$

LXX. where Q_j represents current source, σ is tissue electrical conductivity, ω is the natural frequency, J_e is an externally induced current density and V is the electric potential. COMSOL finite element method (FEM) can be used to solve Equations 9 to 11 to obtain the impedance amplitude and phase angle in the breast models involved in this second set of experiments.

LXXI. Similar to x-ray mammography where the breast is placed in a parallel-plate compression unit and projections of x-ray are measured and converted into mammograms, in the EIM technique for this second set of experiments, the breast is gently compressed between the two parallel plates of an impedance sensor. While the breast is gently compressed, the electrical impedance its tissue is measured as projection data before they are converted into a mammogram. Depending on the excitation frequency [Can this excitation frequency dependency be further delineated? What is this dependency? Explicit frequency ranges?] in the proposed technique, different types of image reconstruction methods such as image impedance, resistance, capacitance and phase angle may be employed to generate respective images. While imaging impedance and resistance are feasible at all excitation frequencies, for the capacitance and phase angle imaging, choosing the right excitation frequency is critical [How critical? Is this 'critical' a different way of stating frequencies less than 1 KHz are preferred? – or more generally that lower frequencies (eg., less than 5 KHz are preferred?].

LXXII. In order to study the electrical behaviour of a biological tissue, a proper electrical model is useful. A lumped electric model (equivalent circuit) of a tissue part of the breast located between two electrodes of the two parallel plates at low frequencies is shown in Figure 16. It consists of a parallel resistor and capacitor.

LXXIII. It is noteworthy that this electrical model of biological tissues, which is used extensively in the literature, has an additional series resistor [Is this series resistor in addition to the parallel resistor shown? is this series resistor not shown?] with capacitance C_s. However, at low frequencies, the value of this resistor, which represents the resistance of intracellular fluids, becomes negligible. The relationship between electrical impedance, resistance, capacitance, and phase angle of a biological tissue sample derived from its equivalent circuit, is:

$$Z_s \angle\theta_s = [(R_s/\omega C_s) / (R_s^2 + (1/\omega C_s)^2)^{1/2}] \angle -90^o + \mathrm{Arctg}\,(1/R_s C_s \omega) \qquad (12)$$

LXXIV. where Z_s and θ_s are the measured amplitude and phase angle of the tissue's electrical impedance, ω is the natural frequency of the excitation signal, and R_s and C_s are the tissue's electrical resistance and capacitance, respectively.

LXXV. In order to examine how the impedance components of a typical biological tissue (e.g. adipose) changes with frequency, a computational simulation was performed involving an adipose tissue specimen. An electrical model of a 50mm×50mm×50mm block-shaped adipose tissue specimen was constructed, and its electrical impedance (Zs ∠θs) was measured at frequencies of 10 Hz to 1 MHz via simulation using COMSOL. The electrical conductivity and permittivity of the tissue specimen at these frequencies, which were input to reconstruct the model, were obtained from the literature (C Gabriel, S Gabriel and E Corthout, The dielectric properties of biological tissues: I. Literature survey, Phys. Med. Biol. 41 (1996) 2231–2249; S Gabriel, R W Lau and C Gabriel, The dielectric properties of biological tissues: II. Measurements in the frequency range 10 Hz to 20 GHz, Phys. Med. Biol. 41 (1996) 2251–2269). The measurement was conducted using two different configurations, leading to two corresponding finite element (FE) models. In one configuration the specimen was assumed to be

placed between two cylindrical brass electrodes with a radius of 1.5 mm and height of 2mm. In the other configuration, the specimen was assumed to be held between the parallel plates of an imaging sensor of a type shown in Figure 1. Each of these models consisted of ~2.2 tetrahedral finite elements.

LXXVI. Using COMSOL solver in conjunction with Equation 12, the capacitance and resistance data of the adipose tissue specimen at the 10 Hz-1 MHz frequency range were obtained for each configuration. These data, which are illustrated in Figure 17, show that at frequencies higher than 1 kHz, the adipose tissue capacitance component diminishes, hence the tissue's impedance becomes predominantly resistive at such frequencies. This implies that the reconstruction of capacitance, permittivity and phase angle images that involve the capacitive component of the tissue's impedance are advantageously generated at excitation frequencies lower than 1 kHz. Based on these observations, the following three types of image reconstruction can be derived.

LXXVII. First type of image reconstruction: Electrical Resistivity and Conductivity Image Reconstructions in EIT and EIM. Electrical conductivity image reconstruction is the easiest and most common type of electrical impedance image reconstruction. This method has been used in the majority of EIT (electrical impedance tomography) applications in the past three decades. The following equation shows the fundamental relationship between tissue electrical resistivity and its conductivity,

$$R = \frac{V}{I} = \frac{\int E.\ dl}{\oint \sigma E.\ ds} \qquad (13)$$

LXXVIII. where R is the tissue electrical resistance, V is the potential difference between the two electrodes where the voltage is being measured, I is the electric current, E is the electric field and σ is the tissue electrical conductivity. In the context of breast imaging, electrical resistance and electrical conductivity image reconstruction may be performed in the whole frequency range of 10Hz-1MHz, as according to Figure 17 the measured resistance at this frequency range is appreciably high. As such, in the majority of EIT image reconstruction methods which mainly use frequencies higher than 1 kHz, the measured amplitude of tissue's impedance is simply approximated by its electrical resistance. However, the major problem with conductivity image reconstruction stems from the complex relationship between R and σ and its high sensitivity to the electric field. Consequently, this type of image reconstruction leads to an ill-posed problem, which requires iterative and non-linear image reconstruction algorithms. Furthermore, previous studies have shown that the variation range of conductivities for biological tissues at 10 Hz-20 GHz is limited. This implies that conductivity and resistance imaging of biological tissues may not produce images with high contrast.

LXXIX. The following equation, which is derived from the lumped electrical model of the tissue (parallel capacitor and resistor in Figure 16), shows the relationship between the tissue resistance (Rs), their electrical impedance (Zs) and phase angle (θs).

$$R_s = \frac{Z_s\ \mathrm{tg}(90+\theta_s)}{\sqrt{(1+\mathrm{tg}^2(90+\theta_s)}} \qquad (14)$$

LXXX. In EIM, resistance image reconstruction involves obtaining resistance projection data for each point on the breast surface plane, and converting this data into 2D mammograms. As such, the breast tissue's impedance projections on the breast surface plane was measured using the type of sensor shown in Figure 1. Then by using Equation (14), the resistance projection data of the breast tissue was calculated and converted into 2D resistance

mammograms. As solving Equation 13 for σ is not convenient, to obtain an estimate of the breast tissue's conductivity projection on the breast surface plane, an assumption of uniform electric field leading to the inverted resistance image can be used.

LXXXI. Second type of image reconstruction: Electrical Permittivity and Capacitance Image Reconstructions. Electrical permittivity is an intrinsic property of materials, which may be obtained via the material's electrical capacitance. For measuring tissue electrical capacitance, the amplitude and phase angle of the tissue's impedance must be measured. The following equation shows the relationship between the tissue capacitance (Cs), their electrical impedance (Zs) and phase angle (θs) based on the lumped electrical model shown in Figure 16.

$$C_s = \frac{1}{Z_s\,\omega\,\sqrt{(1+\mathrm{tg}^2(90+\theta_s)}} \qquad (15)$$

LXXXII. According to Figure 17, for a breast adipose tissue specimen placed between two electrodes, measuring the capacitance (Cs) and phase angle (θs) at frequencies higher than 1kHz may not be feasible, as the tissue capacitance becomes too small to be reliably measured. As such, for breast imaging, capacitance, permittivity and phase angle image reconstructions performed at high frequencies (eg., greater than 5 KHz) are of reduced reliability. However, at lower frequencies (e.g. 1 KHz or lower) where the electrical capacitance is sufficiently large, a reliable measurement of Cs is feasible.

LXXXIII. Measurement of tissue electrical permittivity (ε) can be achieved by measuring its electrical capacitance (C_s) as direct measurement of permittivity is not feasible. The following equation shows the fundamental relationship between electrical capacitance (C) and electrical permittivity (ε):

$$C = \frac{Q}{V} = \frac{\oint \varepsilon E.\ ds}{\int E.\ dl} \qquad (16)$$

LXXXIV. where Q represents the electric charge, V is the potential difference between the two electrodes where the measurement is performed, E is the electric field and ε is the tissue electrical permittivity. This equation shows that the relationship between C and ε is complex and highly dependent on the electric field. As such, tissue permittivity image reconstruction may also lead to ill-posed problems that require iterative and non-linear inverse problem solution algorithms. However, as the variation range of permittivity of biological tissues is very broad in comparison with that of conductivity, permittivity and capacitance imaging is expected to produce images with higher contrast; hence they are preferable over resistance and conductivity imaging.

LXXXV. In EIM, capacitance image reconstruction involves obtaining capacitance projection data for each point on the breast surface plane followed by converting the data into 2D capacitance mammograms. In this study we measured the capacitance projections of the breast models on their surface plane using the type of sensor shown in Figure 1. Using Equation 15, the capacitance projection data of the breast tissue was calculated from the impedance data before they were converted into 2D capacitance mammograms. As solving Equation 16 for ε is not feasible, to obtain an estimate of the breast tissue's permittivity projection on the breast surface plane, the capacitance image can be used as capacitance and permittivity are approximately proportional.

LXXXVI. Third type of image reconstruction: Phase Angle Image Reconstruction. Impedance phase angle of a tissue (θs) may be obtained from Equation 12, leading to the following equation:

$\theta_s = -90^o + \text{Arctg}\,(1/R_s C_s \omega)$ (17)

LXXXVII. Using the discrete form of Equations 10 and 13 leads to:

$$\frac{1}{R_s C_s\,\omega} = \frac{\sum_{i=1}^{m} \sigma_i\, E_i\,.\,\Delta S_i}{\omega \sum_{i=1}^{m} E_i\,.\,\Delta L_i} \times \frac{\sum_{i=1}^{m} E_i\,.\,\Delta L_i}{\sum_{i=1}^{m} \varepsilon_i\, E_i\,.\,\Delta S_i} \qquad (18)$$

Assuming equal ΔS_i and ΔL_i spacing within each element where tissue homogeneity is a good approximation, this relationship may be simplified to the following:

$$\frac{1}{R_s C_s\,\omega} = \frac{\sigma}{\varepsilon\,\omega} \qquad (19)$$

LXXXVIII. Substituting the above in Equation 18 leads to:

$\theta_s = -90^o + \text{Arctg}\,(\frac{\sigma}{\varepsilon\,\omega})$ (20)

LXXXIX. This equation shows that, unlike resistance and capacitance that depend on the electric field and element geometry in addition to the tissue intrinsic properties, the impedance phase angle is dependent on the intrinsic electrical properties of the tissue only. As such, phase angle images are expected to be of higher quality compared to resistance and capacitance images. Moreover, phase angle imaging of the breast is feasible at lower frequencies (e.g. <1 kHz) only where the capacitance component of the measured impedance is non-zero.

XC. Configuration of an Electrical Impedance Mammography System. An electrical impedance mammography scanner was constructed. It comprises two parallel plates where the breast is placed in between before image acquisition is performed. One plate is used for excitation while the other is a detector plate. The excitation plate includes the excitation board while the detector plate is a hand-held plate which can include a detector board and analog and digital boards. The excitation board comprises a large conductive plate and an electronic board on the back, which generates the excitation sinusoidal signals with selectable frequency at 5 Vp-p . The detector board consists of a 1-D circular cells array moved at 5 mm increments along the top surface of the breast to scan its entire volume. The 1-D array consists of thirty circular cells. The radius of each cell is 1.5 mm; each one is separated from the next by a gap of 0.125 mm on the printed circuit board (PCB). For data acquisition, the breast was squeezed gently between the detector plate and the excitation plate. The impedance signals, which were obtained from the cells of the 1-D array, were first amplified by the analog circuit board before they were sent to the digital circuit board. The digital circuit board consists of multiple 24 bit analog to digital converters (AD7766, Analog Devices, Massachusetts, USA) and a microcontroller (ATmega320, Atmel, California, USA). AD7766 converts the analog impedance signal into 24 bits digital packets and sends them through the USB port to a computer. A Matlab (MathWorks, Massachusetts, USA) code on the computer side, which is connected to the sensor (more specifically , the microcontroller) through the USB port, receives the digital impedance data and converts them into 2D digital images. The microcontrollers on the digital board of the sensor [Which of “scanner” or “sensor” is more appropriate? - “scanner” is used in the new manuscript, whereas “sensor” is used in US provisional?] does all the coordination between the A/D converter and computer. The whole procedure can be completed in less than 10 seconds.

XCI. A schematic of the sensor in this second set of experiments is illustrated in Figure 18. Each conductive cell on the detector board is connected to an impedance measurement circuit that measures the impedance amplitude and phase angle of the adjacent breast tissue with 0.1Ω and 0.01° accuracy, respectively.

XCII. The tissue's impedance components (the tissue's resistance and capacitance) measured by the sensor, can be described theoretically by Equations 13 and 16. As these equations show, the measured tissue's resistance (R) and capacitance (C) are highly dependant on the electric field (E) inside the tissue between the parallel plates, the contact area of each conductive cell (A), separation between the sensor plates (L) and dielectric property of the tissue (σ and ε). If the electric field between the sensor plates was uniform, the Equations 13 and 16 could be simplified to $\mathrm{R} = \frac{L}{\sigma A}$ and $\mathrm{C} = \frac{\varepsilon\,\mathrm{A}}{\mathrm{L}}$, respectively. This implies if E was uniform, for a constant A and L, the measured tissue's resistance and capacitance would be functions of tissue dielectric properties, σ and ε only.

XCIII. Methods of *in silico* Breast Phantom Experiment. To assess the capability of the sensor for breast cancer detection, and to evaluate the three types of image reconstruction (ie., conductance, permittivity and phase angle imaging) a series of computer simulations were carried out on a phantom following the configuration shown in Figure 19. The simulations were carried out using the COMSOL Multiphysics software package. The phantom mimics a breast gently compressed by two plates, hence it consists of a half-cylinder with a radius of 75 mm and height of 50 mm. It embeds a cylindrical inclusion with a radius and thickness of 10mm and 20mm, respectively. In order to increase the simulation's realism, the inclusion was positioned as illustrated in Figure 19 in order to mimic the upper outer quadrant where the majority of breast cancer tumors are found. The location of the inclusion along the height of the cylindrical phantom was set to be variable such that the inclusion's centre was located at the centres of the bottom, middle and top thirds along the height. The permittivity and conductivity values assigned to the breast model were chosen based on values reported in the literature for breast tissue at 0.5 kHz. The inclusion's permittivity and conductivity values were assumed to be 6 and 8 times higher than normal breast tissue's conductivity and permittivity, respectively. The breast phantom's FE mesh, which is illustrated in Figure 18, consisted of ~2.7 million tetrahedral elements. Similar to the sensor, one conductive plate was modeled to touch the breast model from the bottom to provide an excitation signal, while the top plate (detector) was considered to measure the impedance. The detector plate consisted of 30 circular conductive cells, each with a radius of 1.5 mm and separation of 0.2 mm. The COMSOL solver used the FEM approach to numerically solve Maxwell's equations and compute the amplitude and phase angle of the electric current that passed through each detector cell. From these computations, the impedance values of the breast tissue located between each detector cell and excitation cell was acquired. To obtain the projected mammography image of the resistance and capacitance, the projection value for each cell was calculated using Equations 14 and 15.

XCIV. Methods for Tissue Mimicking Breast Phantom Experiment. A tissue mimicking phantom study was performed to assess the effectiveness of the three types of imaging techniques. A gelatine phantom was prepared following the general shape of the in silico phantom shown in Figure 19, the gelatine phantom comprising a half-cylinder background tissue embedding a cylindrical inclusion constructed of gelatin and common salt. The background half cylinder part was 150 mm in diameter and 50 mm in height while the diameter and height of the cylindrical inclusion were both 20 mm. Along the phantom's height, the inclusion was placed in the middle. The conductivity and permittivity of the background and inclusion tissues were

measured independently prior to image data acquisition. At 0.5 kHz, their conductivity were 0.23 S/m and 1.2 S/m while their relative permittivity were 1,084,454 and 8,546,138 for the background and inclusion, respectively. Each of these values were obtained by placing a small block shape representative sample between the two electrodes of the apparatus shown in Figure 16 followed by measuring the resultant resistance and capacitance values. The conductivity and permittivity values of each tissue were then calculated using a 2-D optimization algorithm where the sample's FE models were used to calculate the resultant resistance and capacitance values corresponding to the current estimates of conductivity and permittivity values in the optimization process. The algorithm altered the conductivity and permittivity of the sample's FE model systematically until the mismatch between the calculated and experimentally measured resistance and capacitance values was a minimum. To construct the phantom, gelatin and common salt with various concentrations were used. For the background, 12% concentration of gelatin in distilled water was used while for making the inclusion 12% of gelatin and 0.09% common salt was used. The experimental setup consisted of the data acquisition described above where an excitation voltage of the sensor was set to 5 Vp-p at 0.5 kHz.

XCV. Results of *in silico* Breast Phantom Experiment. Images reconstructed from the *in silico* breast phantom are shown in Figure 20. They show 2D mammography images obtained by projection of the impedance, resistance, capacitance, and phase angle [This appears to be four-types of images. How does this correlate to the three types of image reconstruction techniques? Resisatance, capacitance and phase angle are described above – is impedance technique described above? Is impedance technique based on impedance amplitude/magnitude?] of the breast phantom corresponding to three different tumor positions along its height (z-axis). The images were produced from raw simulation data with no additional filtering or manipulation. As described above, the permittivity images are similar to the capacitance images while the conductivity images are similar to inverted resistance images. Thus, the permittivity and conductivity images of the breast phantom are not shown. Variation profiles of the measured impedance, resistance, capacitance and phase angle of the *in silico* breast phantom along the section crossing the inclusion (shown in Figure 19B) are also illustrated in Figure 20. Due to symmetry, the reconstructed images of the phantom with the inclusion located at the centres of bottom and top thirds along the height of the phantom (rows 1, 2 and 5, 6) are identical. As expected, image contrast pertaining to these bottom third and top third locations is higher compared to the case where the inclusion is located in the middle of the phantom's height. This is particularly more important with the impedance and resistance images where the respective images can hardly detect the inclusion. Among the reconstructed images, the capacitance and phase angle images exhibited higher contrast and better quality compared to the impedance and resistance images.

XCVI. The results revealed that there are artifacts seen as intensity variations around the phantom and inclusion's periphery in the reconstructed impedance, resistance, and capacitance images. These artifacts were caused by the nonlinearity and non-uniformity of the electric field. This led to about 9% higher measured impedance and resistance, and about 10% lower measured capacitance around the peripheries as shown in the 2nd, 4th, and 6th rows of Figure 20.

XCVII. Results of Tissue Mimicking Breast Phantom Experiment. Reconstructed images obtained from the tissue mimicking breast phantom study are shown in Figure 21. Pixel size in these images is 3 mm×5 mm. Figure 21 demonstrates that the inclusion can be clearly distinguished from the background on the capacitance and phase angle images. Similar to the reconstructed images obtained from the *in silico* breast phantom study, the inclusion in the

impedance and resistance images of the gelatin phantom cannot be clearly differentiated from its background. The second row of Figure 21 illustrates the variation profiles of the impedance, resistance, capacitance, and phase angle signals along the section crossing the inclusion as shown in Figure 19B.

XCVIII. The *in silico* and tissue mimicking phantom studies indicated that, among the various tested imaging techniques, the permittivity, capacitance and phase angle images were shown to be more effective than the impedance, resistance and conductivity images. Moreover, the studies demonstrated that the phase angle image reconstruction was capable of producing the highest quality images consistent with Equation 20, which implied strict dependence on the tissue intrinsic properties.

XCIX. Experimental results described herein suggest that breast inclusions with higher dielectric values are highly detectable when they are located in the top outer quadrant of the breast. This may be highly advantageous for breast cancer detection, as previous research has shown that the majority of cancer tumors form in the top outer quadrant of breast. Higher conductivity and permittivity of an inclusion also leads to improved tumor detection characterized by higher image contrast. Results provided are conservative, as only conservative increases of 6 and 8 times higher values of conductivity and permittivity were assigned to the inclusion in the *in silico* and tissue mimicking phantom studies relative to background, compared to previous studies that have established the dielectric values of breast cancer tumors at 20-40-fold higher than those of normal breast tissue. Experimental results indicate that the projection images are able to properly capture the location of inclusions with higher dielectric parameter values. However, the size of the inclusion in these images increase with depth. For example, the inclusion in the image corresponding to the case where the inclusion is located in the breast's mid-height appears more diffused (3rd row of Figure 20), hence its sizes is overestimated in comparison with the images corresponding to cases where the inclusion is located in the top or bottom one-third heights. These size variations are due to the electric field non-uniformity. Results obtained from this investigation indicate that, among images produced by the various image reconstruction techniques, the phase angle image is superior in terms of cancer detectability. These results also suggest that the proposed EIM technique is capable of detecting inclusions located deep inside the breast while other EIM technologies such as TransScan are only capable of detecting inclusions located close to the breast surface.

C. The capacitive sensor described herein provides several advantages over existing technologies. The sensor can measure capacitance as low as Femtofarad. Using *in silico* phantom studies, it was shown that at low frequencies of 1 kHz to 10 kHz [This range was stated in the US provisional - Why is freq range stated as a 1 kHz lower limit? Is it that the diaphragm version has a lower limit of 1 kHz while the non-diaphragm version has a lower limit of approx.. 100 Hz?] the average error due to deviation from the linear equation approximation is reasonably low, especially at the centre of inclusion. As such, the sensor can operate at low frequencies within this range, leading to reasonably good quality images constructed using linear back projection. Figure 10, which was obtained from an *in silico* phantom study involving block shape phantoms with inclusions with various sizes, indicated that the maximum deviation from the linear equation approximation occurs at the periphery of the inclusions which suggests that the blurring artifact around the periphery of inclusions in the reconstructed images is caused by the mentioned approximation error. This artifact, which is also known as smoothing effect, is quite common in electrical properties imaging. Results indicate that the quality of images obtained by the capacitive sensor described herein is comparable or superior to those of prior art ECT and

EIT. Moreover, image reconstruction is carried out using straight forward linear back projection in contrast to nonlinear optimization techniques associated with prior art ECT and EIT techniques. As expected, a trade-off exists between the contrast and resolution of the capacitive sensor imaging system. In other words resolution and contrast of the imaging system is determined by the size of diaphragms/cells such that smaller diaphragms/cells produce smaller and narrower perturbation in the sensor's electric field and can produce images with high resolution and small dynamic range while large diaphragms/cells produce larger perturbation with higher SNR and high image dynamic range but with lower resolution. It was concluded from the results of the *in silico* and tissue-mimicking phantom studies that inclusions with both higher and smaller EP values compared to their surrounding tissues are highly detectable using the proposed method. Being safe and low-cost are two further advantages that the capacitive sensor offers. Results are encouraging and indicate that the capacitive sensor is capable of detecting tissue abnormalities effectively, rendering it a safe, effective and inexpensive tool for cancer screening applications. [Can this paragraph be adapted to include phase angle aspect and experiments?]

CI. Several illustrative variants have been described above. Further variants and modifications are described below. Moreover, guiding relationships for configuring variants and modifications are also described below. Still further variants and modifications are contemplated and will be recognized by the person of skill in the art. It is to be understood that guiding relationships and illustrative variants or modifications are provided for the purpose of enhancing the understanding of the person of skill in the art and are not intended as limiting statements.

CII. Frequency of the capacitive sensor electric field will typically range between 1Hz and 1MHz for medical applications. More specifically, for most medical imaging/screening applications the frequency will be less than 100KHz and may be optimized for a specific tissue type. In many examples of medical imaging/screening applications the frequency will range between 10 Hz and 10 KHz. In examples of medical imaging/screening applications for human breast tumors, the frequency will often be set in a range with a lower limit of 10 Hz and an upper limit that may be less than 5 KHz, less than 4 KHz, less 3 KHz, less than 2 KHz, less than 1 KHz or less than 0.5 KHz. In further examples of medical imaging/screening applications for human breast tumors, the frequency can be set in a range with a lower limit of about 100 Hz and an upper limit that may be less than 5 KHz, less than 4 KHz, less 3 KHz, less than 2 KHz, less than 1 KHz or less than 0.5 KHz.

CIII. Experiments indicate that both circular and non-circular (eg., square) shaped cells generate equally uniform 1D electric field. Thus, the shape of cells can be modified as desired.

CIV. Deviation of an electric field communicating between a paired excitation cell and detector cell from 1D linearity may be characterized using a deviation metric Δc. Typically, average deviation of the electric field from linearity will be less than 25%. For example, average deviation may be less than 20%, 15%, 10%, 5% or less than any percentage therebetween.

CV. The size of a cell typically ranges from 0.2 mm for high resolution imaging to 2 mm for low resolution imaging.

CVI. Distance between perimeters of neighboring cells is at least 0.05 mm, more typically at least 0.1 mm, generally ranging from about 0.1 mm to about 5 mm depending on requirements of a specific application. A minimum distance between perimeters of neighboring cells may be required to avoid significant disturbance of the 1D electric field uniformity. The minimum distance may vary depending on the manufacturing technique and process used to

construct the capacitive sensor plates. For example, in a printed circuit board (PCB) etching process, a cell is insulated from neighboring cells by a non-conductive gap of at least 0.1 mm.

CVII. The capacitive sensor has been described as comprising a single line array of paired excitation and detector cells. The capacitive sensor may readily be configured as a two-dimensional grid array of opposing paired excitation and detector cells.

CVIII. Each excitation cell may be surrounded by a guard. The guard is a conductive material that may be the same material as the cell. The guard is electrically isolated from the cell by a non-conductive gap or non-conductive material, with the cell positioned within a central opening or aperture of the guard. The shape of the guard may be varied as desired. Figure 14 shows a circular excitation cell surrounded by a guard of conductive rectangular area defining a central circular opening or aperture for capturing the circular excitation cell and its surrounding non-conductive material area. The guard is excited with the same frequency and phase as the cell. The purpose of the guard is to focus the electric field line between corresponding excitation and detector cell pair and to minimize its bending. Each guard is electrically isolated from neighboring guards and each detector cell is electrically isolated from neighboring detector cells. This isolation is generated through the printed circuit board (PCB) process using non-conductive material where the gap between neighboring cells or neighboring guards range from 0.1 mm to 0.2 mm.

CIX. Capacitive sensors may be driven by an excitation signal to fire individual cells sequentially or to fire a plurality of cells simultaneously. Sequential firing, in the absence of a guard, may reduce linearity but may achieve higher contrast. Thus, firing cells sequentially, in the absence of a guard, achieves better contrast but at the cost of solving nonlinear equations. Use of a guard may improve linearity for sequential firing. Furthermore, as shown in Figure 13A and 13B, simultaneous firing achieves good linearity.

CX. In the variant shown in Figure 14 the material used to make the guard and cell arrays are the same. The cells and guards are made/etched from a thin copper layer laminated on an insulator pad/substrate (the insulator may be a suitable type of glass epoxy). The guards and cells are separated by a thin non-conductive gap on the copper layer of PCB through an etching process. The area which is located at the center is the cell and the area which surrounds the cell is the guard. In other examples, the guard and the excitation cell may be made of different conductive materials.

CXI. Both the cell and its surrounding guard are excited at the same time (simultaneously), thus the emission/propagation of the electric field from the cell and guard is simultaneous. In certain examples, the guard may be excited in advance of the excitation cell.

CXII. Typically, the guard and the cell are excited with the same frequency and phase. Amplitude of an applied excitation signal can be different between the guard and the excitation cell and maybe optimized to achieve a more focused beam. For example, a higher electric potential can be applied to the guard compared to the excitation cell in order to further focus the beam emitted by the excitation cell.

CXIII. The purpose of the guard is to focus the electric field line between corresponding excitation and detection cell pair. Without wishing to be bound by theory, an electric field emitted from the guard may surround the electric field from the cell and constrain the electric field from the cell to a linear direction. Thus, the configuration of the guard may be modified to improve the 1D uniform electric field between an opposing excitation cell and detector cell pair.

CXIV. The capacitive sensor system may be used for medical screening or medical imaging. A simplified variant of the capacitive sensor system which does not require image

reconstruction can be used effectively for medical screening. This is possible by visualizing the projected capacitance data, for example capacitance data from a single pass of a linear cell array. For medical imaging, the capacitive sensor must be configured to capture sufficient data projections at different angles for image reconstruction.

CXV. Medical screening or medical imaging may be useful wherever existing imaging of tissues is performed, and may be particularly useful for tumour detection or imaging. For example, medical screening or medical imaging of a human female breast may be performed for detection of breast cancer.

CXVI. Medical imaging may be conducted for the purpose of image guided needle biopsy of a human female breast to accurately diagnose breast cancer. This is achieved by adding a grid with openings spaced in between excitation cells as illustrated in Figure 15. The openings slidably receive a needle of a needle biopsy device. The grid openings provide a template for guiding needle insertions while guidance is provided by electrical permittivity tomography imaging achieved using the capacitive sensor. This grid/template modification may also be used for insertions for therapeutic purposes.

CXVII. The capacitive sensor system may be used in conjunction with other imaging modalities such as x-ray, CT. and MRI as may benefit a specific application.

CXVIII. Embodiments described herein are intended for illustrative purposes without any intended loss of generality. Still further variants, modifications and combinations thereof are contemplated and will be recognized by the person of skill in the art. Accordingly, the foregoing detailed description is not intended to limit scope, applicability, or configuration of claimed subject matter.

WHAT IS CLAIMED IS:

1. An electrical permittivity tomography [electrical impedance imaging] sensor [or capacitive sensor], comprising:

a first planar plate comprising a plurality of excitation cells;

a second planar plate comprising a plurality of detector cells**;**

the first planar plate held in spaced parallel relation to the second planar plate and defining a chamber there between;

the first and second planar plates arranged to align each excitation cell with a corresponding detector cell in a one-to-one paired relationship; and

each paired excitation cell and detector cell configured for synchronized activation with a substantially uniform electric field communicating there between.

2. The sensor of claim 1, wherein each excitation cell and each detector cell is independently controlled by an electronic switch.

3. The sensor of claim 2, wherein a plurality of electronic switches are coordinated in a multiplexer.

4. The sensor of claim 3, wherein activation of the plurality of excitation cells is coordinated by a first multiplexer and activation of the plurality of detector cells is coordinated by a second multiplexer.

5. The sensor of claim 4, further comprising a voltage source in communication with an input of the first multiplexer, the voltage source generating an excitation signal.

6. The sensor of claim 5, wherein the excitation signal can be modulated for amplitude, frequency or both amplitude and frequency.

7. The sensor of claim 4, further comprising data acquisition circuitry in electrical communication with an output of the second multiplexer [, the data acquisition circuitry controlling measurement of an electrical property].

8. The sensor of claim 7, wherein the data acquisition circuitry measures capacitance [or impedance].

9. The sensor of claim 1, wherein each excitation cell is electrically isolated from neighboring excitation cells and each detector cell is electrically isolated from neighboring detector cells.

10. The sensor of claim 9, wherein the electrical isolation is a non-conductive insulation material surrounding the perimeter of each cell.

11. The sensor of claim 10, wherein the non-conductive insulation material comprises a dielectric material.

12. The sensor of claim 1, further comprising a plurality of guards, each guard comprising a central opening for placing a single excitation cell, the guard electrically isolated from the excitation cell and from other guards, and the guard made of a conductive material.

13. The sensor of claim 12, wherein the excitation cell and the guard are made of the same material.

14. The sensor of claim 12, wherein the excitation cell and the guard are driven by an excitation signal of the same frequency and phase.

15. The sensor of claim 1, wherein each of the first and second planar plates comprise a contacting surface covered with an insulation material intended for abutting contact with a biological object.

16. The sensor of claim 1, wherein the plurality of excitation cells are arranged in a linear array in the first planar plate, and the plurality of detector cells are arranged in a linear array in the second planar plate.

17. The sensor of claim 1, wherein the number of plurality of excitation cells is equal to the number of plurality of detector cells.

18. The sensor of claim 1, wherein activation of each paired excitation cell and detector cell occurs while all other paired excitation cells and detector cells are off .

19. The sensor of claim 1, wherein activation of a plurality of paired excitation cells and detector cells occurs at the same time.

20. The sensor of claim 1, wherein the spaced relation between the first and second planar plates is adjustable to adjust the chamber volume.

21. The sensor of claim 7, further comprising an image reconstruction processor in electrical communication with the data acquisition circuitry.

22. The sensor of claim 21, wherein the image reconstruction processor executes linear image reconstruction algorithms.

23. The sensor of claim 22, wherein the linear image reconstruction algorithm is linear back projection.

24. The sensor of any one of claims 1 to 23, wherein the electric field is a substantially linear electric field.

25. The sensor of claim 24, wherein deviation of the electric field from linearity is less than 20%.

26. The use of the sensor of any one of claims 1 to 25, for medical screening using capacitance data without image reconstruction.

27. The use of claim 26, wherein the medical screening uses capacitance data of a human female breast for detection of breast cancer.

28. The use of the sensor of any one of claims 1 to 25, for medical imaging.

29. The use of claim 28, wherein the medical imaging is imaging of a human female breast for detection of breast cancer.

30. The use of claim 28, wherein the medical imaging is conducted for the purpose of image guided needle biopsy of a human female breast to diagnose breast cancer.

31. The use of the sensor of any one of claims 1 to 25, for medical screening using phase angle calculation of impedance data without image reconstruction.

32. The use of claim 31, wherein the medical screening uses impedance data of a human female breast for detection of breast cancer.

33. The use of the sensor of any one of claims 1 to 25, for medical imaging using phase angle calculation of impedance data.

34. The use of claim 33, wherein the medical imaging is imaging of a human female breast for detection of breast cancer.

35. The use of claim 34, wherein the medical imaging is conducted for the purpose of image guided needle biopsy of a human female breast to diagnose breast cancer.

*

ABSTRACT OF THE DISCLOSURE

CXIX. Described herein is an electrical permittivity tomography sensor, comprising: a first planar plate comprising a plurality of excitation cells; a second planar plate comprising a plurality of detector cells**;** the first planar plate held in spaced parallel relation to the second planar plate and defining a chamber therebetween; the first and second planar plates arranged to align each excitation cell with a corresponding detector cell in a one-to-one paired relationship; and each paired excitation cell and detector cell configured for synchronized activation.

CXX.

Appendix 2: Ethics Approval

Sunnybrook
HEALTH SCIENCES CENTRE

440: Ultrasound and microbubble imaging and therapy in combination with chemotherapy and radiotherapy in mouse tumour models

Submitted by agiles on Tue, 2014-09-30 00:10

AUP Info

Protocol Status: Fully Approved
New Protocol Number: 14 - 440 (M-1)
Previous Protocol Number: 14-440
Expiry Date: Wed, 2015-10-14

Personnel

PI Surname: Czarnota
PI First Name: Gregory
PI Position: Clinician Scientist / Professor
PI Department: Radiation Oncology/ Physical Sciences
PI business phone:
PI mobile phone:
PI email:
Alternate Surname: Stanisz
Alternate First Name: Greg
Alternate Position: Scientist / Professor
Alternate phone:
Alternate email:
Delegate Name: Anoja Giles
Delegate Phone:
Delegate Email:
Research staff:

Name	Department	Position	Email	Training
Dr. Gregory Czarnota	Radiation Oncology/Physical science	Clinician/ Scientist		Yes
Dr. Azza Al Maharouki	Physical Sciences	Research Associate		Yes
Anoja Giles	Physical Sciences	Research Technician		Yes
Amr Hashim	Physical Sciences	Research Assistant		Yes
Golnaz Farhat	Med Biophysics	Grad Student		Yes
Zahra Jahed	Physical Sciences	Research Assistant		Yes
Christine Tarapacki	Physical Sciences	Research Assistant		Yes
Maurice Pasternak	Physical sciences	Grad Student		Yes
Lakshmanan Sannachi	Physical Sciences	Post Doc		Yes
CR Technician	CR	Technician		Yes
Aaron Cumal	Physical Sciences	Research Assistant		pending

CV

Name: Seyyed M. Hesabgar

Post-Secondary Education and Degrees:

PhD (Sep 2012-Oct 2016)
Department of Medical Biophysics, Schulich School of Medicine
Western University, London, Ontario

- Supervisor: Dr. A. Samani
- Research Project: Electrical impedance mammography (EIM) using low voltage and low frequency electric field
- Research Objective: Early detection of cancer tumors using EIM

Master of Science in Electrical Engineering (Sep 2007-Sep. 2009)
Western University, London, Ontario

- Supervisor: Dr. Hanif Ladak
- Research project: Modeling mechanical behavior of the tympanic membrane (ear drum) for designing high quality hearing aids and hearing prosthesis

Bachelor of Science in Electrical Engineering Electronics (Sep 2002-June 2006)
Shahid Beheshti University, Tehran, Iran

Related Work Experience:

Sensor Designer/Electronics Hardware Developer (Dec 2010 – Sep 2012)
LVD Electronics – Kitchener, Ontario

- Design, development and manufacturing of the ultrasound, optical, pressure and vibration sensors for mission critical applications

Teaching Assistantships:

Western University - London, Ontario (Jan 2014 - April 2016)

- Teaching tutorials, marking assignments, marking mid-term exams and helping students for the following course:
    - Fundamentals of Digital Imaging (MEDBIO 3503B)

Western University - London, Ontario (Sep 2007 – Sep 2009)

- Supervising and preparing experiments, marking assignments and helping students for the following course:
    - Introduction to Electrical Engineering (ECE 2238)

Research Assistantship:

Western University - London, Ontario (Sep 2012-Oct 2016)

- Electrical impedance modeling of biological tissue
- Finite-element based algorithms for measuring dielectric properties of biological tissues
- Design and implementation of the electrical impedance imaging sensors

Western University - London, Ontario (Sep 2007 – December 2010)

- Modeling and measuring the Young's modulus of the tympanic membrane using indentation technique and optimization algorithms.
- Improvement of an ultra-sensitive indentation machine with capability of measuring very small forces (as low as 0.01gr) and displacements as small as 0.5 micron.
- Modeling of the eardrum deformation using finite-element analysis and simulation of the indentation experiment.
- Using the information from indentation experiment and finite element simulation in an optimization algorithm in order to obtain the eardrum's Young's modulus

Conferences:

1. Sandeep Dhaliwal, Brian Rotenberg, Seyyed M. Hesabgar, Seyyed M. H. Haddad, Hanif Ladak, Abbas Samani, "Biomechanical properties of the oropharynx – contributing to a robust model of the upper airway in obstructive sleep apnea patients" CARS (Computer Assisted Radiology and Surgery) January 2015.

2. Seyyed Hesabgar, Abbas Samani; A Novel Technique for Measuring Electrical Permittivity of Biological Tissues at Low Frequencies; World Congress on Medical Physics and Biomedical Engineering, 2015, Toronto, Canada

3. Seyyed M. Hesabgar, Harry Marshall, Sumit K. Agrawal, Abbas Samani, Hanif M. Ladak , "Measuring the quasi-static Young's modulus of the eardrum using indentation technique", MEMRO (Middle-Ear Mechanics in Research and Otology), Stanford University, USA, June 24 - 28, 2009

Patent:

Seyyed Hesabgar, Ravi Menon, David Holdsworth, Abbas Samani; Hand-held portable low-cost medical scanner for breast cancer detection (US Provisional Patent W-15-036. Filed in August, 2015. Please see appendix 1 in pages 102-127)

Publications:

1. Seyed Reza Mousavi, Haisu Wang, Seyyed M. Hesabgar, Timothy Scholl, and Abbas Samani,

"Fast Shape-Similarity-Based Elastography Technique for Prostate Cancer Assessment; Medical Physics 09/2015; 42(9):5110-5119. DOI: 10.1118/1.4927572

2. Seyyed M. Hesabgar, Harry Marshall, Sumit K. Agrawal, Abbas Samani, Hanif M. Ladak "Measuring the quasi-static Young's modulus of the eardrum using an indentation technique" Submitted to hearing research society of America, published at Elsevier Hearing Journal Volume 263, Issues 1-2, May 2010, Pages 168-176)